INVESTIGATION ON THE MECHANISM OF WEAR OF SINGLE

CRYSTAL DIAMOND TOOL IN NANOMETRIC CUTTING OF IRON

USING MOLECULAR DYNAMICS (MD)AND THE DEVELOPMENT

OF GENERALIZED POTENTIAL ENERGY SURFACES (GPES)

BASED ON *AB INITIO* CALCULATIONS

By

RUTUPARNA NARULKAR

Bachelor of Engineering in Mechanical
Pt. Ravi Shankar University
Raipur,Chattisgarh, India
1999

Master of Science in Mechanical
Oklahoma State University
Stillwater, OK
2003

Submitted to the Faculty of the
Graduate College of
Oklahoma State University
in partial fulfillment of
the requirements for
the Degree of
DOCTOR OF PHILOSOPHY
December, 2009

INVESTIGATION ON THE MECHANISM OF WEAR OF SINGLE

CRYSTAL DIAMOND TOOL IN NANOMETRIC CUTTING OF IRON

USING MOLECULAR DYNAMICS (MD)AND THE DEVELOPMENT

OF GENERALIZED POTENTIAL ENERGY SURFACES (GPES)

BASED ON *AB INITIO* CALCULATIONS

Dissertation Approved:

Dr. R. Komanduri
_____
Dissertation advisor

Dr. L. M. Raff
_____

Dr. D. Lucca
_____

Dr. S. Bukkapatnam
_____

Dr. R. Delahouyssaye
_____

Dr. Gordon Emslie
_____
Dean of the Graduate College

ACKNOWLEDGMENTS

Completing this study would have been an impossible task had it not been for the un-ending guidance and support of my many teachers, family, and friends. Although the list of people I wish to express my deepest gratitude for far exceeds the scope of this page, I would like to thank the following persons for their dedication, support, and constant en-couragement.

First of all I would like to express my deepest gratitude to Dr. Ranga Komanduri, my advisor, who has been my supervisor since the beginning of my study. He provided me with countless helpful suggestions, exceptional advice, constant encouragement, and financial support during the course of this work. Working for Prof. Komanduri has always been a matter of *de rigueur*. His scientific insight has made him a reservoir of ideas and passions in engineering and science, which has immeasurably inspired and enriched my growth as a student, a researcher, and a scientist. I am indebted to him more than he knows.

I also wish to express my immense appreciation to Dr. Lionel Raff of the Department of Chemistry, Oklahoma State University, who made many valuable suggestions at all times. His ingenuity and resourcefulness in the field of science is phenomenol and have propelled and fostered my intellectual maturity that I will benefit from, for a long time to come. I wax eloquent about this person who has been responsible for so many years of my education and making me who I am today. He is extremely versatile and always ready to lend a helping hand when needed. There have been countless times when I have needed a strong foothold and he has been there to guide me and show me the way.

Special thanks are due to Dr. Satish Bukkapatnam, of Industrial Engineering and Man-

TABLE OF CONTENTS

LIST OF TABLES

LIST OF FIGURES

xvii

CHAPTER 1

INTRODUCTION

Machining is one of the most prevalent techniques for manufacturing parts. It involves the removal of material from the workpiece in the form of chips using a single-point or multiple-point tool. The cutting tool in machining is always harder than the workmaterial. Figure 1.1 is a schematic of the orthogonal machining operation. Machining involves extensive plastic deformation of the workmaterial ahead of the tool and between the tool and the sliding chip. When two surfaces are in sliding contact the result is a change in the surface characterstics of one or both of the surfaces. The loss of tool material is termed wear.
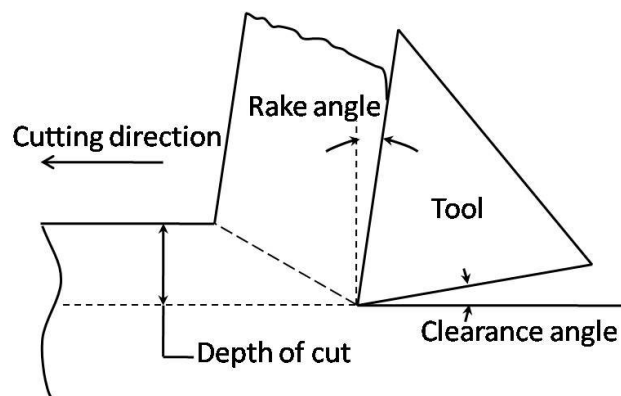
Figure 1.1: Orthogonal or 2D machining

During machining, high temperatures and mechanical and thermal stresses are generated on the tool. Also, newly generated machined surface is chemically very active (along

the chip-tool interface and clearance face/machined surface), and interacts extensively with the tool surface. Depending on the cutting conditions, tool-workpiece chemical reactivity along with previously mentioned conditions lead to the wear of the cutting tool. Wear of tool during machining is undesirable and should be minimized. In other words, a successful cutting tool material must resist these severe conditions and provide a reasonably long tool life. Diamond is one of such tool material, especially in the machining of ferrous materials and low carbon steels.

1.1   Diamond as a cutting tool material

Diamond, as a cutting tool material, is used extensively in ultraprecision machining and grinding on a wide range of workmaterials, including, semiconductors, soft metals, such as aluminum and copper and their alloys, and numerous polymers. The ubiquitous use of diamond is a result of its unique features, namely, highest hardness, its availability in single-crystal form (no grain boundaries), its ability to form an extremely sharp cutting edge, very high thermal conductivity, low friction, non-adhesion to most workmaterials, and high wear resistance [1].

Diamond has the highest hardness varying between 56-102 GPa depending on the crystallographic orientations [2]. This superior hardness is because each carbon atom is surrounded by four carbon atoms and is covalently bonded [3]. Its crystal structure is made up of two cubic face-centered lattices interpenetrating each other such that an atom in the lattice crystal is making a tetrahedral shape [4]. Both natural single crystal and synthetic polycrystalline forms are used as a cutting tool. It is possible to polish diamond tools to a surface finish (R_a) of $\sim$1 nm and a tip radius of about 10 nm [5]; this corresponds to an extremely sharp cutting edge which plays an important role in ultra-precision machining.

It is amazing but a fact that diamond, the hardest known material, is not suitable for machining pure iron or ferrous alloys, such as low carbon steels due to rapid tool wear.

2

Diamond tool wears out 10^4 times faster during machining mild steel than brass [6], where hardness of both workpieces are in the same range. This is because carbon has a strong affinity for iron to form iron carbide, especially at temperatures above and pressures below the diamond stable region [7–9]. Wear of the diamond tool can lead to surface damage and inaccuracy in precision machining. Due to demand for high accuracy in recent technological developments, it is of paramount importance to understand the mechanism behind the tool wear and take appropriate steps to minimize it.

1.2   Wear mechanism in diamond tool

Various factors involving thermal, chemical, mechanical are responsible for wear of the diamond tool. They can act simultaneously or alone to accelerate the wear depending on the ambient conditions. Wear of diamond also depends on various factors, such as structural anisotropy, imperfections, affinity for the metals being cut, temperature, and atmosphere.

Ikawa and Tanaka [10] proposed a mechanism of diamond tool wear involving initial phase transformation of diamond into graphite and subsequent diffusion of carbon into the iron workpiece. Komanduri and Shaw [8, 9] noted that diamond at room temperature is in a metastable state (sp^3 bonding) and will transform into graphite (sp^2 bonding) under appropriate conditions of pressure and temperature. An increase in temperature in cutting/grinding of ferrous materials without a concomitant increase in pressure (relative to diamond-graphite equilibrium) can promote graphitization [11]. This can be accelerated under the influence of properly directed shear stress [12]. The presence of a catalyst/solvent material, e.g. iron, that rapidly displaces graphite from the surface of diamond at high temperature can aid in this transformation [13].

It may be noted that iron is used as a catalyst/solvent in the synthesis of diamond under high pressure-high temperature conditions [14]. Therefore, it can play a similar role in reverse, namely, the transformation of diamond into graphite in the graphite stable region.

3

During machining, the freshly generated surface under the clearance face can further assist the graphitization process [15, 16]. All of the above mentioned conditions, namely, high temperatures, pressures below the diamond stable region, presence of hot iron, and newly generated machined nascent surface exist at the tool-chip and tool-workpiece interfaces.

The commonly accepted theory behind the mechanism of wear of diamond is graphitization. But there is no direct evidence provided by experimentalists or theorists so far. To comprehend the mechanism, one must understand the chemical and physical properties of iron and carbon (both diamond and graphite) and the nature of chemical interaction between them. The following sections (from Section 1.3 - 1.6) give an overview to the electronic states of carbon and iron, their polymorphism, and their affinity for each other.

1.3 Electronic states of carbon in diamond and graphite forms

Carbon has six electrons and at a ground state has $1s^2 2s^2 2p^2$ electronic configuration as shown Figure 1.2 (a), leaving two p-orbital vacant. But depending on the requirements, carbon can form up to four covalent bonds. This can result in the formation of various type of bonding. In the case of diamond, the electrons from $2s$ and $2p$ shells redistribute among themselves to form sp^3 hybrid orbitals [Figure 1.2 (b)]. A total of four hybridized orbitals are formed resulting in a tetrahedral structure. This results in some loss of energy but is compensated by strong covalent bond formation. In the case of graphite, the electrons from $2s$ and $2p$ shells redistribute among themselves to form sp^2 hybrid orbitals similar to diamond. But this time, only two of the three available p-orbitals are mixed with s-orbital [Figure 1.2 (c)]. Due to the electronic structure of carbon, it has this ability to form several types of bonding and thus make it very versatile in forming different structures, such as nanotubes, C_{60}, diamond, and graphite.
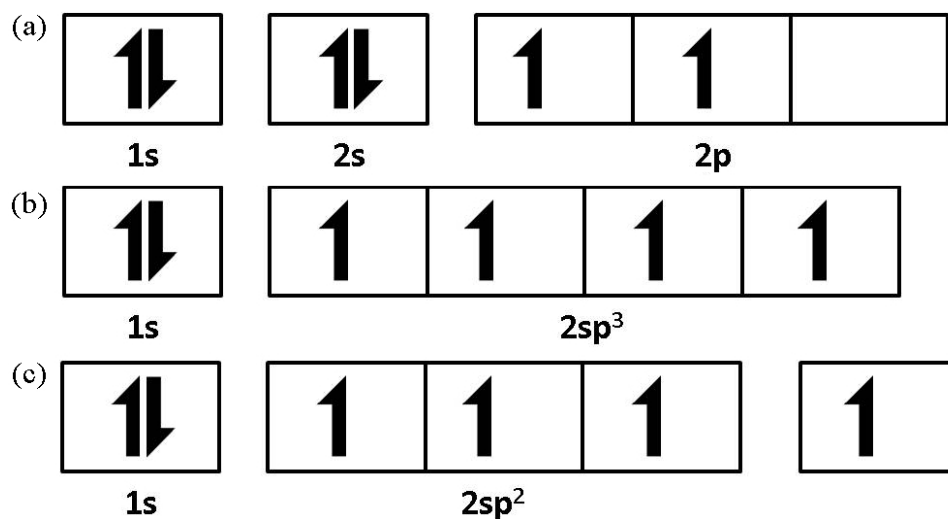
Figure 1.2: (a) Ground state of carbon, (b) sp^3 hybridized state of carbon, and (c) sp^2 hybridized state of carbon

Table 1.1: Properties of diamond and graphite

Properties	Diamond	Graphite
Bond length (Å)	1.545	1.421
Atomic density (nm^3)	176.3	113.9
Density (g/cm^3)	3.51	2.27
Youngs Modulus (GPa)	1140	11.8/5.2
Debye temperature (K)	1860	760
Melting point (K)	3800	4000
Thermal conductivity (W/m°C)	$2000-2500$	85
Electrical Resistivity ($\mu\Omega$-cm)	$\geq 10^{16}$	10^{-3}

1.4 Physical structures and properties of diamond and graphite

Due to the hybridization or nature of the bonding involved in diamond and graphite, the physical and chemical properties show a stark contrast. For example, diamond is the

hardest known material while graphite is one of the softest. While diamond is resistant to electric current, graphite is a good conductor of electricity. More details on physical and chemical properties are provided in Table 1.1.
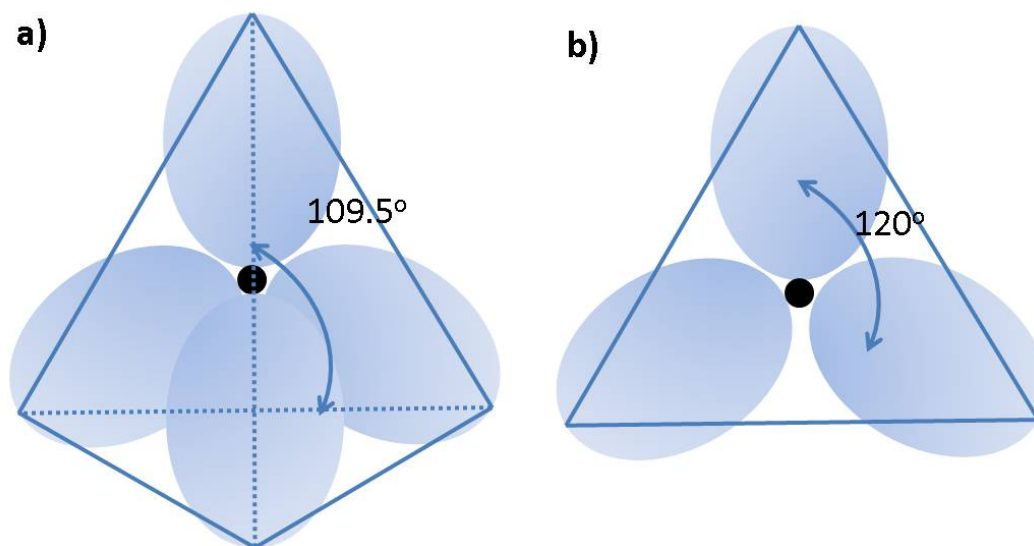
Figure 1.3: Carbon in a) tetraheral and b) planar structure

The physical structures of diamond and graphite are also very different. This is again attributed to the type of bonding involved. As mentioned earlier, in diamond, due to the sp^3 bonding, tetrahedral structure is formed [Figure 1.3 (a)], while in graphite, hexagonal structure is formed due to sp^2 bonding [Figure 1.3 (b)]. Due to this, carbon has an ability to form different crystal structures, such as tetrahedral, planar, and many more.

1.5 Structural transformation in carbon

Carbon exists in many allotropic forms. Some of the newly discovered forms are Bucky ball [17] and carbon nano tubes (CNTs) [18]. The main forms of carbon are cubic diamond and hexagonal graphite. Transformations among these forms occur under appropriate conditions of pressure and temperature (Figure 1.4). A brief introduction is given here. Only the transformation of diamond to graphite, which is the main focus of this study, is covered

in details in this section.
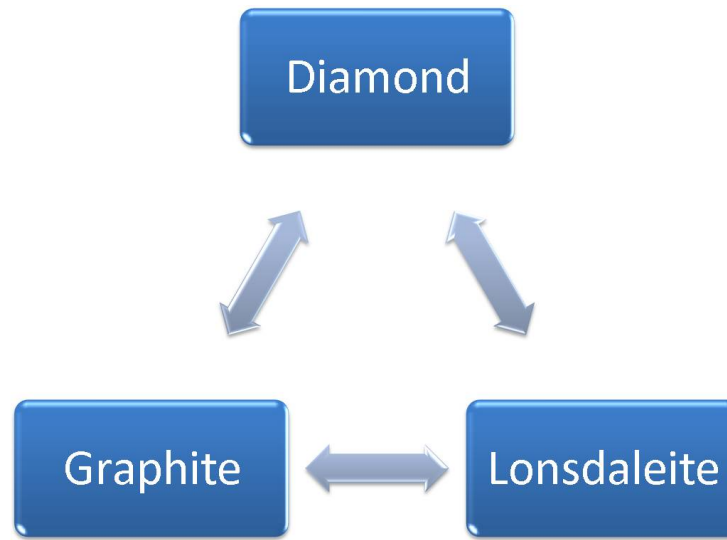
Figure 1.4: Transformation among various forms of carbon

1.5.1 Transformation of diamond to graphite
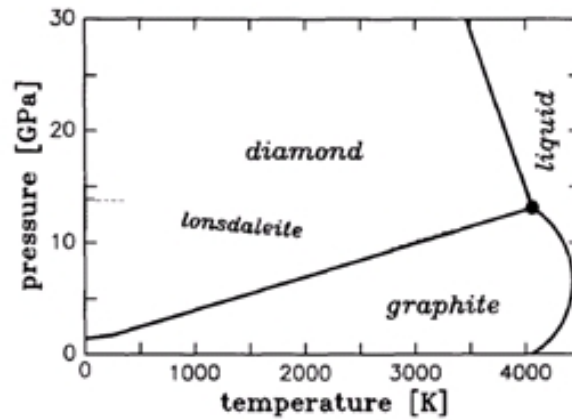
Figure 1.5: Carbon phase diagram [14]

Diamond is a metastable form of carbon at atmospheric conditions of temperature and pressure and under appropriate conditions, carbon atoms of diamond revert back to the stable graphite form. This observation was reported as early as 1847 [19]. The carbon phase

diagram (Figure 1.5) shows the appropriate conditions for diamond-graphite conversion or vice versa [14]. Recently, Wang *et al.* [20] have studied the carbon phase diagram from the *ab inito* molecular dynamics and found that diamond, graphite, and liquid phase coexist at a temperature of 4700 K and at a pressure of 12 GPa.

The conversion of diamond to graphite at NPT is extremely slow because of the presence of sp^3 bonding in diamond. The energy barriers required for graphitization are 730 kJ/mol (for dodecahedral face) and 1060 kJ/mol (for the octahedral face) [21]. Because of these high energy barriers required, graphitization of diamond is almost impossible under normal conditions. But in the presence of a metal catalyst, such as iron, these energy barriers are significantly lowered at elevated temperature as shown in Figure 1.6, and provide a faster rate for conversion from diamond to graphite. Chemical wear of diamond tool can proceed through catalytic mechanisms with or without the involvement of oxygen [22].
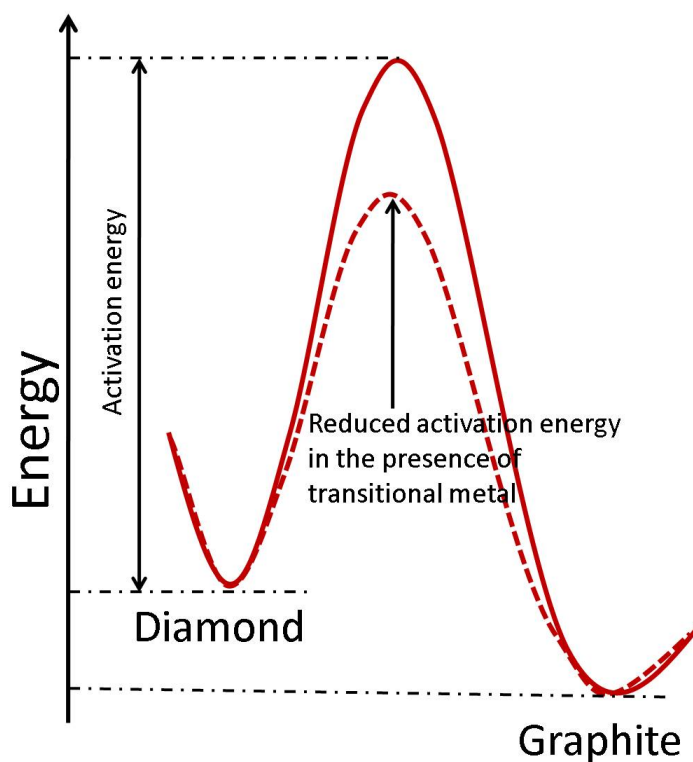
Figure 1.6: Reaction coordinate diagram [22]

8

1.6   Electronic structure of iron

Iron falls under Group VII of the Periodic Table. A single iron atom has 26 electrons and its basic electronic configuration is given as $1s^2 2s^2 2p^6 3s^2 3p^6 4s^2 3d^6$. As Fe atoms approach to form BCC iron, the electronic state is changed to $[Ar](3d_n)^{0.02} (3d_c)^{4.47} (3d_m)^{2.39}$ $(4s_c)^{0.60} (4s_f)^{0.52}$ [23]. Due to the available d shell, iron can have several oxidation levels to access. Commonly, it has divalent and trivalent ions and, hexavalent state is considered to be the highest. But recently, octahedral coordination complex of iron was reported [24].

1.6.1   Structural transformation in iron

Iron, similar to carbon, exhibits polymorphism under different conditions of pressure and temperature. Among metals, iron is the only metal that shows all the three crystal structures, namely, body-centered cubic (BCC), face-centered cubic (FCC), and hexagonal-closed pack (HCP). Figure 1.7 shows the pressure-temperature phase diagram for pure iron.
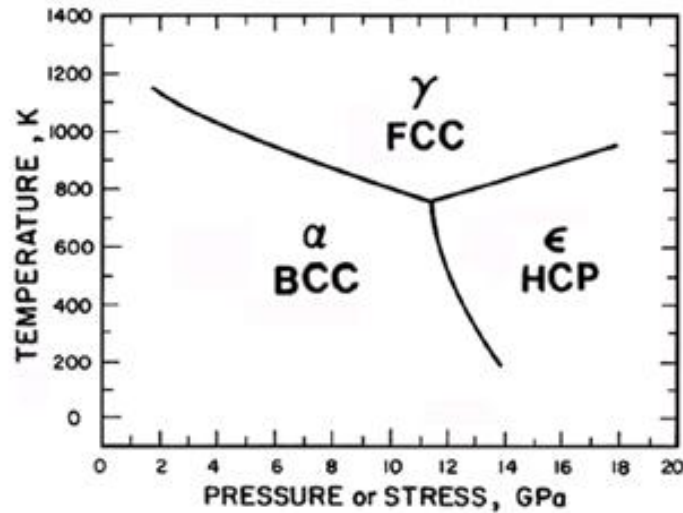
Figure 1.7: Temperature-pressure diagram of pure iron [25]

9

1.6.2 Affinity of iron for carbon

Iron and carbon together form different allotropic combinations with different crystallographic structures. Carbon also plays an important role as an alloying element with iron in forming various steels and cast irons. Fe_3C is a basic component of the carbon steels and white cast irons. This structure is metastable or unstable at ambient conditions [26]. It has an orthorhombic crystal structure (space group - Pnma). As shown in Figure 1.8, eight iron atoms are in "general" position, Fe(g), and four metal atoms, Fe(s) are in "special" positions with carbon atoms at the interstices [27]. Interestingly, this strong affinity of iron
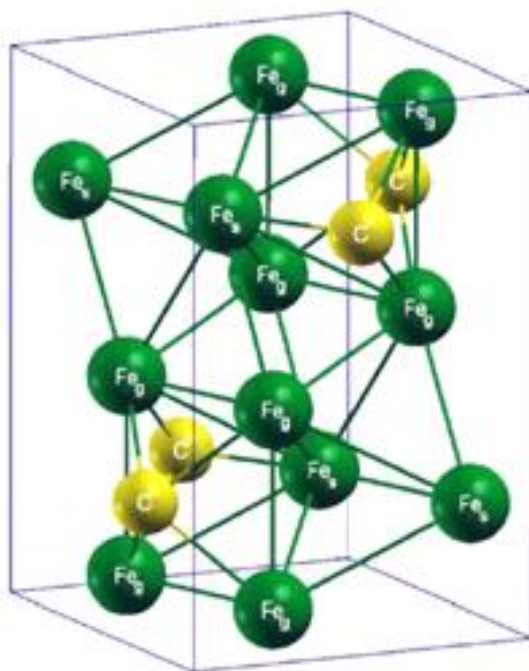
Figure 1.8: Crystal structure of a unit cell of cementite [26]

for carbon plays a vital role in the wear of diamond tool in the machining of iron and low carbon steels. One of the main focuses of this investigation is to study the role of iron in the wear of diamond using molecular dynamics (MD) simulations.

1.7 Simulation techniques

Different methods are available for simulating many physical or chemical processes at various times and length scales. Each method has its own advantages and disadvantages. Understanding the physics and chemistry behind the mechanisms involved, such as interaction between iron and carbon during nanometric machining, call for a fundamental approach. An ideal overture is to employ quantum calculations (*ab initio* molecular dynamics, AIMD), such as Born-Oppenheimer molecular dynamics (BOMD) directly to investigate the mechanism. We conducted *ab initio* molecular dynamics to estimate the time required
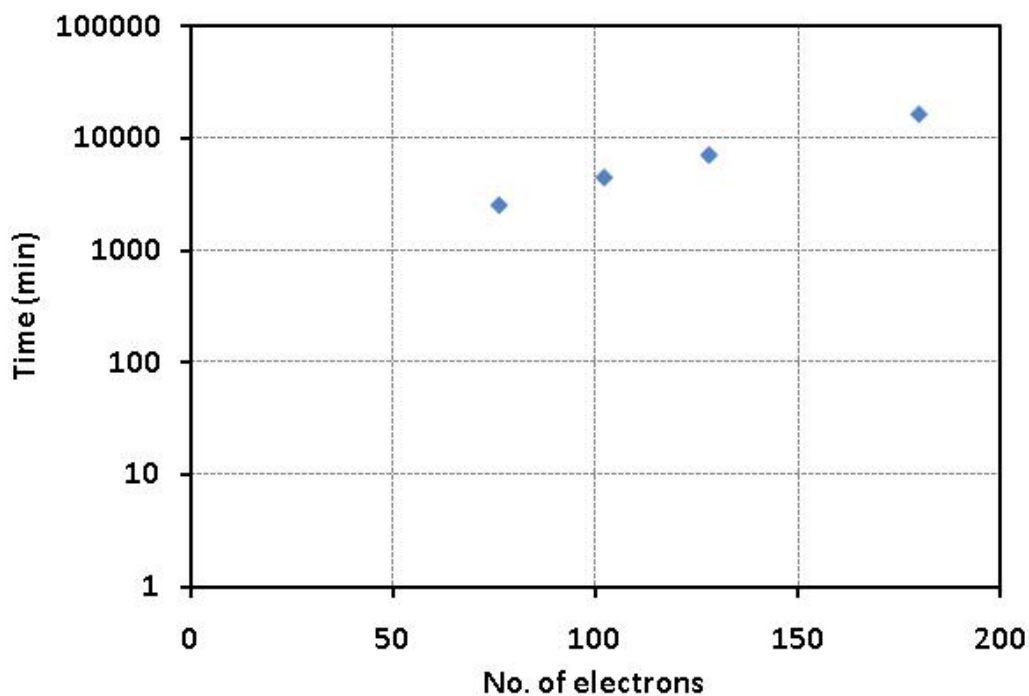
Figure 1.9: Time taken by ADMP with respect to the number of electrons for 1 ps

for the computation. Figure 1.9 shows the computation time required by Atom Centered Density Matrix Propagation (ADMP) molecular dynamics [28–30] model for a timescale of 1 ps wtih different number of electrons using Gaussian software [31]. It may be noted

that the Y-axis uses log time-scale. ADMP provides equivalent functionality to BOMD but at a reduced computational cost. But the time required to solve Schrödinger equations becomes intractable when the number of atoms/electrons increases to a nanometric scale.

Molecular dynamics (MD) and Monte Carlo (MC) simulations are the most powerful and robust existing methods for the investigation of the dynamical behavior of atomic and molecular motions of complex systems. With the advent of relatively inexpensive, powerful PCs, MD simulations have become a routine procedure in these investigations. Once the potential-energy hypersurface for the system has been obtained, the MD or MC computation is straightforward. In the majority of cases, the computational time required is on the order of hours to a few days (Figure 1.10).
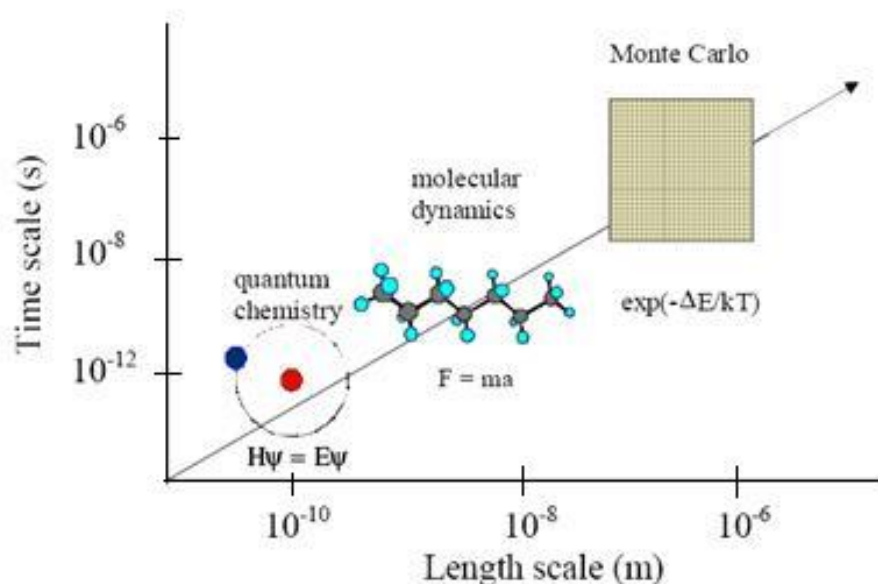
Figure 1.10: Comparison among the different simulation techniques [32]

Empirical potential surfaces are frequently employed to represent the interactions present in the system under investigation. In most cases, the functional forms present in these potentials are selected on the basis of chemical and physical intuitions. The parameters of the surface are adjusted to fit a set of experimental data that comprise bond energies, equilib-

12

rium bond distances and angles, fundamental vibrational frequencies, and measured barrier heights to reactions of interest.

The aim of this current work is to use MD simulations to investigate the mechanisms involved in the wear of diamond during the machining of iron and develop a generalized method that can be used to cultivate PES based on the *ab initio* calculations.

CHAPTER 2

REVIEW OF LITERATURE

Alder and Wainwright [33–35] initiated MD simulation studies at the Lawrence Radiation Laboratories (LRL) in the fields of equilibrium and non-equilibrium statistical mechanics in the early 1950's. They developed the calculations to perform MD which they employed to study the relaxation. They started with a 32-particle system in a FCC structure and extended to several hundreds of classical interacting particles. Since then, MD simulations have been applied to investigate a wide range of fields, such as chemical reactions, irradiation effects, tribology, indentation, and machining.

2.1 Interatomic potential

There are several types of potentials. Two body potentials are very simple and are an early form of the potentials developed. Morse [36] and Lennord-Jones [37] are examples of two-body potentials. The accuracy of a simulation depends on the potential used for the simulation. Therefore, it is very important to choose a potential that represents experimental results accurately. In the present study, various combinations of potentials were used depending on the requirements of the system to be analyzed. Potentials used in the present work are judiciously chosen, based upon their performance. Tersoff [38–40] and reactive empirical bond order (REBO) [41, 42] potentials were used to represent carbon and embedded atom method (EAM) [43, 44] and modified embedded atom method (MEAM) [45]

potentials for iron and iron-carbon interactions.

2.1.1 Tersoff potential

Tersoff potential [38–40] was developed to represent tetrahedral single component elements, such as diamond and silicon. It can also represent multi component systems, such as silicon carbide. The total potential energy E_i is represented by:

$$\sum_i E_i = \frac{1}{2} \sum_{i \neq j} V_{ij}$$

(2.1)

where, V_{ij} is the interaction between atom i and j which is given by:

$$V_{ij} = f_c(r_{ij}) \left[f_R(r_{ij}) + b_{ij} f_A(r_{ij}) \right]$$

(2.2)

f_c is the cutoff function, f_R and f_A are repulsive and attractive part of the potential, respectively, and are given by:

$$f_R(r_{ij}) = C_{ij} \exp(-\lambda_{ij} r_{ij})$$

(2.3)

$$f_A(r_{ij}) = -D_{ij} \exp(-\mu_{ij} r_{ij})$$

(2.4)

$$f_c(r_{ij}) = \begin{cases} 1, & r_{ij} < R_{ij} \\ \frac{1}{2} + \frac{1}{2} \cos\left[\pi \frac{(r_{ij} - R_{ij})}{(S_{ij} - R_{ij})} \right], & R_{ij} < r_{ij} < S_{ij} \\ 0, & rij > S_{ij} \end{cases}$$

(2.5)

b_{ij} is a three body interaction which is given by:

$$b_{ij} = \chi_{ij} (1 + \beta_i^{n_i} \xi_i^{n_i})^{-\frac{1}{2n_i}},$$

(2.6)

where,

$$\xi_i = \sum_{k \neq i,j} f_c(r_{ik}) \omega_{ik} g(\theta_{ijk}),$$

(2.7)

and

$$g(\theta_{ijk}) = 1 + \frac{c_i^2}{d_i^2} - \frac{c_i^2}{[d_i^2 + (h_i - \cos\theta_{ijk})^2]}$$

(2.8)

15

The Tersoff potential developed for carbon [39] produces an accurate description of the structural properties and energetics of carbon. It can also describe carbon-carbon single, double, and triple bond lengths and energies in hydrocarbons, as well as in solid graphite and diamond.

Table 2.1: Tersoff parameters for carbon and nitrogen

Parameter	Carbon [39]	Nitrogen [46]
C (eV)	1.3936×10^3	1.1000×10^4
D (eV)	3.476×10^2	2.1945×10^2
$\lambda(\text{Å}^{-1})$	3.4879	5.7708
$\mu(\text{Å}^{-1})$	2.2119	2.5115
β	1.5724×10^{-7}	1.0562×10^{-1}
n	7.2751×10^{-1}	1.24498×10^1
c	3.8049×10^4	7.9934×10^4
d	4.384×10^0	1.3432×10^2
h	-5.7058×10^{-1}	-9.973×10^{-1}
R (Å)	1.8	2.0
S (Å)	2.1	2.3
interactions	C-N	
χ_{ij}	0.9685	
ω_{ij}	0.6381	

2.1.2 Reactive empirical bond order (REBO) potential

Brenner [41, 42] developed an empirical many-body potential energy function that can represent intra molecular bonding in a variety of hydrocarbons as well as graphite and diamond. The potential is based on the Tersoff covalent bonding formalism. REBO potential addresses the issue of over-binding of radicals in the Tersoff potential, like in intermediate bonding situations, the assumption of near-neighbor interactions when combined with the sum over atomic sites results in aphysical behavior. For example, if a carbon atom with three nearest neighbors is bonded to a carbon atom with four neighbors [42]. The Tersoff formalism interpolates the bonds so that it is between a single and a double bond. Brenner corrected the shortcomings of Tersoff potential by rewriting the Tersoff equation along with adding corrections. The total energy is represented as follows:

$$E_b = \sum_i \sum_{j(>i)} \left[V_R(r_{ij}) - \bar{B}_{ij} V_A(r_{ij}) \right], \tag{2.9}$$

where, $V_R(r_{ij})$ and $V_A(r_{ij})$ are the attractive and repulsive components of the potential and are represented as follows:

$$V_R(r_{ij}) = f_{ij}(r_{ij}) D^e_{ij} / (S_{ij} - 1) e^{\sqrt{2S_{ij}} \beta_{ij}(r_{ij} - R^e_{ij})} \tag{2.10}$$

$$V_A(r_{ij}) = f_{ij}(r_{ij}) D^e_{ij} S_{ij} / (S_{ij} - 1) e^{\sqrt{2S_{ij}} \beta_{ij}(r_{ij} - R^e_{ij})} \tag{2.11}$$

$f_{ij}(r_{ij})$ is a cutoff function which restricts the pair potential only to the nearest neighbors and is given by:

$$f_{ij}(r_{ij}) = \begin{cases} 1, & r_{ij} < R^1_{ij} \\ \dfrac{1}{2} + \dfrac{1}{2} \cos\left[\pi \dfrac{(r_{ij} - R^1_{ij})}{(R^2_{ij} - R^1_{ij})} \right], & R^1_{ij} < r_{ij} < R^2_{ij} \\ 0, & r_{ij} > R^2_{ij} \end{cases} \tag{2.12}$$

17

The empirical bond-order function, $\bar{B}_{ij}$ is given by the average of terms associated with each atom in a bond plus a correction and is given by,

$$\bar{B}_{ij} = (B_{ij} + B_{ji})/2 + F_{ij}(N_i^{(t)} + N_j^{(t)} + N_{ij}^{conj}), \tag{2.13}$$

$$B_{ij} = \left[1 + \sum_{k(\neq i,j)} G_i(\theta_{ijk}) f_{ik}(r_{ik}) exp\left(\alpha_{ijk}[(r_{ij} - R_{ij}^e) - (r_{ik} - R_{ik}^e)]\right)\right]^{-\delta_i}, \tag{2.14}$$

The quantities N_{ij}^H and N_{ij}^C are the number of hydrogen and carbon atoms, respectively, bonded to atom i equations (2.15) and (2.15), respectively,

$$N_{ij}^H = \sum_{j(\neq hydrogen)} f_{ij}(r_{ij}), \tag{2.15}$$

$$N_{ij}^C = \sum_{j(\neq carbon)} f_{ij}(r_{ij}), \tag{2.16}$$

N_{ij}^{conj} depends on whether a bond between atoms i and j is a part of a conjugated system and is represented by,

$$N_{ij}^{conj} = 1 + \sum_{carbons\ k(\neq i,j)} f_{ik}(r_{ik}) F_{ik}(x_{ik}) + \sum_{carbons\ l(\neq i,j)} f_{jl}(r_{jl}) F_{jl}(x_{jl}) \tag{2.17}$$

where,

$$F(x_{ij}) = \begin{cases} 1, & x_{ij} \leq 2 \\ \frac{1}{2} + \frac{1}{2}\cos\left[\pi(x_{ik} - 2)\right], & 2 < x_{ij} < 3 \\ 0, & x_{ij} \geq 3 \end{cases} \tag{2.18}$$

$$x_{ik} = N_k^{tot} - f_{ik}(r_{ik}) \tag{2.19}$$

$G(\theta_{ijk})$ is a function of the angle between i-j and i-k bonds and is given by,

$$G(\theta_{ijk}) = a_0 \left(1 + c_0^2/d_0^2 - c_0^2/[d_0^2 + (1 + cos\theta_{ijk})^2] \right) \qquad (2.20)$$

2.1.3 Embedded-atom Method (EAM) Potential

Daw and Baskes [43, 44] conceptualized Embedded-atom Method (EAM) potential based on density functional theory (DFT) calculations to represent metallic systems. The potential was also applied to impurities, surfaces, and other defects in metals. It is based on the concept that energy is a function of electron density as well. The potential may be represented by:

$$E_{tot} = \frac{1}{2}\sum_{ij}V(r_{ij}) + \sum_{i}F(\rho_i), \qquad (2.21)$$

$$\rho_i = \sum_{i\neq j}\varphi(r_{ij}), \qquad (2.22)$$

where, F is the embedding energy and ρ_i is the electron density.

Base on this method, Simonelli *et al.* [47] developed EAM potential for BCC iron. Ruda *et al.* [48] presented empirical interatomic potential for the description of C interstitial impurities in metals and intermetallic alloys for C-M systems (M= Al, Ti, Ni, Fe, and Nb). They have used this potential and calculated the heat of solution of carbon in these metals. Furthermore, the potential also predicts lattice parameters of ternary perovskite carbides that agree with experimental data. Based on potential developed by Simonelli, they obtained C-Fe interaction by empirically adjusting the experimental and *ab initio* data [49] calculated for B_1 structures to a modified linear combination of the effective-pair interaction between C-C and Fe-Fe. The general form for the combination is given by:

$$V_{C-M}^{eff}(a+bx) = A\left[V_{C-C}^{eff}(c+dx) + V_{M-M}^{eff}(e+fx)\right] \qquad (2.23)$$

where, A = 1.25, a = 0.20, b = 4.0, c = 1.0557, d = 4.2253, e = 0.99294, and f = 3.10336. In order to achieve complete interaction, the value of x is varied from zero to unity and the

results are plotted in Figure 2.1.
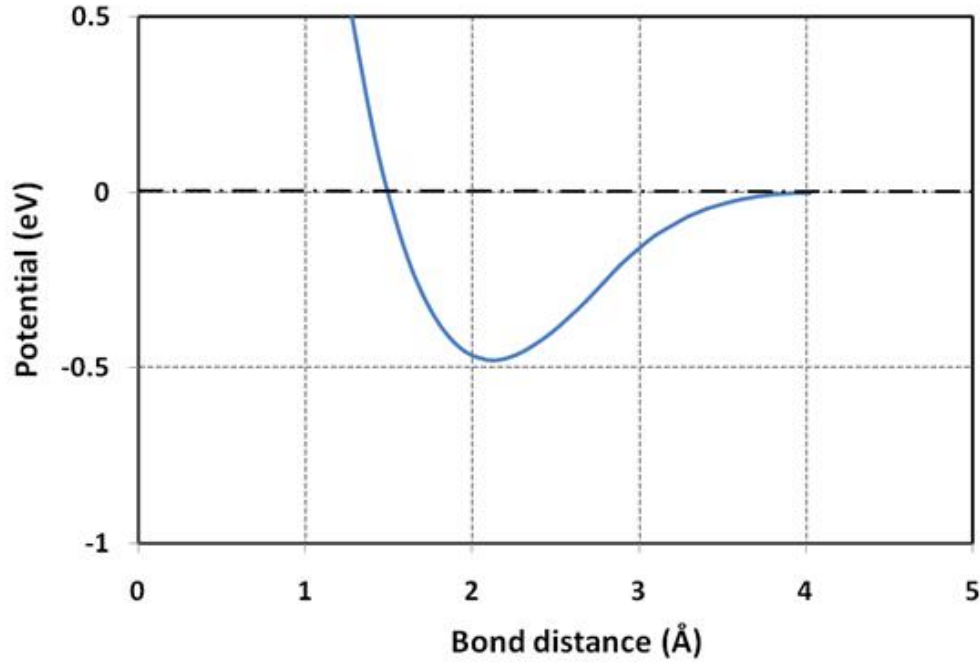
Figure 2.1: EAM potential for the Fe-C system

They obtained the effective C-C potential from the Tersoff potential [38] without any angular dependency and is given by:

$$V_{C-C}^{eff} = 709.1e^{-3.161r_{ij}} - 191.6e^{-2.305r_{ij}} \tag{2.24}$$

2.1.4 Modified Embedded-atom Method (MEAM) Potential

Baskes [45] modified EAM potential by incorporating angular terms to get Modified Embedded-atom Method (MEAM). The potential can represent physical properties of metals, for various crystal structures, such as FCC, BCC, HCP; and diamond cubic; semi-conductors, such as silicon; and diatomic gases, such as hydrogen. The MEAM potential is unique in the sense that with a single formalism it can represent properties of metals,

semiconductors as well as diatomic gas. In MEAM, the total energy is represented by:

$$E = \sum_i \left[\frac{1}{2} \sum_{j(\neq i)} \Phi(R_{ij}) + \sum_i F(\rho_i) \right], \tag{2.25}$$

where, F is the embedding function, ρ_i is the background electron density at the site i, and $\Phi(R_{ij})$ is the pair potential interaction between i and j separated by distance R_{ij}. The embedding function has the following form:

$$F(\bar{\rho}) = AE_c(\bar{\rho}/\bar{\rho}^\circ)ln(\bar{\rho}/\bar{\rho}^\circ), \tag{2.26}$$

where, A is an adjustable parameter, E_c is the sublimation energy, and $\bar{\rho}^\circ$ is the is the background electron density for a reference structure. Typically, the equilibrium structure is taken as a reference structure. The background density $\bar{\rho}^\circ$ is composed of a spherically symmetric partial electron density $\rho_i^{(0)}$ and the angular distributions $\rho_i^{(1)}$, $\rho_i^{(2)}$, and $\rho_i^{(3)}$. Each partial electron density can be represented by the following forms:

$$\left(\rho_i^{(0)} \right)^2 = \left[\sum_{j \neq i} \rho_j^{a(0)}(R_{ij}) \right]^2 \tag{2.27}$$

$$\left(\rho_i^{(1)} \right)^2 = \sum_\alpha \left[\sum_{j \neq i} \frac{R_{ij}^\alpha}{R_{ij}} \rho_j^{a(1)}(R_{ij}) \right]^2 \tag{2.28}$$

$$\left(\rho_i^{(2)} \right)^2 = \sum_{\alpha,\beta} \left[\sum_{j \neq i} \frac{R_{ij}^\alpha R_{ij}^\beta}{R_{ij}^2} \rho_j^{a(2)}(R_{ij}) \right]^2 - \frac{1}{3} \left[\sum_{j \neq i} \rho_j^{a(2)}(R_{ij}) \right]^2 \tag{2.29}$$

$$\left(\rho_i^{(3)} \right)^2 = \sum_{\alpha,\beta,\gamma} \left[\sum_{j \neq i} \frac{R_{ij}^\alpha R_{ij}^\beta R_{ij}^\gamma}{R_{ij}^3} \rho_j^{a(3)}(R_{ij}) \right]^2 - \frac{3}{5} \sum_\alpha \left[\sum_{j \neq i} \frac{R_{ij}^\alpha}{R_{ij}} \rho_j^{a(2)}(R_{ij}) \right]^2 \tag{2.30}$$

where, $\rho_i^{(h)}$ represents atomic electron densities from j atom at a distance R_{ij} from site i. R_{ij}^α is the α component of the distance vector between atoms j and i. The expression for $\rho_i^{(3)}$ was incorporated to make partial electron densities orthogonal [50]. The atomic electron density is given as:

$$\bar{\rho}_i = \rho_i^{(0)} G(\Gamma_i) \tag{2.31}$$

where,

$$G(\Gamma) = 2/(1 + e^{-\Gamma})$$ (2.32)

$$\Gamma_i = \sum_{h=1}^{3} [\rho_i^{(h)}/\rho_i^{(0)}]^2$$ (2.33)

where, $t^{(h)}$ are adjustable parameters. The atomic density is given as:

$$\rho^{a(h)}(R) = exp[-\beta^{(h)}(R/r_e - 1)]$$ (2.34)

Here, $\beta^{(h)}$ are adjustable parameters and r_e is the nearest neighbor distance in the equilibrium reference structure. In MEAM, the energy per atom for the reference structure is obtained from the universal equation of state developed by Rose *et al.* [51] as a function of neighboring distance R:

$$E^u(R) = -E_c(1 + a + da^{*3})e^{-a^*}$$ (2.35)

where, d is an adjustable parameter, and

$$a^* = \alpha(R/r_e - 1)$$ (2.36)

$$\alpha = \left(\frac{9B\Omega}{E_c}\right)^{1/2}$$ (2.37)

Here, $E^u(R)$ is the universal function for a uniform expansion or contraction in the reference structure, B is the bulk modulus, and Ω is the equilibrium atomic volume. The expression for the pair interaction between two atoms separated by a distance R is given by,

$$\Phi(R) = (2/Z_1)[E^u(R) - F(\bar{\rho}^\circ(R))]$$ (2.38)

where, Z_1 is the number of the nearest-neighbor atoms. Initially in the MEAM potential, only the first neighbor interactions were considered. This caused some critical problems in

the potential. First, for many BCC metals, the surface energy of (111) surface is computed to be smaller than that of the (100) surface. Also, it generated a structure more stable than BCC for some BCC metals. In order to overcome these problems, Lee and Baskes [52, 53] extended the formalism to the second nearest neighbor interactions given by:

$$\Phi(R) = \psi(R) + \sum_{n=1} (-1)^n (Z_2 S/Z_1)^n \psi(a^n R) \qquad (2.39)$$

The summation is performed until the correct value of energy is obtained for the reference structure, where, Z_2 is the number of second nearest-neighbor atoms, a is the ratio between the second and the first nearest-neighbor distances, S is the screen function on the second nearest-neighbor interaction, which is a constant for a given reference structure.

$$\psi(R) = \phi(R) + (Z_2 S/Z_1)^n \psi(a^n R) \qquad (2.40)$$

Lee and Lee [54] developed a semi-empirical potential for carbon. They reported that the potential describes various stryctural properties of diamond satisfactorily. But it cannot represent graphit unless it is combined with the Lennard-Jones potential. Though, this potential was never used to represent diamond-graphite transformation.

Lee [55] applied the potential to Fe-C system which reproduces various physical properties of iron carbide. These properties include dilute heat of solution of carbon, the vacancy-carbon binding energy, the location of interstitial carbon atoms, and the migration energy of carbon atoms in BCC and FCC iron. The iron-carbon interaction is given by:

$$\phi_{FeC}(R) = \frac{1}{3} E^u_{Fe_3 C}(R) - \frac{1}{4} F_{Fe}(\bar{\rho}_{Fe}) - \frac{1}{12} F_C(\bar{\rho}_C) - \phi_{FeFe}(R)$$
$$- \frac{3}{4} S_{Fe} \phi_{FeFe}(aR) - \frac{3}{4} S_C \phi_{CC}(aR) \qquad (2.41)$$

Lee [56] also developed a potential for Fe-N system which can reproduce physical properties, such as the dilute heat of solution of nitrogen, the location of interstitial nitrogen atoms, the migration energy of nitrogen atoms, the vacancy-carbon binding energy and its

configuration in BCC and FCC iron, and the enthalpy of formation and lattice parameters of nitride phases. The iron-nitrogen interaction is given by:

$$\phi_{FeN}(R) = \frac{1}{3}E^u_{FeN}(R) - \frac{1}{6}F_{Fe}(\bar{\rho}_{Fe}) - \frac{1}{6}F_N(\bar{\rho}_N) - \phi_{FeFe}(R)$$
$$- S_{Fe}\phi_{FeFe}(aR) - S_N\phi_{NN}(aR)$$

(2.42)

Table 2.2: MEAM potential parameters for pure iron, carbon, and nitrogen [55, 56]

Parameter	Fe	C	N
E_c	4.29	7.37	4.88
r_e	2.48	1.54	1.10
B	1.73	4.45	5.96
A	0.56	1.18	1.80
$\beta^{(0)}$	4.15	4.25	2.75
$\beta^{(1)}$	1.0	2.8	4.0
$\beta^{(2)}$	1.0	2.0	4.0
$\beta^{(3)}$	1.0	5.0	4.0
$t^{(1)}$	2.6	3.2	0.05
$t^{(2)}$	1.8	1.44	1.00
$t^{(3)}$	-7.2	-4.5	0.00
C_{max}	2.8	2.8	2.8
C_{min}	0.36	1.41	2.00
d	0.05	0.00	0.00

In MEAM, the pair potential is computed from the reference structure. The energy of the reference structure for a range of values of R_{ij} is computed, assuming isotropic expansion or compression, and obtaining the pair potential from that by assuming the

Table 2.3: MEAM potential parameters for Fe-C and Fe-N alloys [55, 56]

Parameter	Fe-C	F-N
E_c	$0.75E_cFe + 0.25E_c^C + 0.95$	$0.5E_cFe + 0.5E_c^C + 0.7$
r_e	2.364	2.09
B	2.644	2.195
d	$0.75d_c^{Fe} + 0.25d_c^C$	$0.75d_c^{Fe} + 0.25d_c^N$
C_{min}	0.36 (Fe-C-Fe)	0.16 (Fe-N-Fe)
C_{min}	0.16 (C-Fe-C)	0.16 (N-Fe-N)
C_{min}	0.16 (Fe-Fe-C)	0.16 (Fe-Fe-N)
C_{min}	0.16 (Fe-C-C)	$\left[0.5(C_{min}^{Fe})^{1/2} + 0.5(C_{min}^{N})^{1/2}\right]^{1/2}$
C_{max}	2.80 (Fe-C-Fe)	1.44 (Fe-N-Fe)
C_{max}	1.44 (C-Fe-C)	2.80 (N-Fe-N)
C_{max}	2.80 (Fe-Fe-C)	2.80 (Fe-Fe-N)
C_{max}	2.80 (Fe-C-C)	2.80 (Fe-N-N)
ρ_0	$\rho_0^C/\rho_0^{Fe} = 6$	$\rho_0^N/\rho_0^{Fe} = 18$
Ref. structure	L_{12}	B_1

material obeys the Rose energy function. In the LAMMPS code [57] subroutine compute_pair_meam (), phi_meam () is called to compute the pair potential at a list of values in r (the array "phir"), and then call interpolate_meam() to create the arrays phirar1, phirar2, etc. These are coefficients that later are used to interpolate $\phi(R)$ and its derivative (search for "phirar" in meam_force.F to see where it occurs).

In the case of alloys, meam_force.F, computing derivatives of the total density doesn't have anything to do with the the pair interaction - it is related to the density part of the potential and the forces are calculated numerically (no 'if' conditions are present to identify

the lattice structure). Note that the way the density is computed does not depend on the reference structure of alloys; only the pair potential does.

2.2 Molecular Dynamics (MD) simulation of nanometric machining

Belak *et al.* [58, 59] conducted md simulation of orthogonal or 2D cutting of copper using the embedded-atom method (EAM) potential. Calculations at a cutting speed of 100 m s^{-1} with different edge radii tools and different cut depths were reported. An infinitely hard tool was considered in all the cases. While this may appear reasonable as the hardness of copper is only a small fraction of the hardness of the diamond tool, by making it infinitely rigid, the diamond potential is actually not considered.

The investigations of Ikawa *et al.* [60], Shimada *et al.* [61, 62], and Shimada [63] of Japan were mainly on MD simulations of nanometric cutting of copper using a diamond tool. The workpiece was also 2-D in their cases. Investigations were made to study the effect of edge radius and depth of cut on the chip formation process, subsurface deformation, and specific cutting energy. Most of the tests were simulated at 200 m s^{-1}, though a few were simulated at 5 m s^{-1}.

Ikawa *et al.* [60] investigated the minimum chip thickness that can be removed from the workpiece using both experiments and simulations without compromising on the surface finish. For simulations, they used different Morse potential parameters between aluminum workpiece and infinite hard diamond tool. They concluded that the cutting mechanism differs by using different potentials. They reported that although there was no remarkable difference in the chip formation, there was a significant effect on the machined surface.

Inamura *et al.* [64–67] reported MD simulation under quasi-static conditions where only the changes in the minimum-energy positions (which are the mean positions of the vibrating atoms) were followed. They intoduced a method by which energy dissipation is

26

incoroporated in the atomic-scale model to simulate cutting tests. They reported that the distribution of stress and strain in nanoscale cutting is similar to that of microscale cutting except they did not report any concentrated shear plane in the primary shear zone.

Maekawa and Itoh [68] developed the concept of area restricted molecular dynamics (ARMD). In this method, instead of running simulation for the entire workpiece, simulations were carried out in a region near the tool nose with a radius of 7.3 nm. This restricted region moves along with the tool as the simulation proceeds. This process reduces the overall computational time but makes the process dependent on the cutting geometry and tool geometry.

Komanduri, Chandrasekaran, and Raff have done significant work in the field of MD simulations of nanometric machining, material properties, and tribology which are described in details as follows. Chandrasekaran *et al.* [69] introduced the length restricted molecular dynamics (LRMD). In this, the length of the workpiece is kept constant throughout the experiment but its position is shifted along the direction of the cut. In other words, the atoms from the machined part of the workmaterial that are not going to affect the simulation results significantly are discarded, but their memory positions are retained. These memory positions are used to add new atoms to the work material. With this method, a small workpiece can be used to simulate cutting to any distance.

Komanduri, Chandrasekaran, and Raff [70] investigated the effect of tool geometry in nanometric cutting using MD simulations with different edge radii relative to depth of cut. They conducted simulations by varying the tool edge radius, r (3.62 to 21.72 nm) and depths of cut, d (0.362 to 2.172 nm) by maintaining the d/r ratio constant (0.1, 0.2, and 0.3). They investigated the variation of the cutting and thrust forces, the force ratio, the specific energy, and the sub-surface deformation with the tool geometry and depth of cut and concluded that they have significant influence on them which is in agreement with the experimental observations.

Komanduri, Chandrasekaran, and Raff [71, 72] simulated grinding by conducting MD simulations with negative rake tools. They compared the variations in the cutting forces, specific energy (energy required for removal of unit volume of work material), nature of subsurface deformation, and the size effect with rake angle with the published experimental results. They observed that specific energy in nanometric cutting was nearly an order of magnitude larger than in conventional cutting. They attributed that to the size effect that is commonly reported when the specimen size under consideration has submicrometer to nanometer dimensions.

Komanduri, Chandrasekaran, and Raff [73] also conducted MD simulations of nanometric cutting on single crystal aluminum in specific combinations of crystal orientation (111), (110), and (001) and cutting directions [$\bar{1}$10], [$\bar{2}$11], and [100] and with tools of different rake angles (10°, 30°, and 45°) to investigate the nature of deformation and the extent of anisotropy of aluminum. They found that when the aluminum crystal was oriented in plane (111) and cut in the <$\bar{1}$10> direction, plastic deformation ahead of the tool was accomplished predominantly by compression along with shear in the cutting direction. Also, the deformation in the work material, underneath the depth of cut region, was found to be along the cutting direction. In (001)[$\bar{1}$10] combination, the dislocations were found to be generated parallel to the cutting direction. In contrast, in (110)[001] combination, the dislocations were generated normal to the cutting direction. In the case of (110) orientation and [$\bar{1}$10] cutting direction, the dislocations were found to be parallel as well as perpendicular to the cutting direction. In contrast, for (001)[100] combination, extensive dislocations motion at $\sim 45°$ to the cutting direction was seen. Similarly, for (111)[$\bar{2}$11] combination, the dislocation motion was observed to be at $\sim 60°$ to the cutting direction.

Molecular dynamics (MD) simulations of nanometric cutting were conducted under different cutting conditions to investigate burr formation and exit failure in metals [74]. They investigated the effect of relative ductility of the workmaterial (e.g. soft versus hard),

tool rake angle (–30° to +60°), depth of cut (1.45 to 3.62 nm), and external constraint at workmaterial exit on the exit failure and burr formation.

Komanduri, Chandrasekaran, and Raff [75] investigated the effect of rake angles (from -60° to +60°), widths of cut (1.1 to 4.34 nm), depths of cut (0.01 to 2.72 nm), and clearance angles (10° to 30°) on the nature of material removal and surface generation process in ultraprecision machining and grinding of pure, defect-free silicon. They observed pressure-induced phase transition from a diamond cubic (or α-silicon) to a bct (or β-tin structure) in the case of machining silicon. They also concluded that an alternate final polishing process, such as chemomechanical polishing, is required to produce defect free surface at an atomic scale because of the subsurface or near-surface deformation was observed in all the cases of rake angle. They divided material removal mechanisms into four components: (i) compression of the work material ahead of the tool; (ii) chip formation akin to an extrusion-like process; (iii) side flow; and (iv) subsurface deformation in the machined surface.

2.3 Monte Carlo (MC) simulation of nanometric machining

Due to very high cutting speeds required for MD simulation of nanometric cutting, Komanduri, Narulkar, and Raff [76] have worked on simulating nanometric machining at conventional cutting speeds (5 m s^{-1}). They accomplished this by defining a local temperature in the cutting zone generated by shear plane heat source and tool-chip frictional heat source. Extension of this method to the nanometric regime permits an accurate estimate of the local temperature in cutting. This temperature was then employed in the Boltzmann probability distribution function that was used to determine the acceptancerejection of Monte Carlo moves in the simulation, given by Eq. (2.43).

$$exp\left(-\frac{V(q_0)}{KT}\right) \geq \xi_i \tag{2.43}$$

where, ξ_i is the random number generated between 0 and 1 in the ith Markov move and $V = V_{new} - V_{old}$.

The total rise at any point in the workpiece is given by:

$$\theta_M = \frac{q_{pl}}{\pi\lambda}\left\{(B_{chip} - \delta B)\int_{l_i=0}^{L} exp\left(\frac{-(X-l_i)v}{2a}\right)\left[K_0(\frac{R_i v}{2a}) + K_0(\frac{R_i^{'v}}{2a})\right]dl_i\right.$$
$$+ 2B\int_{l_i=0}^{L}\left(\frac{l_i}{L}\right)^m exp\left(\frac{-(X-l_i)v}{2a}\right)dl_i$$
$$\left. + C\delta B\int_{l_i=0}^{L}\left(\frac{l_i}{L}\right)^k exp\left(\frac{-(X-l_i)v}{2a}\right)dl_i\right\}$$
$$+ \frac{q_{pls}}{\lambda}\int_{w_i=0}^{t_{ch}/cos(\phi-\alpha)} exp\left(\frac{-(X-l_i)v}{2a}\right)\left[K_0\left(\frac{v}{2a}\left[(X-X_i)^2 + (z-z_i)^2\right]^{1/2}\right)\right.$$
$$\left. + K_0\left(\frac{v}{2a}\left[(X-X_i)^2 + (2t-z-z_i)^2\right]^{1/2}\right)\right]dw_i$$

$$(2.44)$$

This method for the thermal analysis is developed by Komanduri and Hou [77] for conventional machining as shown in Figure 2.2.

Since cutting speed was closely related to cutting temperature, the cutting speed enters the calculation via the thermal analysis equations. This method is computationaly efficient and saves 1000 hrs of the time over MD at low cutting speeds (Figure 2.3).

The method was applied to nanometric cutting of single-crystal aluminum with the crystal oriented in the (001) plane and cut in the <100> direction. Three positive rake cutting tools, namely 10°, 30°, and 45° were employed to investigate the effect of the rake angle on the forces, the specific energy, and the nature of the chip formation. The method was evaluated by direct comparison with corresponding molecular dynamics simulations conducted under the same conditions (Figure 2.4).

This work was further extended and optimized by Narulkar, Raff, and Komanduri [78] by incorporating steepest descent (SD) along with MC to improve on computational time and memory space. They observed that this MCSD combination is found to reduce the required computational times by factors of at least two to three over those achieved using
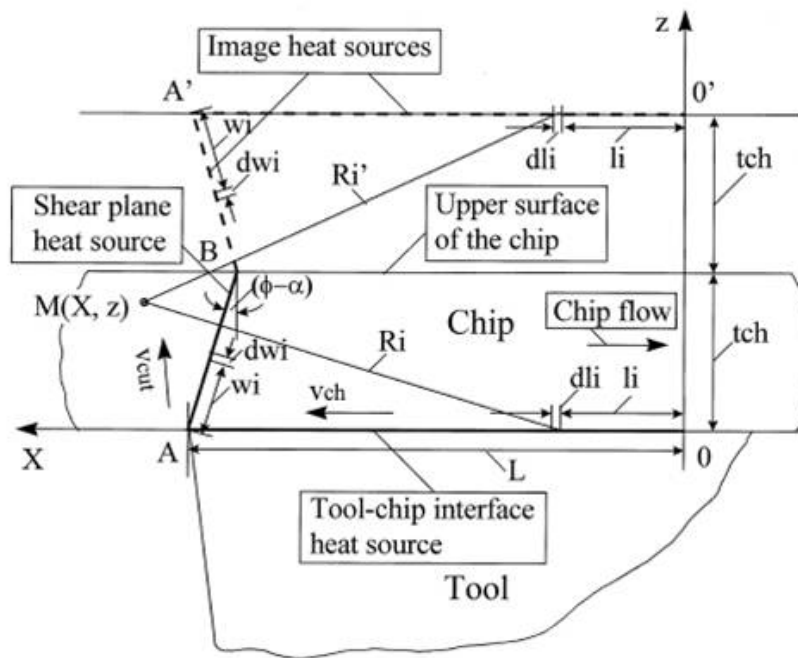
Figure 2.2: Schematic of the heat transfer model with a common coordinate system for the combined effect of two principal heat sources [77]

MC methods alone. The MCSD method was applied to the nanometric cutting of single-crystal aluminium along the (100) plane with different rake angle tools at a cutting speed of 5 m s^{-1}.

A solid foundation has been laid by various researchers in the field of simulating nanometric cutting, but not much work has been done in understanding the mechanism of tool wear involved during machining. The following section covers the work done in understanding the tool wear so far.

2.4   MD simulation of tool wear mechanism

Maekawa and Itoh [68] conducted MD simulation of nanometric cutting of copper with a diamond tool. They reduced the cohesive energy of the tool and showed that bonding of
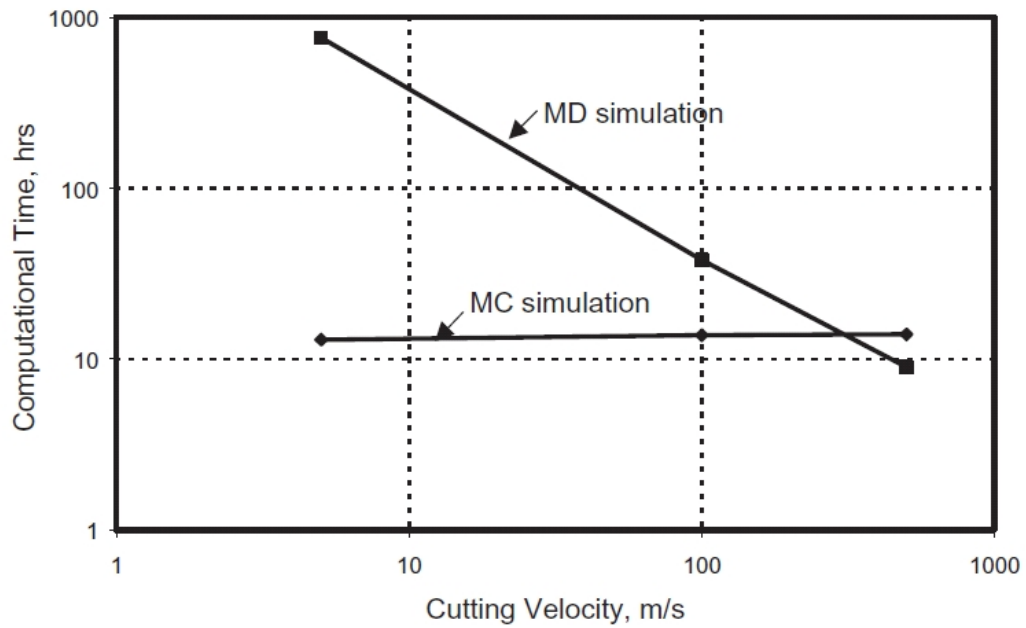
Figure 2.3: Comparison of computation time between MD and MC simulation [76]
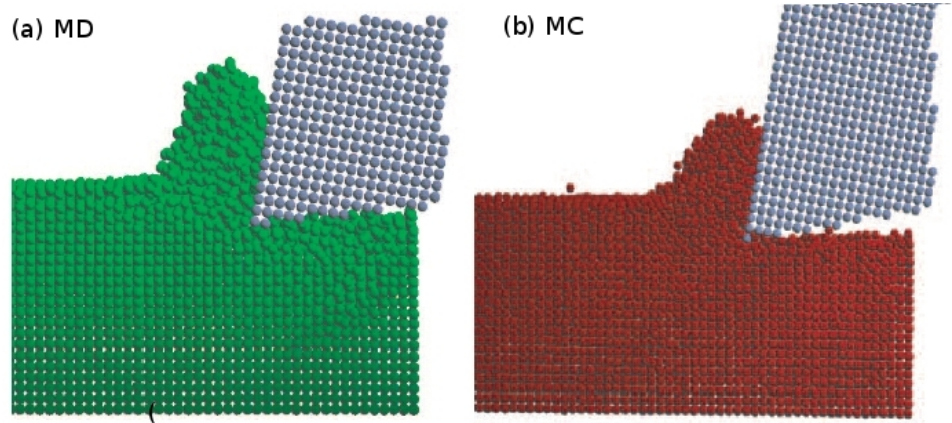
Figure 2.4: Comparison between (a) MD and (b) MC simulation under identical cutting conditions [76]

the tool atoms at specific sites become weak allowing the workpiece atoms to penetrate. This action promotes separation of atoms from the tool surface. The separated tool atoms tend to occupy another site on the tool creating a different structure thus establishing a

correlation with graphitization.

Belak [79] investigated machining of silicon using a deformable diamond tool at a cutting speed of 540 m s^{-1}. He reported that a layer of atoms from the workpiece was transferred to the diamond tool. He also reported that the silicon in the chip and the first few layers of the newly cut surface appeared amorphous and attributed this to the fact that the energy requirements for transformation of the crystal into an amorphous solid is less than that required to shear the crystal.

Perry and Harrison [80] investigated friction between two diamond surfaces under sliding contact using MD simulations. They reported that friction between two hydrogen-terminated diamond (111) surfaces is significantly reduced when methane molecules are placed between the diamond surfaces compared to the same two surfaces in the absence of the debris, or third-body, molecules.

Zhang and Tanaka [81] investigated the mechanism of wear and friction in diamond-copper sliding system using MD simulations. They observed that there generally exist four distinct regimes of deformation, i.e. the no-wear regime, adhering regime, ploughing regime, and cutting regime. They concluded that the transition between these regimes is governed by key sliding parameters, such as indentation depth, sliding speed, and surface lubrication conditions.
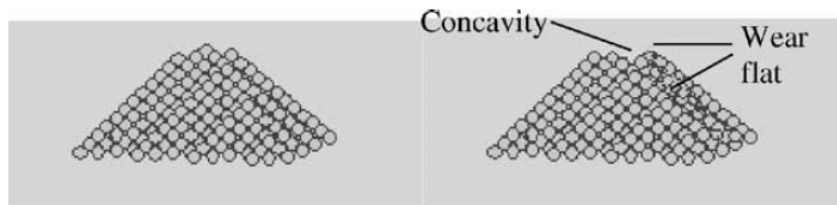
Figure 2.5: Diamond tool (a) before, (b) after, machining silicon [82]

Recently, Cheng *et al.* [82] have modeled tool wear of diamond machining silicon.

This was achieved by incorporating the assumption that cutting energy is completely transformed into the heat energy. They used MEAM potential for diamond as well as for silicon. The validity of using MEAM for diamond and silicon is somewhat questionable. Indentation followed by scratching was performed with a tool model simulating AFM tip. They observed diffusion of silicon and carbon atoms at the cutting edge of diamond tool. They also observed that wear initiates at the cutting edge. They experimentally validated the wear rate observed in the simulation and found a difference of ∼11.5%. They concluded that a thermo-chemical mechanism is the basis for tool wear.

2.5   Structural transformation in carbon

Structural transformations of diamond, Lonsdaleite (hexagonal diamond), and graphite occur under the appropriate conditions of pressure and temerpature and a suitable catalyst. Among the references available on the literature on these mechanisms, only mechanism pertinent to this investigation, the conversion from diamond to graphite or vice versa has been covered in some detail (Section 2.6), other mechanisms are discussed only briefly in this section. Bovenkerk *et al.* [14], Bundy *et al.* [83], DeCarli and Jameison [84], and Bundy [85] have reported the transformation of graphitic carbon into diamond.

Trueb [86] reported the formation of diamond from graphite in cast iron by an explosive shock process. Bundy and Kasper [87] have shown that crystallized graphite can be transformed to hexagonal diamond under a static pressure of more than 130 kbar and temperature greater than 1000 $°C$.

Yagi *et al.* [88] have reported the transformation of graphite into hexagonal diamond at room temperature under high pressure. He *et al.* [89] showed the transformation of diamond to hexagonal diamond under shock pressure waves in the range of tens of giga Pascal and temperature hundreds of Kelvin.

Recently, Irifune *et al.* [90] have developed polycrystalline diamond from graphite by heating a pure graphite rod at temperatures of 2300 $^\circ C$ - 2500 $^\circ C$ and at a pressure of 12-25 GPa.

2.6   Graphitization of diamond or vice versa

2.6.1   Experimental work

Graphitization of diamond was reported in the literature dating back to 1847. It has been an active field of research for many researchers [19, 91, 92]. Friedel and Ribaud [93] noted graphitization as a surface phenomenon. They also reported the bursting and disintegration of diamond at temperatures of $\sim$1900 $^\circ C$.

Bridgman [94] conducted experiments to synthesize diamond from graphitic precursors. Even though diamond is thermodynamically unstable, he observed that the graphitization of diamond can be restricted by applying a pressure of 30,000 kg/cm^2 and temperatures above 2000 $^\circ C$ in the presence of a catalyst, molybdenum. He reported that at the temperatures above the melting point of molybdenum, the rate of diamond to graphite transformation is a function of pressure.

Grenville-Wells [95] observed using X-ray diffraction that the crystallized graphite planes have a preferred orientation such that the graphite basal planes were parallel to (111) surface or in other words the *c*-axis of the graphite plane is in the $<111>$ direction.

Phinney [11] showed that graphitization of diamond can be divided into three regimes under vacuum or inert atmosphere. The first regime occurs in the temperature range below 1200 $^\circ C$. In this regime, no graphitization was observed. In the temperature range of 1200 $^\circ C$ to 1300 $^\circ C$, graphitization is restricted to a fine thin surface layer. In the third regime, above 1300 $^\circ C$ rapid graphitization takes place. He also reported that diamond powder graphitized in the temperature range of 50 $^\circ C$ to 100 $^\circ C$.

Rodewald [96] argued against the graphitization theory that because of the huge dissimilarities in the physical and electronic structures of diamond and graphite, a direct transformation from diamond to graphite is not possible. He calculated activation volume for the graphitization process and reported that the difference in molar volumes of graphite and diamond is much less.

Seal [97, 98] concluded that diamond can be deformed plastically at a temperature of 1800 $°C$ even though diamond is very brittle and hard at room temperature. This is because of the stresses generated due to the expanding nucleus of graphitization at high temperatures. He reported that the nucleation of graphite and the plastic deformation of diamond above the temperature vary from diamond to diamond in the range of 1600 $°C$ to 1800 $°C$. He observed no evidence of high percentage of rhombohedral graphite when he examined graphitized diamond by x-ray diffraction. He observed cubic intermediate structures which he later rejected upon further investigation [98].

Evans and Sauter [99] investigated etching of diamond surfaces with gases. They concluded that in the temperature range of 900 $°C$ to 1400 $°C$, graphitization is due to the deposition of carbon on the diamond surface as a result of surface chemical reaction and not because of pure physical phase change. They observed that the graphite formation is not only depended on the temperature but also on the surface and pressure of the air surrounding diamond. They concluded that carbon deposited on the diamond surface is by a secondary chemical reaction in which carbon monoxide reacts with the oxidized diamond surface given by the following equation:

$$CO + (CO) \longrightarrow CO_2 + C \tag{2.45}$$

They also suggested that diamond can graphitize in the presence of carbon dioxide in a similar fashion, and the primary equation of this mechanism is:

$$CO_2 + CO \longrightarrow CO + (CO) \tag{2.46}$$
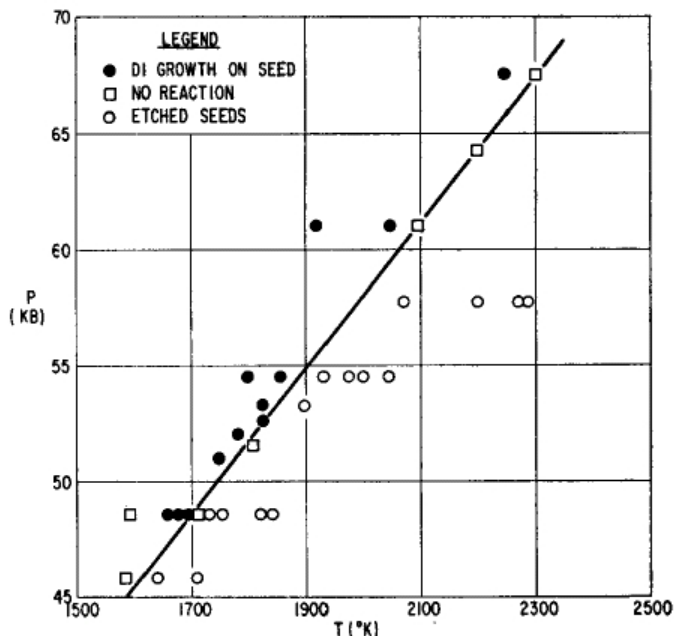
Figure 2.6: The temperature and pressure conditions for the dissolution and growth of diamond [100]

Bundy *et al.* [100] investigated the diamond-graphite equilibrium line from the point of view of growth of diamond and graphitization of diamond. They supported the view that because of the difference in the crystallographic structure of diamond and graphite, an intermediate state of a disorganized vapor-like state may be formed during graphitization. They observed that there is a definite high-temperature limit to the diamond-synthesis zone which on exceeding, results in the dissolution and graphitization of diamond (Figure 2.6). This temperature increases linearly with pressure. They also reported that the results on graphitization of diamond without a catalyst also fall in the same line.

Howes [101] performed experiments on diamond at temperatures of 1700 $^\circ C$ and above in high vacuum. He observed graphitization both internally and on the surfaces of dia-
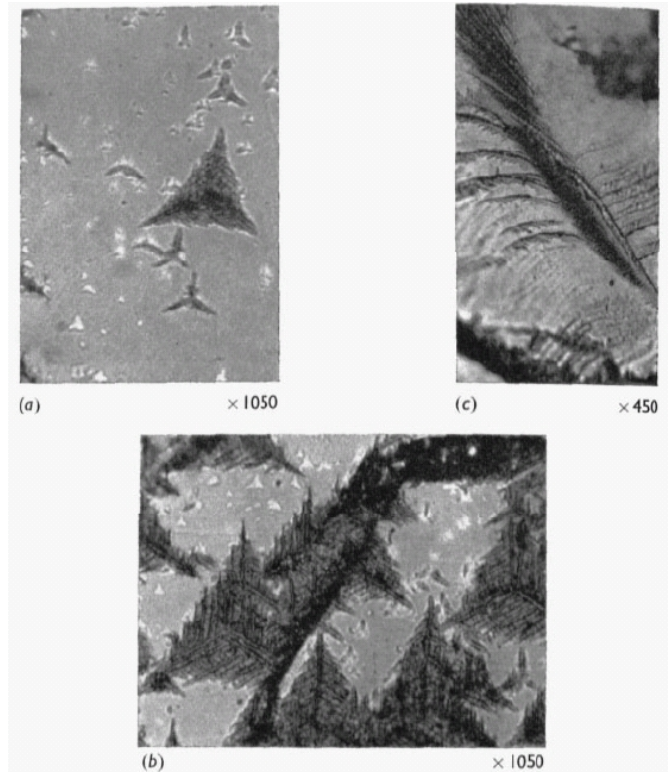
Figure 2.7: (a) and (b) Graphite nuclei on the surface of diamond, (c) nuclei formation on the cleavaged surface of diamond [101]

mond. He concluded that this is due to a physical phase transformation and defects which are present in the diamond (Figure 2.7). He conjectured that graphitization occurrs more rapidly at the <110> edges than at the (111) faces. While explaining the cause, he suggested that the atoms at the edges are weakly bonded and would break first than the ones strongly bonded on the surface. He added that breaking of an atom along the <110> would leave atoms, on either side, with double bonds which are again prone to transformation. On the other hand, breaking of an atom from a (111) surface would leave atoms which are triply bonded, which would be less susceptible to the transformation. He reported that the surface graphitization, unlike internal graphitization, increased with time and temperature. He also suggested that the a spacing of the graphite (2.47 Å) is very close to the atomic spacing in the <110> direction of diamond (2.52 Å) and this could be the path for the graphitization.
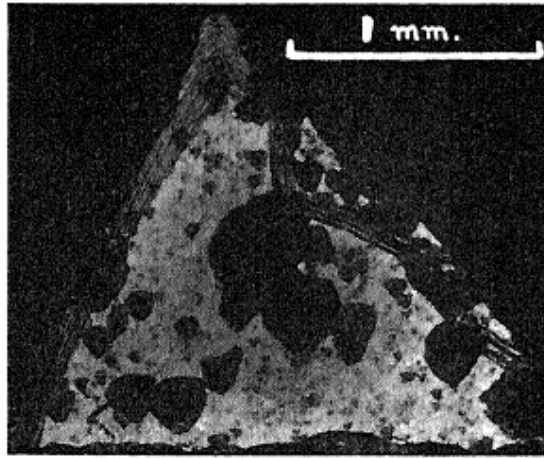
Figure 2.8: Optical micrograph of natural diamond (111) face after graphitization at 1800 $°C$ [102]

Seal [102] investigated the wear of diamond along different orientations and has shown that the (001) faces of diamond are most resistant to high temperature thermal graphitization whereas (110) planes are the least resistant. He also pointed out that the directions of fastest and slowest graphitization are the same as those of the fastest and slowest growth of diamond respectively. Similar conclusions were drawn by Field [21] that at high temperatures graphitization of diamond show different activation energies for different diamond surface planes.

Evans and James [103] studied the transformation of diamond with (111) surfaces to graphite by heating the diamond fragments in vacuum in the temperature range of 1500 $°C$ - 1900 $°C$. They observed no graphitization below 1500 $°C$ and a very rapid rate above 1800 $°C$. They observed that during the initial stages of graphitization the c-axis of graphite was oriented perpendicular to the underlying (111) surface and a-axis parallel to <110> direction, but after heavy graphitization the c-axis is oriented in a cone around <111> direction of the diamond surface. They proposed that groups of carbon atoms detached from

diamond surface condense back to from graphite. But later they modified their conclusion based on the theory proposed by Davies and Evans [104] which is described in the next paragraph.

Davies and Evans [104] investigated the graphitization of diamond both at zero pressure (2 x 10^{-6} Torr) and at high pressures. They supported the view that the graphitization of diamond involves detachment of a single atom from the diamond surface to an intermediate activated state and then condensation of these atoms to graphite structure. They also suggested that the rate-controlling step for the graphitization of (111) surface is the breaking of three carbon-carbon bonds and for the (110) surface is the breaking of two carbon-carbon bonds.

Recently, Hu *et al.* [105] conducted experiments on the deposition of tetrahedral (diamond like) amorphous carbon films on silica surface in the temperature range of -253 $^\circ C$ and 300 $^\circ C$. They reported a higher percentage of graphitic structure in the films grown at cryogenic temperatures than at higher temperature. With the help of Raman spectra, they showed clustering of sp^2 bonds in the the sp^3 bonded matrix. They concluded that graphitization occurs at cryogenic temperatures.

Temperature is not the only cause of graphitization of diamond. In the presence of properly directed shear stress, diamond can transform into graphite. van Bouwelen [106] observed debris obtained from a wide range of polishing experiments performed on diamond along different planes and directions. He proposed that a chemical transformation (sp^3 bonding to sp^2 bonding) is induced by shear at the interface of sliding. Based on this, he explained the anisotropy in polishing in terms of anisotropy of the elastic constants of diamond.

Recently, Gogotsi *et al.* [12] have reported the transformation of diamond into graphite under pressure by paring diamond parer against diamond surface at room temperature.
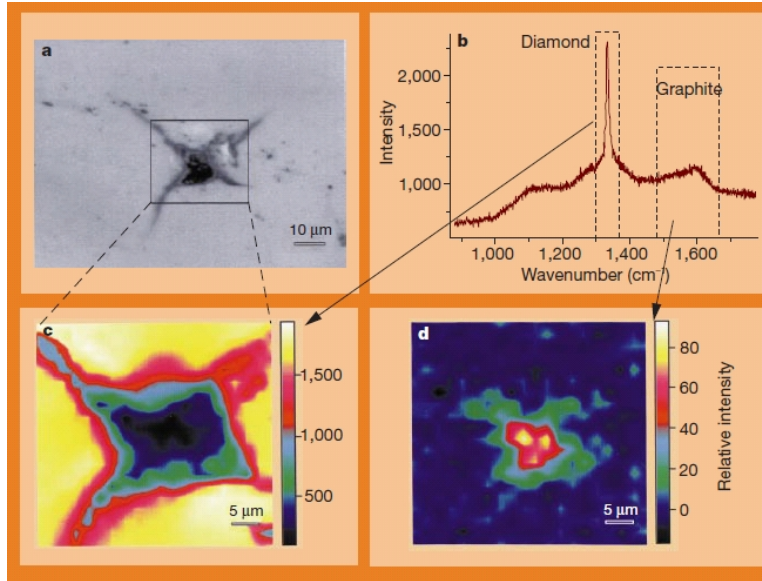
Figure 2.9: Raman analysis of indentation on diamond, (a) Optical micrograph, (b) Raman spectrum of the pared region, (c) and (d) Raman intensity map of graphite and diamond, respectively [12]

They observed that under non-hydrostatic compression, the transformation takes place at the point of indentation. Where the parer touched, the diamond surface, as well as the diamond parer, turned into graphite (Figure 2.9). They explained that during nanoindentation, the diamond is sheared along with having a change in volume. In other words, not only the carbon-carbon bonds are compressed but also the angles are changed during indentation [3]. This shear strain leads to a high compressive stress state in diamond which eventually leads to graphite formation. They suggested that graphite forms during unloading of the parer which is accompanied by an increase in volume. This was based on the observation that the whole pared area was slightly elevated above the surface which corresponds to increase in volume.

2.6.2 Theoretical work

Nath [107] proposed the first theoretical model to represent diamond to graphite transformation. He proposed that at high temperatures, the (111) diamond planes flatten, resulting in hexagonal planes and glide to form graphite. He suggested that this can be achieved by displacing the two cubic face centered in a particular direction, thus explaining the geometrical aspects of graphitization (Figure 2.10). He conjectured that there exists one and only one potential barrier between diamond and graphite stable states which can be crossed by either side by increasing the thermal energy of diamond/graphite, thus explaining the physical aspect of transformation.

FIG. 1.   FIG. 2.   FIG. 3.
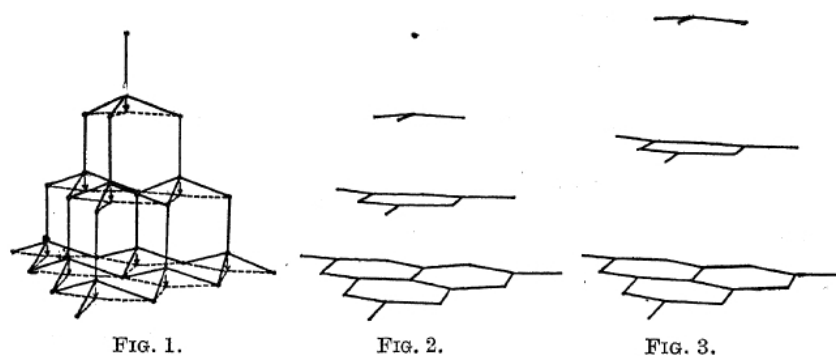
Figure 2.10: (a) Diamond structure, (b) α-pseudo graphite structure, and (c) β-pseudo graphite structure [107]

Badziag *et al.* [108] calculated the heat of formation of diamond and graphitic structures. Based on these calculations, they concluded that diamond, having a characteristic size of ∼3 nm, are not metastable. In this size range they are more stable than polyatomic form of carbon and they are energetically more favored than graphite in the presence of hydrogen because of the influence of C-H groups. However, this conclusion was criticized by Stein [109] who suggested that equilibrium constants are more appropriate measure of stability than energies and on this basis he found that diamond is always less stable than

graphite.

Kitabatake [110] simulated the transformation of graphite into cubic as well as hexagonal diamond using MD simulations using a Tersoff potential. This was achieved by compressing graphite along the *c*-axis.
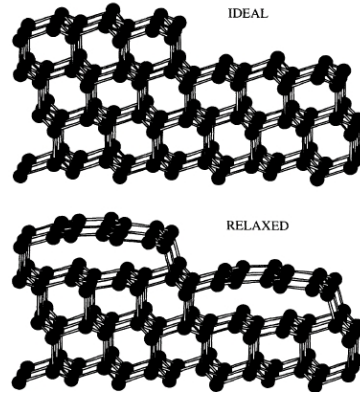
Figure 2.11: Graphitization of stepped (111) surface upon relaxation [111]

Davidson and Pickett [111] studied relaxation of a stepped (111) diamond surface using tight-binding method. They found that diamond (111) surface near steps graphitizes which is accompanied by a large increase in the spacing between the surface layers (Figure 2.11). But, graphitizaiton reverts to sp^3 bonding in the presence of H atoms. Hence, they suggested that this stepped surface could be a region where diamond nucleation can occur.

Jungnickel *et al.* [112, 113] conducted studies on the diamond (111) surface reconstruction as well as the graphitization process using tight-binding method. They observed that the ground state of the flat (111) surface is not graphitic but the 2 x 1 Pandey π-bonded chain model, diamond (111) surface graphitizes at high temperatures (Figure 2.12) instead of going to 2 x 1 reconstruction. They also suggested that both the structures can coexist on the diamond (111) surface.

DeVita *et al.* [114] studied microscopic model for surface induced graphitization of diamond. They started with the 2 x 1 Pandey π-bonded chain reconstructed (111) surface
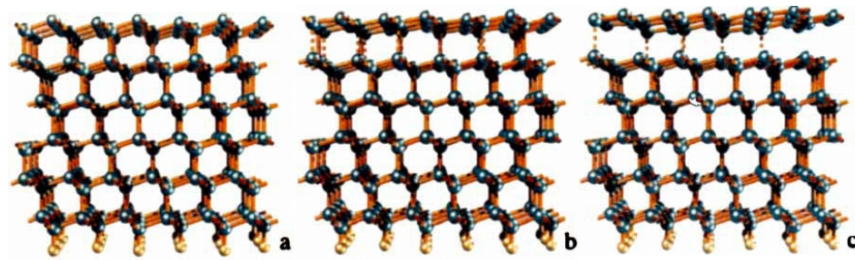
Figure 2.12: Structure of 111 diamond surface (a) at 0 K, (b) after 0.6 ps at 1200 K, and (c) after 0.8 ps at 2700 K [112]
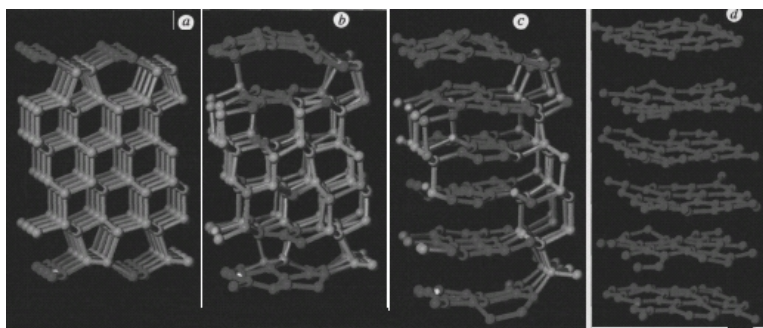
Figure 2.13: (a) 2 x 1 surface at 0 K, (b) a strained graphitic seed is formed at the surface after ~0.1 ps, (c) penetration of graphite into diamond slab after ~0.3 ps, (d) complete graphitization of diamond ~0.5 ps [114]

and showed a direct transformation of diamond to graphite for temperatures more than 2500 K with the help of *ab initio* MD. They reported that during the graphitization process, the graphite phase penetrates into diamond before full graphite planes are formed; hence a diamond-graphite interface is created during the graphitization process. Similar simulations were obtained by quenching the system to 1900 K, but only after the nucleation of the initial graphitic seed at 2500 K (Figure 2.13). They reported that despite the dissimilarities in the electronic and physical structures of diamond and graphite, a direct transformation was observed from diamond to graphite. They reported the total time taken for complete graphitization to be ~0.5 ps.

Similarly, Saada *et al.* [115] and Bródka *et al.* [125] have observed graphitization of

44
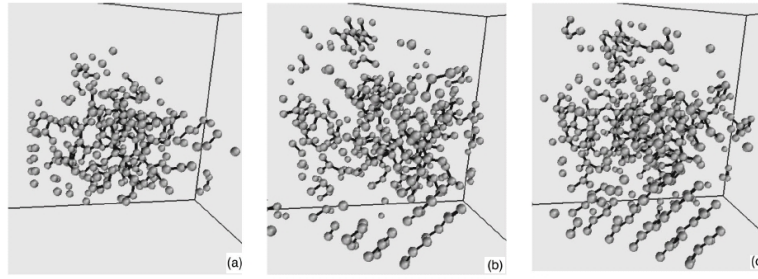
Figure 2.14: Evolution of the structure of the sample during annealing at 3000K, (a) before annealing, (b) after 16.25 ps, (c) after 20 ps, formation of graphitic planes [115]

diamond with the help of MD simulations. Saada *et al.* [115] have studied the damage in diamond due to ion impact and its annealing. They observed graphitization at 3000 K for simulation times up to 20 ps (Figure 2.14). A Tersoff potential was used for the simulation. On the other hand, Bródka *et al.* [116] have found that diamond transforms to graphite at temperatures as low as 1500 K with the total simulation time of 2.25 ns (Figure 2.15). They have used the reactive empirical bond order (REBO) Brenner potential for their simulation.
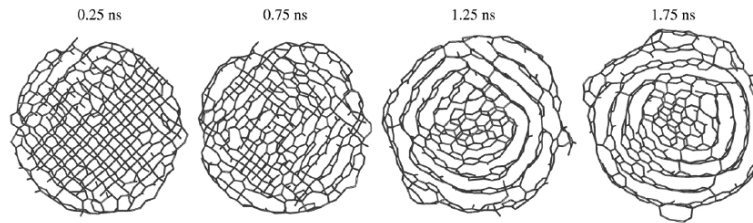
Figure 2.15: Arranangement of carbon atoms at T=1600 K at different time steps [116]

Jeschke *et al.* [117] presented a theoretical model to investigate ultrafast phase transition in diamond induced by a femtosecond pulse laser. They used MD simulation on time dependent potential-energy surface derived from a microscopic Hamiltonian. They

reported ultrafast ($\sim$100 fs) diamond to graphite transition that takes place over a wide range of laser pulse durations and intensities. They attribute this to the suppresion of the diamond minimum energy-surface due to the laser excitement.

2.7 Diamond growth and orientation relationships between diamond and graphite crystal structures

Angus *et al.* [118, 119] reported the deposition of diamond on natural diamond powder from methane gas at 1050 $^{\circ}C$ and 0.3 Torr. No specific mechanism for the diamond growth was described. However, a likely mechanism was proposed that methane reacted with the diamond surface resulting in the deposition of carbon atoms forming diamond.

Sunkara *et al.* [120] proposed that graphitic intermediate serves as a precursor for diamond nucleation. Hydrogenation of these graphitic intermediates, by atomic hydrogen to saturated states, serves as sites for diamond growth.

Angus *et al.* [121] reported that diamond can be grown by chemical vapor deposition (CVD) process. This was achieved under the metastable conditions of diamond. They reported that atomic hydrogen plays a major role in mediating rates and in maintaining a proper surface growth. They proposed that the nucleation of diamond crystals can proceed through a graphitic intermediate or from the diamond debris, directly from the carbon in a vapor phase.

Angus *et al.* [122] proposed a mechanism of nucleation of diamond from the gas phase through a graphitic intermediate. Since the corrugated hexagonal rings in the diamond (111) plane have the same spatial orientation as the flat hexagonal rings in the graphite (0001) plane, by energy minimization calculations they determined that a low energy interface was formed when three (111) diamond planes are joined to two (0001) graphitic planes. The model reactions proposed here involve the sequential conversion of monatomic

46

gas-phase carbon species to aromatic sp^2 bonded species, to saturated sp^3 bonded species by reaction with atomic hydrogen.
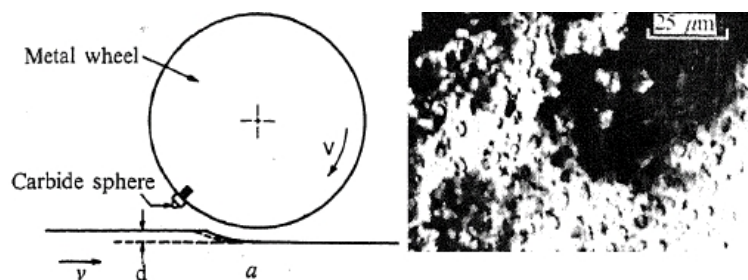
Figure 2.16: (a) Experimental setup, (b) scanning electron micrograph of inner layer of nickel showing possible diamond nuclei [7]

Komanduri and Shaw [7] proposed a novel method for the nucleation of diamond from graphite precursors. They coated tungsten carbide spheres with alternate layers of nickel and graphite and mounted them on an aluminum disk (Figure 2.13 (a)). They used this wheel to grind steel. Due to high temperatures ($\sim$2000 $^\circ C$) and high pressures (2 x 10^6 lb in^{-2}) and in the presence of nickel, graphite was reported to have transformed into diamond. They also suggested that the graphite formed by wear of diamond during grinding may be reconverted to diamond in the presence of nickel (Figure 2.13 (b)).

Komanduri and Nandyal [123], grew polycrystalline diamond aggregates from graphite for abrasive applications using the combustion synthesis technique. They mixed graphite power in a silver conducting cement and placed the mixture on a molybdenum substrate. The test procedure included initial nucleation and growth of diamond for about 2 hrs followed by a brief oxidation (for about 5 min). This was followed by further growth for an hour. Oxidation was done to etch the diamond crystals to provide the cube morphology suitable for grinding applications.

Li *et al.* [124] studied diamond growth on synthetic graphite and on substrates covered with graphite powder. They concluded that there was a preferential epitaxial relationship
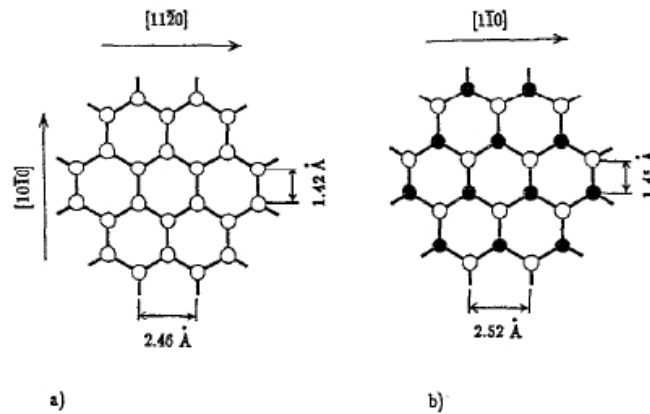
Figure 2.17: Atomic arrangement of carbon depicting correlation between different orientation in a diamond lattice [124]

between chemical vapor deposited (CVD) diamond and graphite substrate; the diamond (111) plane and graphite (0001) plane are parallel, and the diamond $<110>$ direction is parallel to the graphite $<11\bar{2}0>$. They also concluded that diamond can nucleate with an epitaxial relationship to the graphite which means that the corrugated hexagons in the diamond (111) plane retain the same orientation as the basal planes of the graphite (Figure 2.17).
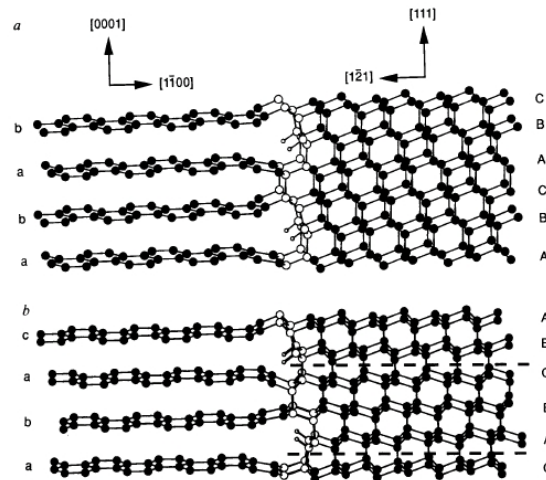
Figure 2.18: Correlation between diamond and graphitic plane [125]

Lambrecht *et al.* [125] proposed that diamond can nucleate from the initial condensation of graphite and subsequent hydrogenation of (1100) prismatic planes along the edges of the graphite particles with an almost perfect interface between graphite and diamond nucleus (Figure 2.18).
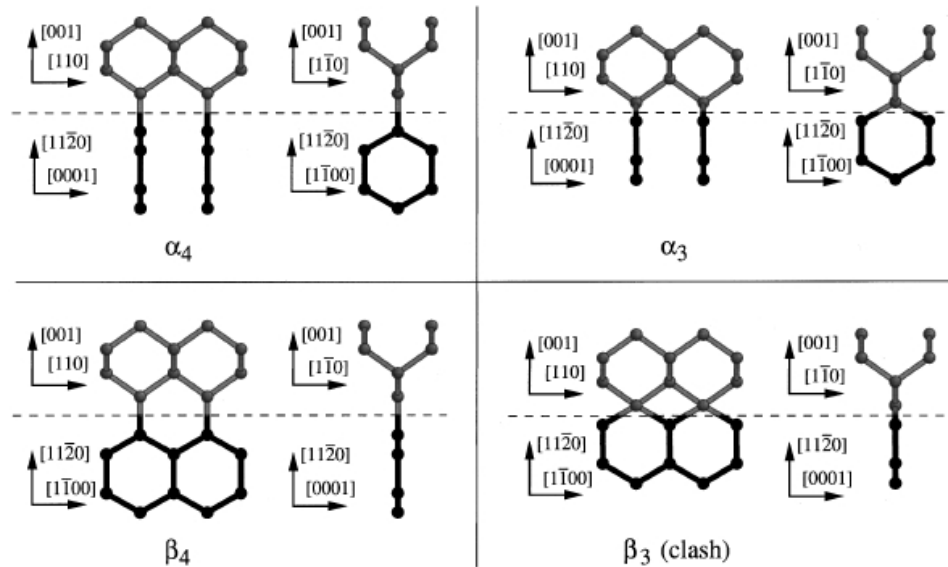
Figure 2.19: Four possible matches between a (001) diamond surface and graphitic planes [126]

Sternberg *et al.* [126] conducted *ab inito* studies on diamond/silicon (001) interfaces with and without graphitic interface layers. They considered four possible matches between a (001) diamond surface and graphite planes (Figure 2.19). They concluded that due to internal stresses in the graphitic structure, the resulting interfaces are at a higher energy than the ones without graphitic interface.

2.8   Wear of diamond in machining and grinding operations

Bowden and Scott [127] investigated the wear mechanism of diamond in the machining of glass. They reported heavy wear of diamond during the sliding operation and reported

that wear of diamond is accompanied by the production of amorphous carbon. They reported traces of graphite on the sliding rack on the glass when electron diffraction photographs were taken (provided by M. Seal). They found no evidence of any traces of diamond, neither on the sliding marks nor in the loose wear product. So they ruled out mechanical abrasion as a mechanism of wear. They reported that in the presence of oxygen the wear rate was reduced, which they attributed to the lubricating properties of graphite in the presence of oxygen and reported high wear rate in the presence of nitrogen. So, they ruled out thermal oxidation as a mechanism of wear. They concluded that degradation of diamond to graphite or amorphous carbon may be the primary cause of wear.

Seal [128] investigated abrasion of diamond against diamond. He reported a difference in behavior at high and low speeds and attributed these reactions to thermally activated chemical effect. He suggested that due to the generation of high local temperatures, graphitization may be the cause of wear.

Loladze and Bokuchava [129] proposed that wear of diamond was due to diffusion of carbon atoms into steel at high local flash temperatures generated during machining. They performed diffusion couple tests by paring a conical diamond into iron and heating them to 1300 $^\circ C$ for 0.5 sec. They reported a diffusion layer of 80 μ m. Although it was a static test, it clearly demonstrated the strong affinity of carbon for iron, forming iron carbide.

Ikawa and Tanaka [10] proposed a possible wear mechanism of diamond in grinding of ferrous materials. In single grit grinding, they reported that the diamond tends to wear out more easily by iron than by other materials, such as nickel or brass, in spite of the fact that hardness of the other two metals is more or less same as that of iron (Figure 2.20). They concluded that wear of diamond is governed by a thermal or possibly a chemical process rather than a mechanical process. They argued that if a mechanical process is the main mechanism of wear, then the wear curves for the three metals would lie close to each other, which was not reported. They also conducted etching tests in vacuum of 2 x 10^{-3} Torr and
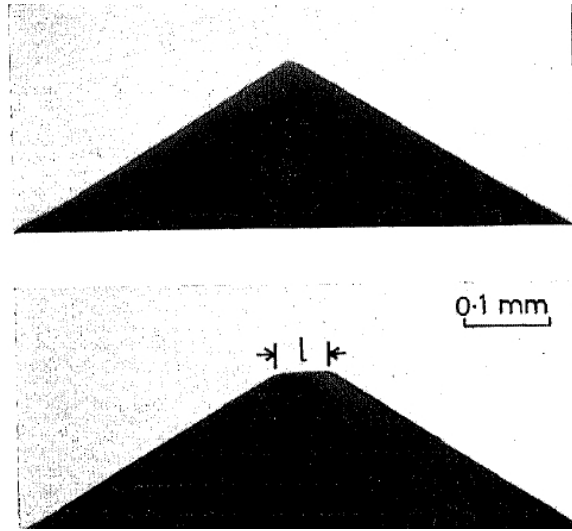
Figure 2.20: Diamond tool profile, before and after the test [10]

reported that the diamond surface graphitizes only in the presence of iron powder but not in the presence of air, iron oxide, copper powder, alumina, and nickel powder. They also performed diffusion tests and reported that diffusion of carbon in iron is accompanied by the graphitization of diamond at the contact surface.

Keen [130] investigated into the wear mechanism of diamond in the machining of Al-Si alloy used for automobile piston. He suggested that microcracking of the surface during polishing of diamond may be the cause of wear. Crompton *et al.* [131] deduced the relation between hardness and the rate of wear of diamond tool. They reported that when the hardness of the workmaterial is high enough, the tensile stresses acting on the diamond reach the fracture stress, and the wear becomes visible quickly. They attributed the wear of diamond tool to abrasion and attrition.

Tanaka and Ikawa [13] investigated the wear mechanism of diamond in grinding mild steel. They conducted diffusion tests and based on the results concluded that diffusion of carbon into steel is accompanied by the graphitization of diamond at the contact surface. Along with diffusion, they also observed a greater quantity of graphite at the surface of

51
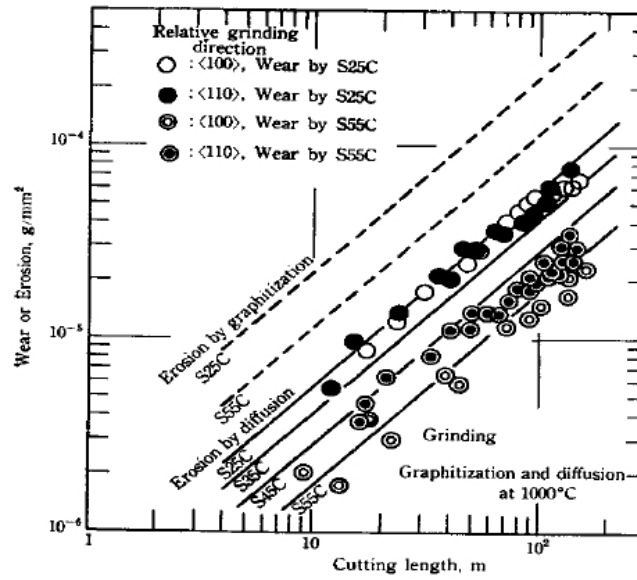
Figure 2.21: Comparative representation for wear in grinding test and erosion in diffusion couple test [13]

diamond when in contact with steel of lower carbon content than for that of steel of higher carbon content. They reported greater wear in <110> direction than in <100> on the (100) planes of the diamond grinding steels with lower carbon content (Figure 2.21).

Vishnevskii and Lysenko [132] reported graphitization of diamond and diffusion of carbon into iron along the diamond-iron interface during machining of low carbon steel and other alloys containing iron. Diffusion rates for various iron-carbon systems over a temperature range of 800 °C to 1100 °C were calculated and compared with the data on kinetics of the graphitization of diamond in the presence of iron. Vertman and Samarin [133] showed that dissolution of graphite can be categorized in two stages: (1) a phase-boundary reaction at the interface leading to the dissocation of carbon atoms, (2) a mass transfer through adjacent boundary into the bulk system.

Komanduri and Shaw [8] simulated grinding of steel using a well developed, single crystal, synthetic (cubo-octahedral) diamond crystal mounted on an aluminum disk. They
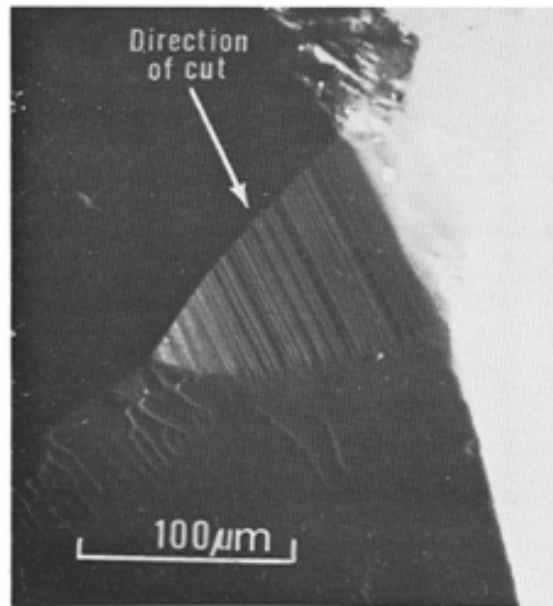
Figure 2.22: (a) Graphical representation of saw-tooth markings, (b) Micrograph of the wear area of a diamond grit [8]

concluded that under the catalytic effect of iron, high temperature, high shear stress, and low contact pressure (relative to the diamond stable region) diamond is first transformed into graphite and subsequently removed from the surface of the diamond. They ruled out oxidation as the predominant mechanism of wear. They proposed that since diamond is in a metastable state at room temperature it will transform to graphite under the appropriate conditions of temperature and pressure. High temperatures, shear stresses, and presence of chemically active materials will carry diamond further away from the equilibrium, considering that all these conditions exist under the clearance face. They suggested that diamond is relatively insoluble in molten iron (a key point in diamond synthesis [**?**]) and hence diamond does not directly react with iron. However, once diamond graphitizes, it rapidly reacts with iron forming iron carbide. They reported preferential etching of diamond on {110} planes while grinding ferrous materials [Figure 2.22(a)] which is consistent with the graphitization theory. They reported rapid crater wear on the diamond abrasive in grinding [Figure 2.22 (b)].

Komanduri and Shaw [9] extended their work on the wear mechanism of diamond by studying the chemical interaction between diamond and iron. With the help of Auger electron spectroscopy, they reported a 160 Å diffusion layer in grinding of iron with a single crystal synthetic diamond. They found iron carbide (Fe_3C) and iron oxide at the surface where grinding was done. They concluded that graphitization of diamond precedes diffusion. They reasoned that the carbon atoms are held much more tightly in a diamond lattice than in the graphite structure, although iron-carbon complex formation provides an alternate path. For this, diamond has to graphitize first before it can diffuse. They also reported that with increasing depth of cut, the proportion of iron oxide decreases. They also performed diffusion couple tests and reported results in excellent agreement with the diffusion theory (Figure 2.23).
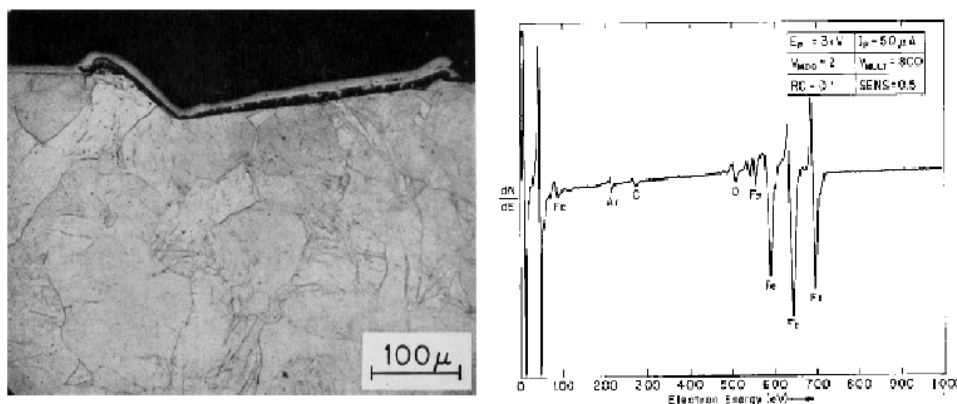
Figure 2.23: (a) Micrograph of pure iron showing the cross section of the groove, (b) Auger spectra of the machined iron [9]

Thornton and Wilks [15] provided an insight in the prevailing conditions at the interface between the tool (diamond) and the workpiece (mild steel) during machining. They calculated wear rates of round-nose diamond tools turning mild steel under specified conditions. They concluded that clean surfaces have an enhanced chemical activity and play an important role in the wear of diamond. Because of the clean surfaces, reactivity of diamond with mild steel takes place at a low temperature.

54

Thornton and Wilks [16] investigated the wear of diamond tools while turning a mild steel workmaterial under a range of cutting conditions. They reported high rates of wear because of graphitization of diamond due to high local flash temperatures and catalytic action of steel and the atmosphere. They also concluded that during the machining process the nascent surface generated has different chemical activitiy than the bulk. They reported that wear of diamond in the machining of steel is steady and smooth when compared to the wear in the machining of molybdenum. In the latter case, fracture was reported.

Tanaka *et al.* [134] investigated the affinity of diamond towards several metals. They concluded that diamond shows very less affinity for soft non-ferrous materials. They reported that the affinity is dependent on the crystallographic orientation of diamond to form metal complexes. They reported {100} plane to have better wetting capabilities than {110} and {111} planes. They also reported heavy graphitization of diamond when heated with iron or mangnese powder.

Hitchiner and Wilks [135] investigated the factors affecting chemical wear of diamond tool in turning of steel, nickel, and graphite. They concluded that chemical wear during turning is greatly affected by changes in the gaseous environment and is strongly dependent on the chemical constituents of the tool as well as the workpiece. They showed that in the presence of hydrogen and methane, the wear of diamond increased during machining of steel. They reasoned that both the gases are known to be chemisorbed in iron. Hydrogen atoms bond to diamond which essentially leads to a reaction producing hydrocarbons. Grigoriev and Kovalsky [136], on the other hand, reported evolution of methane gas when a sharp diamond is placed in contact with iron or nickel foil in the presence of hydrogen environment.

Gangopadhyay and Tamor [137] reported wear of CVD-grown diamond films in the machining of steel. They did not find any particular mechanism for wear. They concluded that the wear of diamond film occurred due to fracture. They also reported evidence of

delamination of diamond surface, which may be attributed to the poor coating

Paul *et al.* [22] investigated chemical aspects of wear of diamond tool. They proposed a *d*-electron theory to explain the chemical wear of diamond. In this mechanism, the formation of carbon-metal complexes by unpaired *d* electrons from the workpiece with the carbon from the diamond tool producing wear. This hypothesis was used to explain a range of results for metals, such as group VII from the periodic table, alloys, such as mild steel, and other materials, such as "electroless" nickel. They elucidated that nickel, which has two unpaired *d*-electrons, is not diamond turnable. But in nickel phosphorus alloy (electroless nickel) *d*-electrons of nickel are paired with *p*-electrons from phosphorus atoms resulting in fewer unpaired *d*-electrons. Consequently, it forms fewer metal complexes resulting in less diamond tool wear.

Tanaka *et al.* [138] investigated the difference in wear patterns of diamond cutting tool on several workpieces, including iron, copper, and aluminum. They reported three different mechanisms of wear of diamond tool. In the first mechanism, they reported graphitization of diamond and subsequent diffusion of carbon atoms into the workpiece in the turning of iron or steel. The second, a two-step mechanism, namely, oxidization-deoxidization reaction was reported. In this, the workpiece is first oxidized by the ambient oxygen and then the oxide of the workpiece is deoxidized by the diamond tool. This mechanism was reported to be dominant in the machining of copper; they argued that if the cutting temperatures were not very high then this mechanism should also have been reported in the machining of iron. The third mechanism reported was the formation of carbide with the workmaterial along the cutting edge and on the flank face.

Sahajwalla and Khanna [139] developed a Monte Carlo model for the dissolution of graphite in iron-carbon melts in the temperature range of 1300 $^\circ C$ to 1600 $^\circ C$. They reported that a contact between graphite and melt resulted in the formation of a broad interfacial region containing high concentrations of C and Fe atoms. Hence, they concluded

that contact between graphite and the melt leads to dissociation of carbon atoms from graphite and their subsequent diffusion into the melt. Shabouk and Nakamoto [140, 141], on the other hand, used the phenomenon of wear of diamond in machining of iron to polish diamond by using hot ferrous materials. Uemura [142] investigated the probability of diamond-graphite phase transformation related to oxidation of carbon-hydrogen bonds on a diamond surface and analytically calculated the wear rate of the diamond tool.

2.9   Minimization of diamond tool wear

Casstevens [143] conducted diamond turning of steel in carbon saturated gaseous atmosphere, such as methane (CH_4), carbon dioxide (CO_2), carbon monoxide (CO), and ethyne (C_2H_2) in order to investigate diamond tool wear. He varied machining parameters, such as rake angle, nose radius, cutting speed, feed, and depth of cut along with gas pressure and purging times. There was no significant improvement in the diamond tool life in presence of CO_2. However, he reported that the wear of diamond suppressed in the atmosphere of methane (CH_4), which is opposite of what Hitchiner and Wilks [135] had reported. No explaination was provided for the mechanism postulated.

Evans [144] conducted cryogenic diamond turning of stainless steel to investigate wear of single crystal diamond tool. He concluded that at low temperatures, both diffusion and graphitization were slowed down. However, he reported that the experiments conducted were unable to explicitly differentiate between the mechanisms. He also reported that a considerable improvement in surface finish was achieved in diamond turned stainless steel.

Zhang [145] claims a method for extending the life of a diamond tool in machining a workpiece that chemically reacts with the diamond tool. In that, the surface electric potential of the workpiece is adjusted to inhibit chemical reaction between the diamond tool and the workpiece.

Kohlscheen *et al.* [146, 147] reported that the tool life of diamond can be increased in the machining of titanium (group IVB element) by adding nitrogen (TiN_x) to it. To explain the mechanism, they conducted *ab initio* calculation and reported that the covalent bonds formed between Ti and N are such that unpaired *d*-shell electrons in Ti are tied up by nitrogen and that is reported to be the reason behind the reduction of tool wear.

Sasaki and Saito [148] investigated wear models of frictional sliding between a diamond pin and a carbon thin film containing nitrogen using MD simulations. They developed Tersoff-type potential using genetic algorithm (GA) from the first principle calculations for nitrogen-nitrogen and carbon-nitrogen interactions. The carbon-nitrogen potential represents crystalline as well as amorphous carbonitride (β-C_3N_4) system. They reported that wear can be minimized by adding 20 - 30% of nitrogen into the thin film. They showed qualitative correspondence with the experimental results.

2.10   Quantum calculations based modeling of iron-carbon interaction

Häglund *et al.* [49] performed *ab initio* calculations on the orthorhombic unit cell of cementite using linear-muffin-tin-orbitals (LMTO) method. They calculated physical and chemical properties of cementite (Fe_3C) and found good agreement with the experimental observations. However, the cohesive energy per atom determined was 100% higher than the experimental value.

Häglund *et al.* [149] also performed *ab initio* calculations on transition-metal carbides and nitrides. They performed calculations on different 3*d*-, 4*d*-, and 5*d*- transitional-metal carbide structures, namely, M_3C_2, M_2C, M_7C_3, M_5C_2, M_3C, and $M_{23}C_6$. They concluded that the results on enthalpies of formation and cohesive energies are adequate factors to understand the trends in bonding energies among carbides. They reported that the enthalpy of formation for the carbides has a characteristic variation along a *d*-series. The enthalpy increases to a maximum value and then decreases followed by almost a constant value.
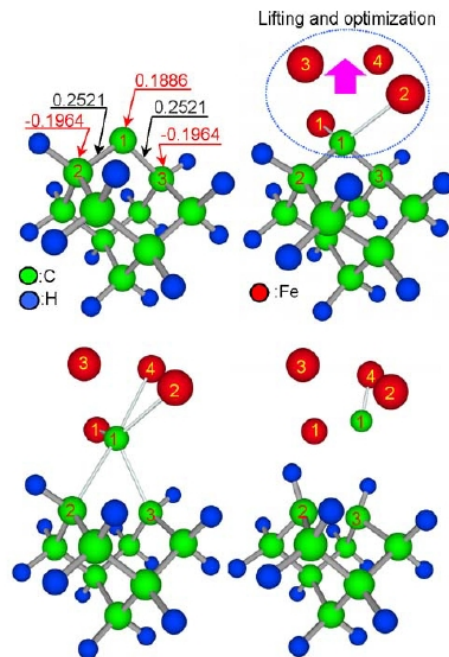
Figure 2.24: (a) $C_{10}H_{14}$ cluster model fo diamond (100) surface, (b) Interaction between Fe_4 cluster and most stable $C_{10}H_{14}$ configuration, (c) formation of Fe_4C under forced lifting, (d) Dissociated Fe_4C [150]

Shimada *et al.* [150] conducted erosion tests to simulate wear process and *ab-initio* molecular orbital calculations. They showed that the essential wear mechanism, at temperatures higher than 1000 K, is the dissociation of carbon atoms from diamond surface due to interaction with the iron surface. The wear rate was controlled by the removal rate of dissociated carbon atoms from the tool-work interface, such as diffusion into workpiece (Figure 2.24). At temperatures lower than 900K, the mechanism involved is the removal of carbon atoms due to oxidization of diamond accompanied with deoxidization of iron oxide.

Nash *et al.* [151] investigated the equilibrium structure and bonding of small iron-carbon clusters using self-consistent (HF-MP$_4$) *ab initio* molecular orbital theory. They reported that the structure of neutral FeC_n to be cyclic which is consistent with the experimental broadening observed in the photodetachment of FeC_n^{--} clusters.

Shim and Gingerich [152] investigated the nature of bonding in diatomic transition iron carbide (FeC) using multi-configuration self-consistent-field (CASSCF) *ab initio* calculations. They reported that the chemical bond in the FeC molecule can be described as a triple bond. The bonds are formed by valence bond couplings between Fe $3d\sigma$ and Fe $3d\pi$ with the C $2p\sigma$ and C $2p\pi$. They report that FeC molecule is polar with a diapole moment of 1.86 D in the $^3\Delta$ state and 1.51 D in the $^1\Delta$ and charge transfer from Fe to C.

Timoshevskii *et al.* [153] modeled Fe_8C and Fe_8N superstructures ($Fm\bar{3}m$) using *ab initio* calculations. They concluded that austenite can be simulated using the model they have proposed. They also reported that the chemical bond between Fe-C is highly covalent than Fe-N.

Chiou Jr. and Carter [154] performed gradient-corrected psuedopotential-based DFT calculations on bulk cementite (Fe_3C) and reported that these results are in good agreement with the experimental results. They reported that the local densities of state are predominantly metallic in character with some polar covalent bonding contributions (charge transfer from iron to carbon) for both bulk and surfaces with different orientations. They mention that the relatively greater stability of Fe_3C surfaces is the reason behind the formation of cementite at the surfaces of BCC iron.

Jiang and Carter [155] performed DFT calculation of carbon dissolution and diffusion in iron. They reported that the minimum-energy path for carbon diffusion is from one octrahedral site to another via a tetrahedral site (Figure 2.25). They reported that repulsive interacton between carbon atoms at high concentrations, consistent with the experiments and consistent with the tendency of carbon to precipitate out as Fe_3C into BCC Fe.

Ding *et al.* [156] conducted MD simulations to investigate the thermal behavior of $Fe_{N-m}C_m$ clusters. Based on their results, they concluded that, when carbon nanotubes (CNTs) are grown on large ($> 3 - 4$ nm) catalyst particles at below melting temperatures
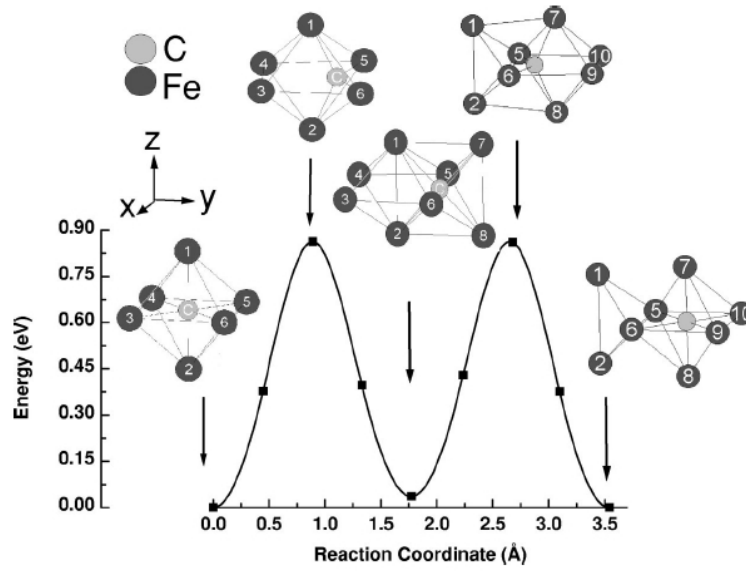
Figure 2.25: Minimum-energy path for carbon diffusion in the $Fe_{128}C_1$ super-

cell showing initial, intermediate, and final structures [155]

(<1200 K), the catalyst particles are not completely molten. Hence, they argued that, under

these conditions, the mechanism of CNT growth may be governed by the surface melting

of the cluster.

Weissmann *et al.* [157] investigated several properties of iron nanowires coated with

carbon from the first priciple calculations. They particulary focused on the effect of car-

bon's presence on the magnetic ordering of iron.

Shein *et al.* [26] investigated electronic and structural properties of cementite-type

M_3X, where M = Fe, Co, Ni; X = C or B, and reported that these structures are not ther-

modynamically stable. Most of the bonding is due to metallic state as well as metal-carbon

hybridized bonding.

Shibuta *et al.* [158] investigated the growth of single-walled CNT under the presenc of

transition metal. They developed many-body potential for transition metal carbide clusters

from the DFT calculations. They concluded that Co clusters have stronger graphitization
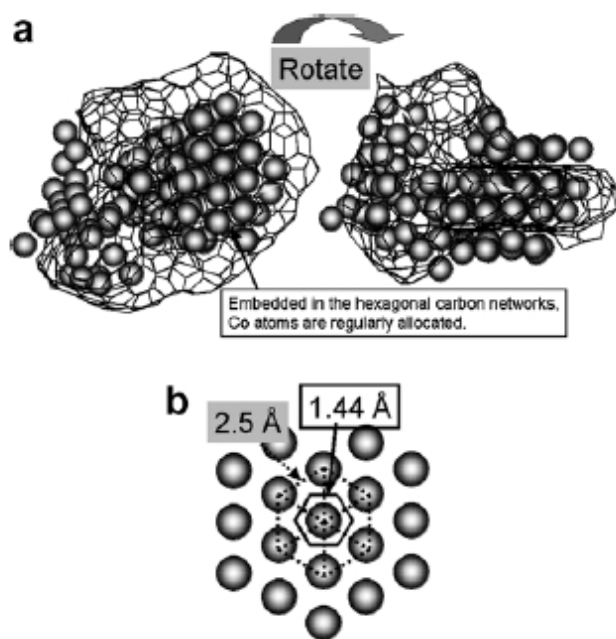
Figure 2.26: (a) Co atoms are regularly allocated and embedded in the hexag-
onal carbon network, (b) deptiction of the hexagonal rings [158]

than Fe clusters. They also reported that the transition metal embed into hexagonal network
of carbon to form hexagonal ring [Figure 2.26 (b)]. They reasoned that the minimum points
for the potential energy fields are distributed on the hexagonal network.

CHAPTER 3

PROBLEM STATEMENT

Ultraprecision diamond turning and grinding have now become common and established methods for manufacturing precision components. These methods are applicable to electronics, optical, and mechanical industries in the field of nanotechnology. This is because of the extraordinary features of diamond, such as high hardness (infact diamond is hardest of all materials known to human kind), its availability in single crystal form (with no grain boundaries), its ability to form an extremely sharp cutting edge, very high thermal conductivity, low friction, non-adhesion to most workmaterials, and high wear resistance [1].

But it is also a well known fact that diamond undergoes severe wear in machining ferrous materials, such as iron and low carbon steels [8]. This is because carbon has a strong affinity towards iron to form carbides, especially at high temperatures. The wear mechanism not only depends on the cutting and ambient conditions but also on the type of workmaterial used. This causes difficulty in understanding the underlying mechanism of wear and prohibits the application of diamond as an ideal material for a tool in nanometric machining.

A review of the literature indicated that there are several experimental results at microscopic level that conclude wear of diamond in machining iron to be chemical in nature. Various mechanisms were proposed explaining the chemical wear of diamond in the ma-

chining of iron. In this, diamond is first converted into graphite and subsequently reacts with iron to form iron carbide, a mechanism orginally proposed by Ikawa and Tanaka [10]. This mechanism was further supported by the works of various researchers. Loladze and Bokuchava [129] proposed that wear of diamond was due to diffusion of carbon atoms into steel at high local flash temperatures generated during the machining process.

Komanduri and Shaw [8, 9] suggested that since diamond is a metastable form of carbon, it can transform into graphite under appropriate conditions of pressure and temperature, but below the diamond-graphite equilibrium. During machining, the increase in temperature and pressure below the diamond stable region, existence of high shear stress at the cutting edge, and the presence of reactive material underneath the clearance face and at the tool-chip interface can promote graphitization.

Several studies have been reported in accordance with the mechanism proposed at the microscopic level, but only a few, if any, are available at atomistic level. Graphitization occurs at a time scale of picoseconds [12] and MD simulations become a suitable tool at this time scale. This motivated us to investigate the underlying mechanism of wear of diamond in the machining of iron at the nanometric level. This was achieved by performing investigations that require us to identify potentials that represent, (a) the chemical aspects of wear of nanometric cutting of iron with diamond tool, (b) the transformation of diamond into graphite, taking into account the physical properties of iron, diamond, graphite, and iron-carbide.

The next step was to investigate the reactivity between two different forms of carbon, namely, diamond and graphite and iron using diffusion couple tests at different temperatures. This was followed by conducting nanometric machining of iron with a diamond tool for different crystallographic orientations of the tool and also correlating the wear mechanism to diamond polishing and investigating the role of iron in the wear of diamond.

If the wear mechanisms are understood adequately, appropriate steps can be taken in order to reduce wear. This includes employing low cutting temperatures (sub-zero) and cutting fluids that can aid in suppressing the reaction between iron and diamond. Studies conducted on the cryogenic diamond turning of steel using liquid nitrogen reported a reduction in tool wear. This was attributed to the low cutting temperatures [144]. However, conflicting results have been reported for minimizing tool wear in the presence of different elements. For example, machining conducted in the presence of carbon-rich environment, such as methane, the wear of diamond is reported to be suppressed [143]. In contrast, at other times, an increase in the wear of diamond was reported in the presence of methane [135]. Similar outcome was reported for hydrogen [143].

To investigate the reduction of wear of diamond tool in the presence of various elements, such as diatomic and polyatomic gases (nitrogen, carbon dioxide, methane) using MD simulations, there was a requirement to obtain the analytical potential(s) that can be implemented for various crystal structures as well as gases. There were two ways to address this issue; one, modify the existing analytical potential, such as Tersoff to extend its application for several materials or the other, develop a method that is independent of any functional form. Both these methods involve generation of a database from *ab initio* calculations conducted on the material of interest.

To develop analytical potentials from quantum calculations, we can implement neural network (NN) which is a fitting tool [159]. With this in mind, a new method was co-developed for the parameterization of the analytical functional form with the help of NNs. This method allows the user to modify any parametric form to accommodate larger databases for accurate fitting. This was demonstrated over two different databases, namely, Si_5 and $O_2 + O \rightleftharpoons O_3$ for the Tersoff functional form.

If no functional form, such as Tersoff, was to be taken into consideration, we proposed a new approach to develop analytical potential based on multi-body expansion, neural net-

works, and moiety approximation. This method can be applied for heterogeneous as well as homogeneous systems so that materials can be simulated accurately. This proposed method was applied to three different systems, namly, (i) silicon, (ii) vinyl bromide, and (iii) iron-carbon clusters.

CHAPTER 4

REACTIVITY OF IRON WITH DIAMOND AND GRAPHITE, TWO ALLOTROPIC FORMS OF CARBON

4.1   Introduction

Diamond, the hardest known material is also known for its inability to machine ferrous alloys and low carbon steels causing significant tool wear. The most commonly accepted theory explaining the mechanism of wear is that diamond initially graphitizes and subsequently reacts with iron to form iron carbide [8–10, 13, 134, 138]. Many researchers have reported diffusion of carbon into iron and other low carbon ferrous materials by conducting diffusion-couple tests [10, 13]. Diffusion wear occurs when carbon atoms from the diamond surface detach and enter into hot iron chip. They demonstrated the affinity of carbon to react with iron, forming iron carbide. Carbon atoms occupy interstitial and/or substitutional vacancies in the workpiece (iron) until all the vacancies are saturated [160].

Ikawa and Tanaka [10] concluded that the diffusion of diamond in iron is accompanied by graphitization of diamond at the contact surface. Komanduri and Shaw [9] investigated the diffusion wear of diamond in grinding pure iron. Using Auger electron spectroscopy (AES), they observed a diffusion layer of 160 Å thickness. They concluded that graphi-

tization of diamond precedes diffusion. They reasoned that since the carbon atoms are held much more tightly in a diamond lattice than in the graphite structure, diamond has to graphitize first before it can diffuse. Although iron-carbon complex formation provides an alternate path.

In this chapter[*], we assume that diamond is first converted into graphite, and thus conforming to this hypothesis. This way a transformation path from diamond to graphite is explored. It is referred to as the diamond-graphite interface in our study. Graphite, not diamond, dissolves in molten iron and precipitates out as a diamond in the diamond stable region. This indicates that diamond does not react directly with iron. We would expect a similar phenomenon in MD simulations wherein diamond would not react directly with iron but graphite would.

To investigate the diffusion characteristics of carbon in iron, two different carbon structures were considered - (a) diamond-graphite interface, and (b) diamond. Angus *et al.* [121, 122] reported that diamond can be grown from the graphitic precursors under the metastable conditions of diamond. If diamond can be grown from the graphitic precursors, similar energy path could be present in the reverse direction, such that under proper conditions diamond gets transformed into graphite.

Based on Lambrecht *et al.* [125] and Jungnickel *et al.* [112, 113], Sternberg and Lambrecht [126] have conducted studies on diamond/silicon (001) interfaces with and without a graphitic interlayer. They considered four possible matches between a (001) diamond face and graphitic planes. For this study, one of the structures, β_3, was considered as a tool. Figure 4.1 shows this structure where green spheres are diamond atoms and red spheres are graphite. This structure has been considered in our study to accommodate the mechanism that diamond is first converted into graphite and subsequently this leads to the wear of the
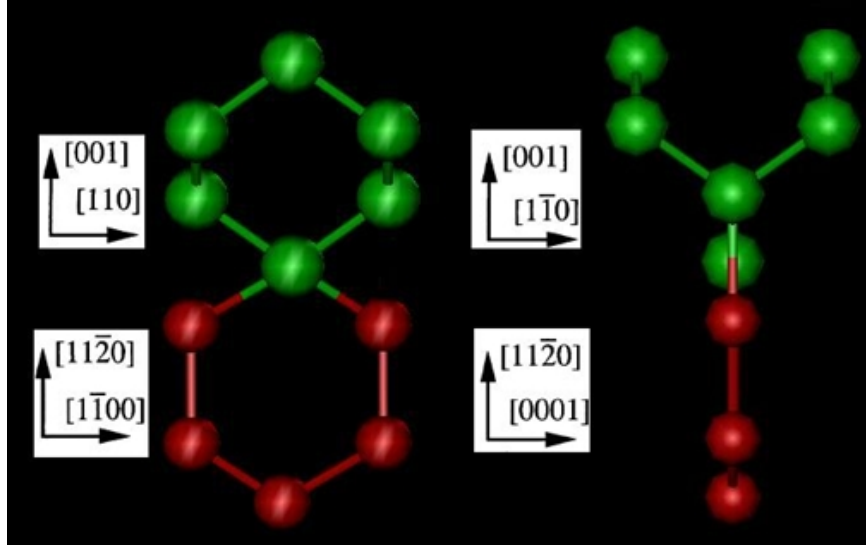
Figure 4.1: Structure of the diamond-graphite interface

tool.

Sternberg and Lambrecht [126] have reported a mismatch of about 2.6% between diamond and graphite planes. These are high energy structures compared to diamond without graphitic layers because of the strain produced in the graphite due to mismatch. However, we observed no significant deformation or rearrangements of carbon atoms at temperatures as high as 1600 K.

Simulations of diffusion-couple tests were conducted to investigate the diffusion wear of diamond tool in iron. The system requires potentials for Fe-Fe, C-C, and for the Fe-C interactions. EAM potential functional form developed by Daw and Baskes [43, 44] and REBO Brenner potential [41, 42] were used in this investigation.

4.2   Modeling

The workpiece and tool were initialized to a temperature of 300 K. They were initially separated by a distance of 9 Å (Figure 4.2). The carbon atoms are in green and iron atoms are in white. All the simulation images have been created using Visual Molecular Dynamics
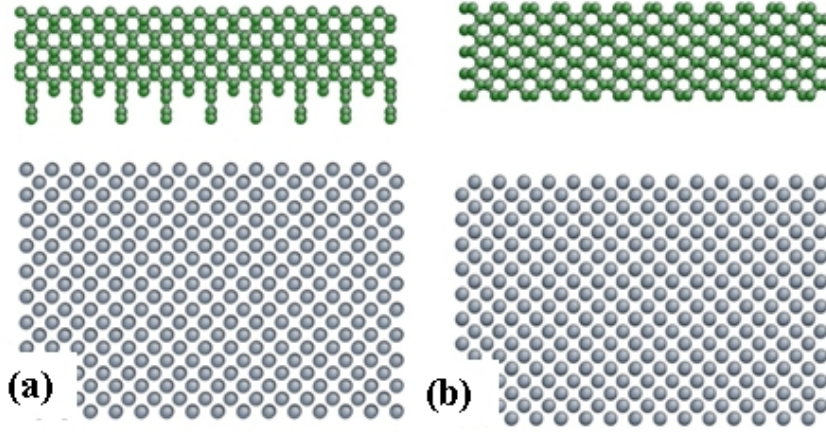
Figure 4.2: Initial configuration of (a) diamond-graphite interface and (b) diamond as a tool and iron as a workpiece

(VMD) software [161]. We have integrated XMD [162] and Brenner [163] codes that are available separately. In order to simulate diffusion wear, the entire process is divided into three steps,

Step 1 (S_1): The workpiece and tool were brought into contact with the temperature maintained at 300 K using a velocity reset function [162]. The workpiece was kept stationary while the tool was brought down at 500 m s^{-1} until the tool and workpiece were in firm contact. The bottom surface of the workpiece was kept fixed to restrain the vertical motion.

Step 2 (S_2): The system was heated to a temperature T by reassigning the velocities to the atoms. Random velocities were allocated to all the particles from the appropriate Maxwell-Boltzmann distribution. The system was equilibrated at the temperature T for the next 50,000 time steps which is equivalent to 40 ps.

Step 3 (S_3): Iron and diamond were cooled down to 300 K from their respective temperature T, while keeping in contact and equilibrated for the next 50,000 time steps. Cooling was done to investigate, once diffusion starts at elevated temperatures, if carbon atoms

70
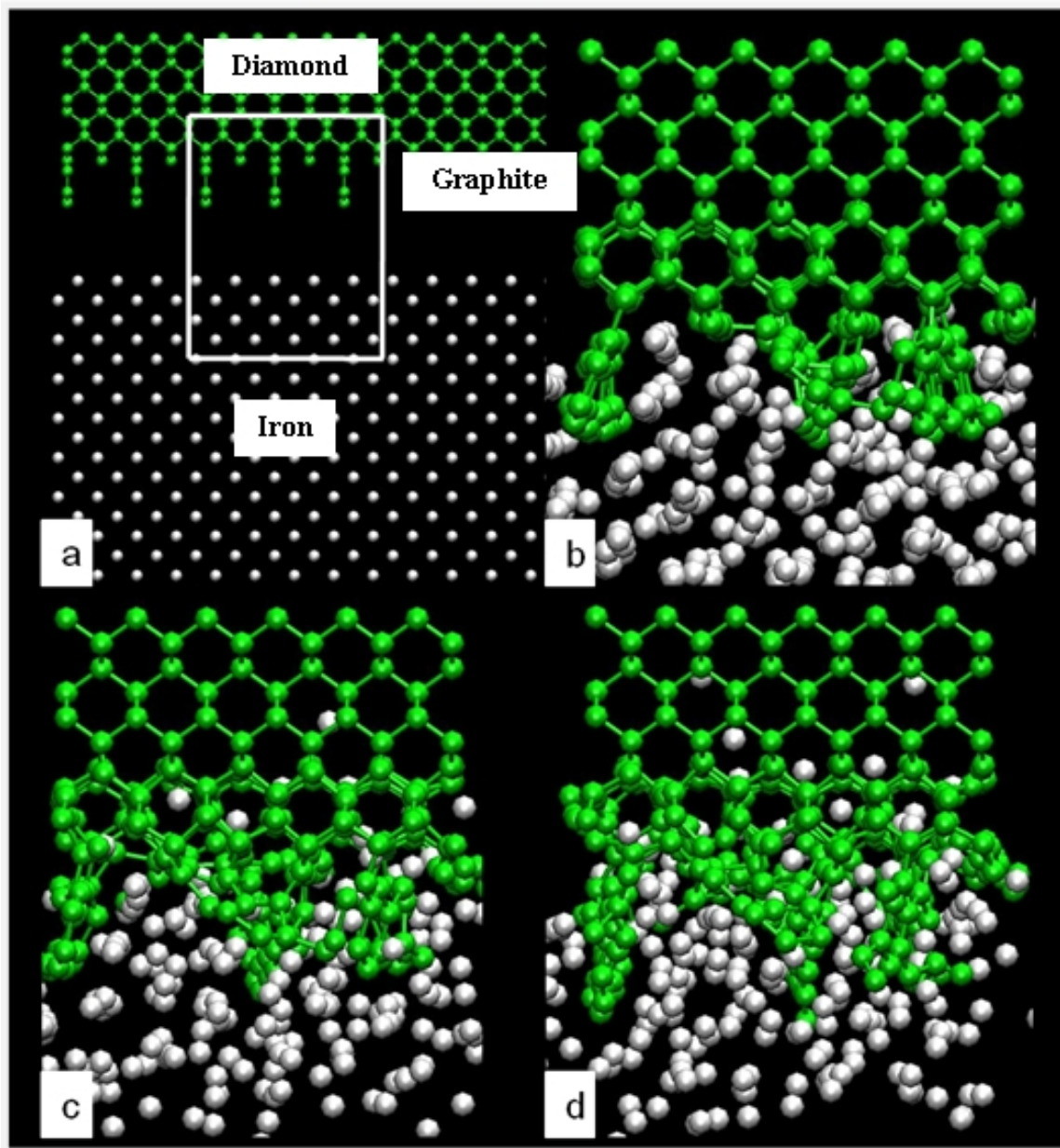
Figure 4.3: Diffusion of carbon atoms into iron at 1600 K after, (a) initial setup, (b) 5 ps, (c) 20 ps, and (d) 40 ps (Region of analysis is shown as a white box in (a)

continue to diffuse into iron, i.e. whether diffusion is strictly a function of temperature.

The MD simulations require the solution of 6 N (where N is the total number of atoms) coupled first-order differential equations of motion. The solution is obtained us-

ing a predictor-corrector algorithm with a fixed integration step size of 0.8 fs.

4.3 Results and discussion

The diffusion couple tests were conducted for three different temperatures: 300 K (T1), 800 K (T2), and 1600 K (T3). There were 4500 iron atoms in the workpiece, 3152 carbon atoms in the diamond-graphite interface tool and 3672 carbon atoms in the diamond tool.

4.3.1 Diamond-graphite interface and iron

As is well known, diffusion rates change with temperatures in accordance with the Arrhenius law. Figure 4.3 shows diffusion of carbon atoms into iron at 1600 K at different times. It can be seen that the carbon atoms from the graphite structure react with the iron atoms and gradually diffuse into the iron. Figure 4.3 (b) shows the initial contact between graphite and iron, where iron atoms have just began to interact with the carbon atoms. Subsequently, more and more carbon atoms react with and diffuse into iron [Figures 4.3 (c) and (d)]. This indicate that graphite reacts with iron at high temperatures. To further analyze diffusion of carbon atoms into iron, we calculated, (a) the radial distribution function (RDF), (b) Fast Fourier transform (FFT), and (c) diffusion depths. These results are presented in the following section.

4.3.1.1 Radial distribution analysis

Figure 4.4 shows the C-C radial distribution function (RDF) after 80 ps at 300 K, 800 K, and 1600 K. No significant change in the distribution of C-C bond distance after 80 ps at 300 K was observed. The C-C equilibrium distance is 1.54 Å for diamond and 1.41 Å for graphite. As can be seen from Figure 4.4, the carbon atoms maintain their crystal structure and do not react with iron but merely vibrate at an equilibrium distance between 1.45 and

1.65 Å. The RDF of C-C bond lengths at 800 K and 1600 K suggest that more and more atoms are vibrating at elongated bond distances.
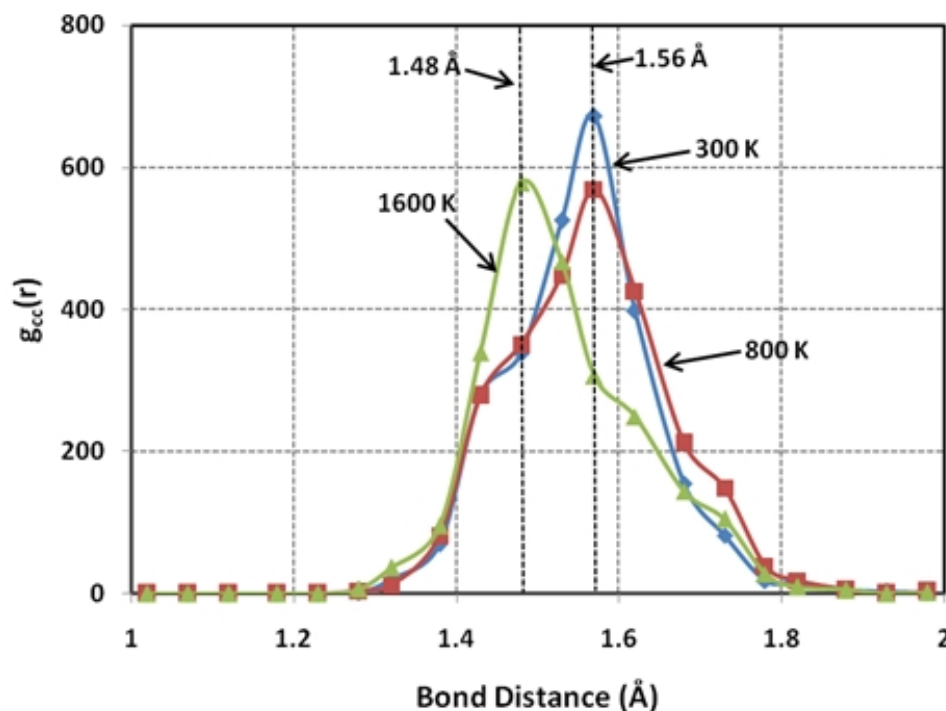
Figure 4.4: Radial Distribution Function (RDF) of carbon atoms at the junction of iron and diamond-graphite interface

At 800 K, some atoms are beyond 2 Å as the integrated area of the distribution is different from that at 300 K. This indicates that some atoms may have begun to react with iron and, thus, are losing their crystallographic graphite structure. This phenomenon is accentuated at 1600 K, where the RDF maximum shifts to 1.48 Å, a distance much closer to that of equilibrium graphite. This is a plausible indication of diffusion. One could also attribute this to the elevated temperatures in the system. Nevertheless, the fact remains that the C-C system is not vibrating freely but is in firm contact with the iron. Carbon atoms do not have any free space to vibrate and, hence, they diffuse into the iron.

4.3.1.2   Fast fourier transform (FFT) analysis

The results shown in Figures 4.5 and 4.6 are Fast Fourier Transforms (FFTs) of the temporal behavior of bond lengths and bond angles in the interface zone between carbon and iron as predicted by the MD simulations. Such transforms exhibit maxima at frequencies corresponding closely to the fundamental vibrational frequencies and their overtones of the model system for the force field employed in the calculations. In this respect, the FFT provides information similar to that obtained from IR and Raman spectra. However, the magnitude of the FFT maxima will not correspond to the measured intensities of IR and Raman bands, which depend upon concentrations, instrument characteristics, quantum mechanical transition probabilities, and oscillator strengths, none of which are present in the MD calculations.
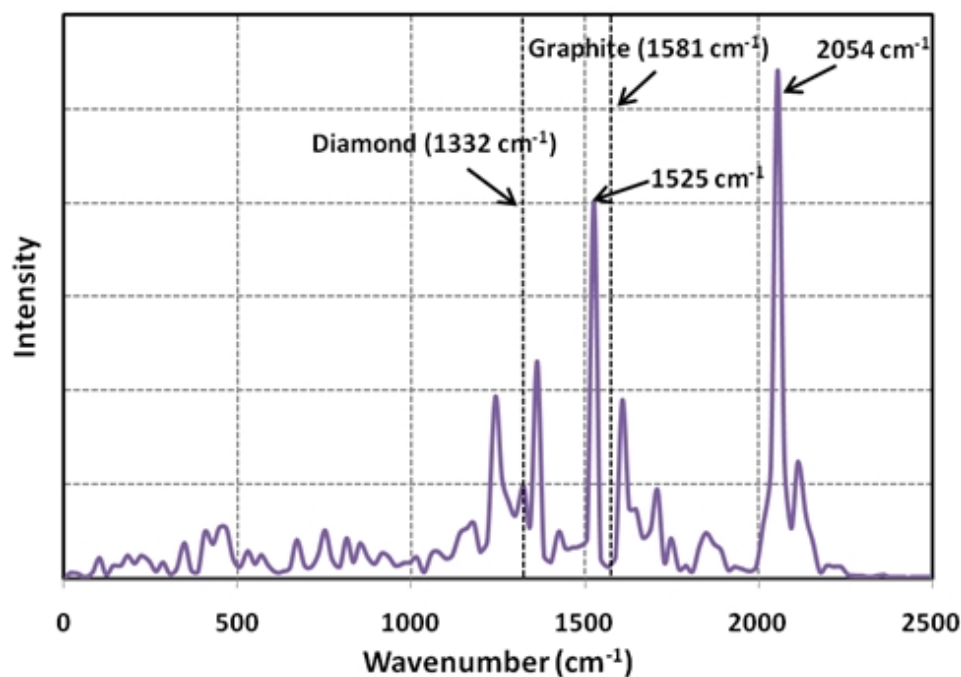
Figure 4.5: FFTs of diamond-graphite interface without the presence of iron at 1600 K

Figure 4.5 shows FFTs of the diamond-graphite interface at 1600 K after 80 ps. The
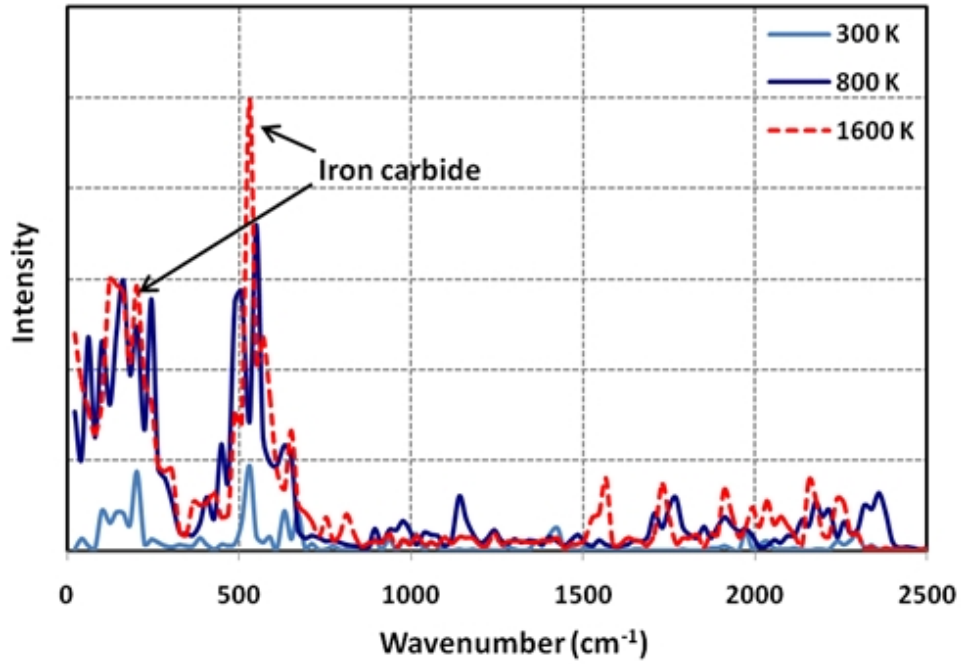
Figure 4.6: FFTs of atoms at the junction of iron and diamond-graphite interface at different temperatures

peak for graphite is found experimentally to be 1581 cm^{-1} [32]. Here, we observed peaks at 1525 and 2054 cm^{-1}, which correspond to graphitic bonding as well as bonding between the diamond-graphite interface. The figure also shows the range of C-C bond frequencies present at the diamond-graphite interface (i.e. with no iron present), when the REBO Brenner potential is employed.

For the diffusion test, a region (42 x 4 x 42 Å) at the contact junction of iron-carbon was considered. After 80 ps time steps, a neighbors' list was generated for all the carbon atoms lying in this region. This list was observed for 1.6 ps. Coordinates of the atoms were recorded after every 1.6 fs. The FFT for bonds that did not persist for 1.6 ps were not included. The FFT of the temporal variation of each bond was normalized and then all normalized FFTs were summed up for all the neighbours. We calculated the resultant composite FFTs at 300 K, 800 K, and 1600 K for different times and plotted as shown in

Figure 4.6.

At 300 K, we observe increased modes of vibrations but the dominant frequencies are that of C-C. These increased modes may be due to initial mechanical deformation of graphite atoms and/or compression experienced by the carbon atoms as they are in firm contact with iron. Note that the potential representing the Fe-C interaction is not sufficiently robust to accurately represent iron carbide (Fe_3C). We can, however, use the FFT spectra to determine whether C-C bonds break and carbon atoms diffuse into iron. If iron carbide (Fe_nC_m) systems are dominant, we would expect to observe a shift in the bond frequencies. In other words, the composite FFT spectra would be expected to exhibit Fe-C frequencies, which should appear at lower wave numbers.

Experimentally, iron carbide frequencies lie in the 200 - 600 cm^{-1} range [164]. We observed these shifts in the frequencies in the simulation at all temperatures, albeit at lower rates at lower temperatures. Figure 4.6 shows composite FFT spectra for atoms at the diamond-graphite interface and iron junction at 300 K, 800 K, and 1600 K. At elevated temperatures of 800 K and 1600 K, the appearance of Fe-C bond frequencies around 200 cm^{-1} and 500 cm^{-1} can be clearly seen.

4.3.1.3 Diffusion analysis

Figure 4.7 (a) shows the spatial distribution of the carbon atoms diffusing into iron, quantitatively, at 1600 K as a function of depth into iron for different time intervals. Note that diffusion occurs when the system is at 1600 K for 40 ps but not when the system is cooled down to 300 K for another 40 ps. As expected, the diffusion rate is a function of temperature. Similar behaviour is observed at 800 K [Figure 4.8 (a)], but the amount of carbon diffused into iron is less than that observed at 1600 K. There is no significant amount of diffusion observed at 300 K [Figure 4.7 (a)].
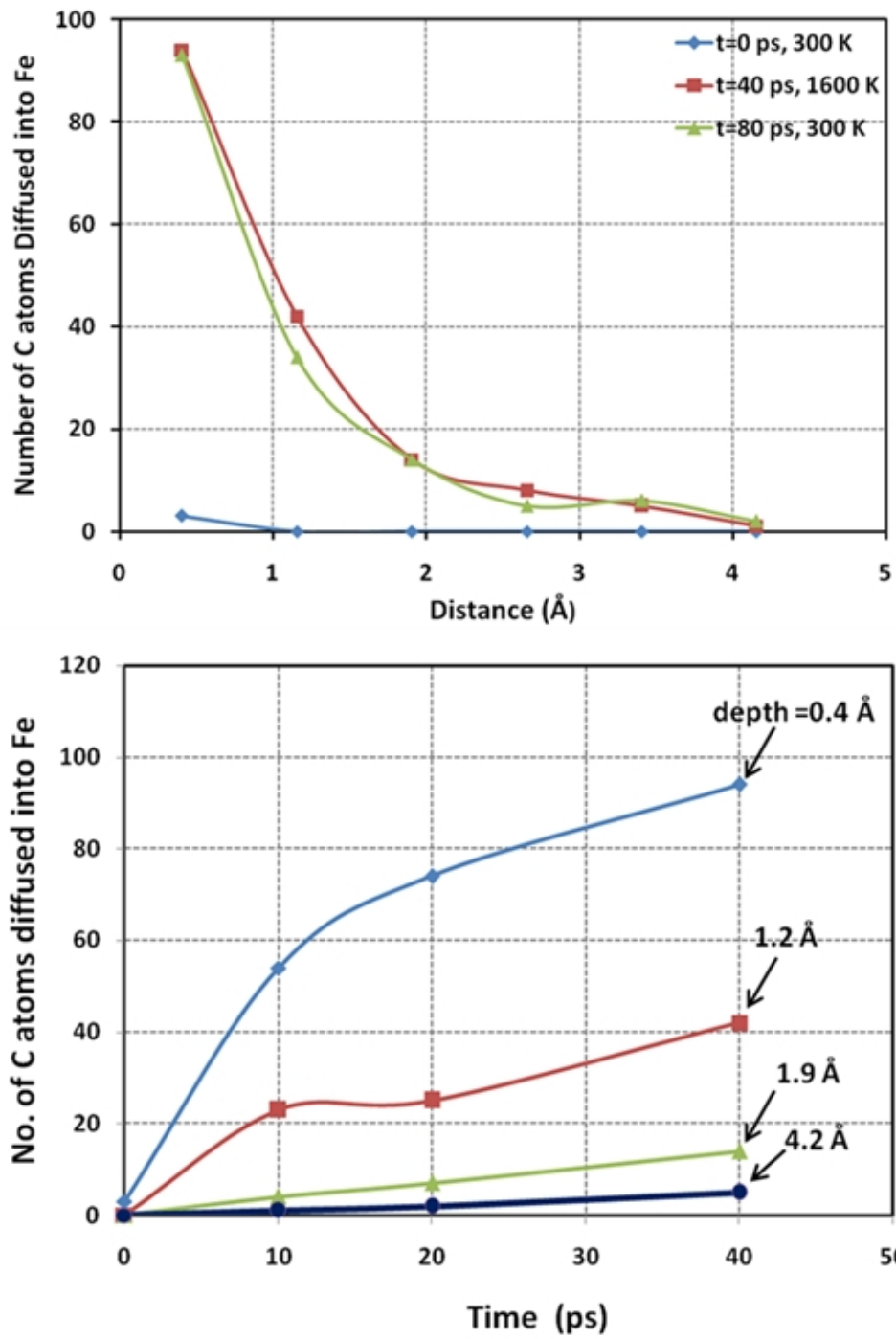
Figure 4.7: Diffusion of carbon atoms into iron at 1600 K, (a) along the depth and (b) at different times

The numbers of diffused carbon atoms with respect to time for different depths at temperatures of 1600 K, 800 K, and 300K are shown in Figures 4.7 (b), 4.8 (b), and 4.9 (b), respectively. As steady-state conditions are approached, the number of diffused carbon atoms asymptotically reaches a certain value for a particular depth and temperature. The number of diffused carbon atoms depends on the temperature; as the temperature decreases, the number of carbon atoms at a particular depth also decreases. As can be expected, the number of diffused carbon atoms increases with increasing temperature.

Figure 4.10 compares the experimental values [165] of solubility of carbon in iron with the current MD simulation results. The calculated variation of solubility with temperature is in good agreement with the experimental trend, but experimental solubility is about twice the MD result after 80 ps. This discrepancy can be attributed to the approximate nature of the potential-energy surface used, combined with the limited simulation time, which is insufficient to reach steady-state conditions.

4.3.2 Diamond and iron (no graphite interface)

Diamond (in the absence of a graphite interface) and iron were considered for the diffusion couple tests. Only the first three layers from the bottom of the diamond were made moveable, while the rest of the carbon atoms were fixed. The orientation of the diamond chosen was (001) [110]. This configuration is identical to the diamond-graphite interface-diamond, but without any graphitic carbon atoms. The simulation conditions are identical to that of diamond-graphite interface.

Figure 4.11 shows the simulation images at different time steps, where it can be clearly seen that carbon atoms in the diamond structure do not react with iron. This is in contrast to the situation when there is a layer of graphite on top of a diamond surface (Figure 4.3 for comparison).
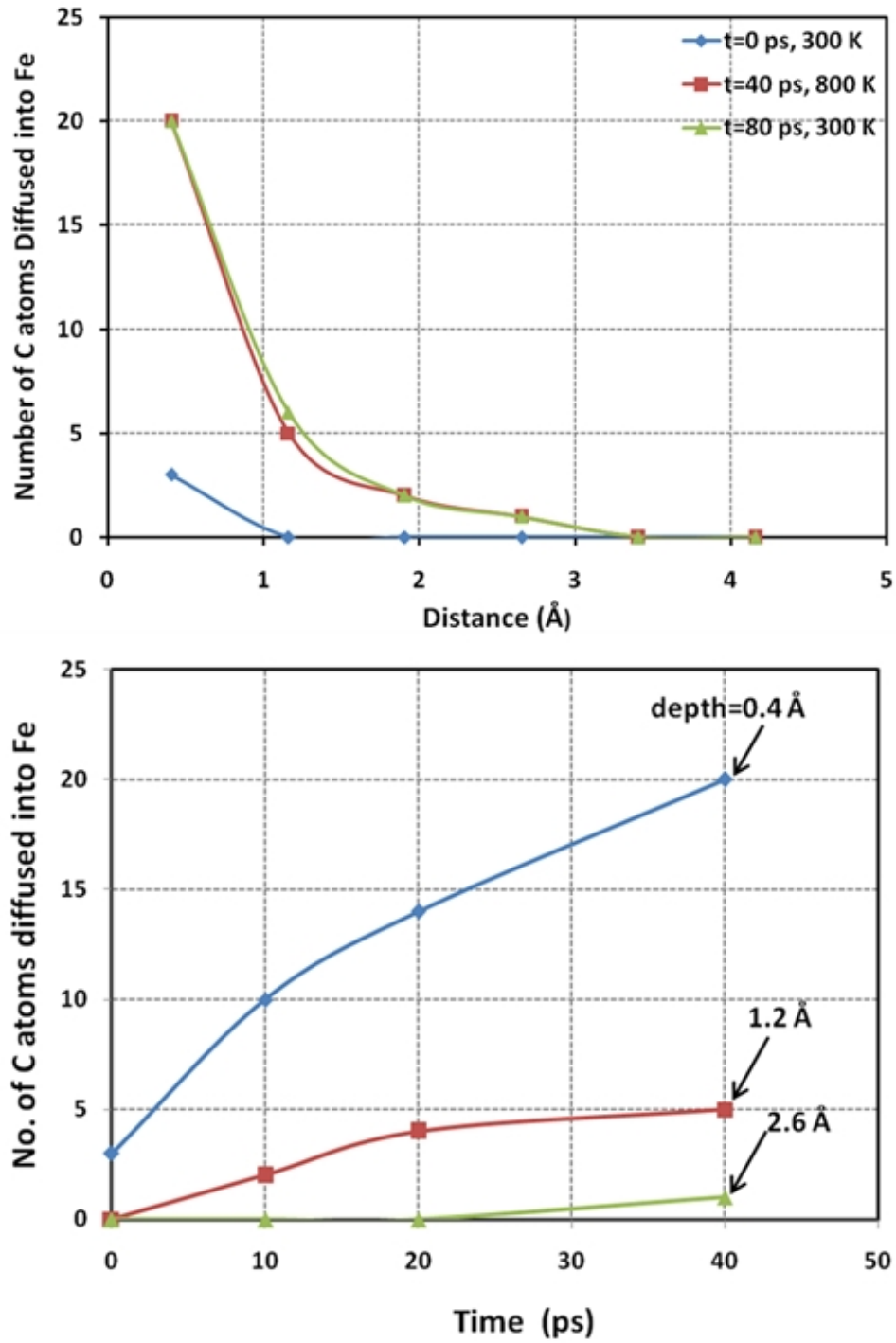
Figure 4.8: Diffusion of carbon atoms into iron at 800 K, (a) along the depth and (b) at different times
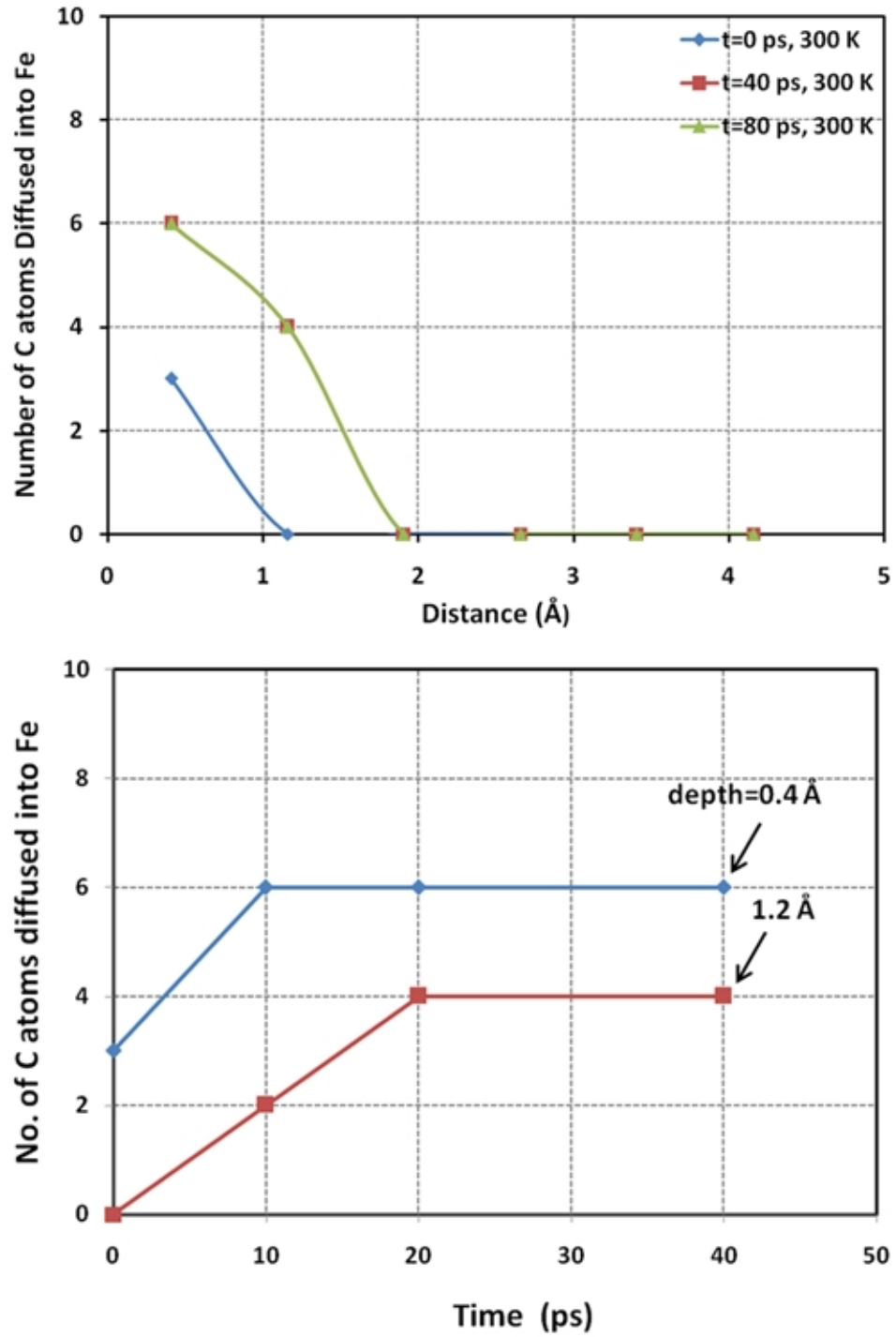
Figure 4.9: Diffusion of carbon atoms into iron at 300 K, (a) along the depth and (b) at different times
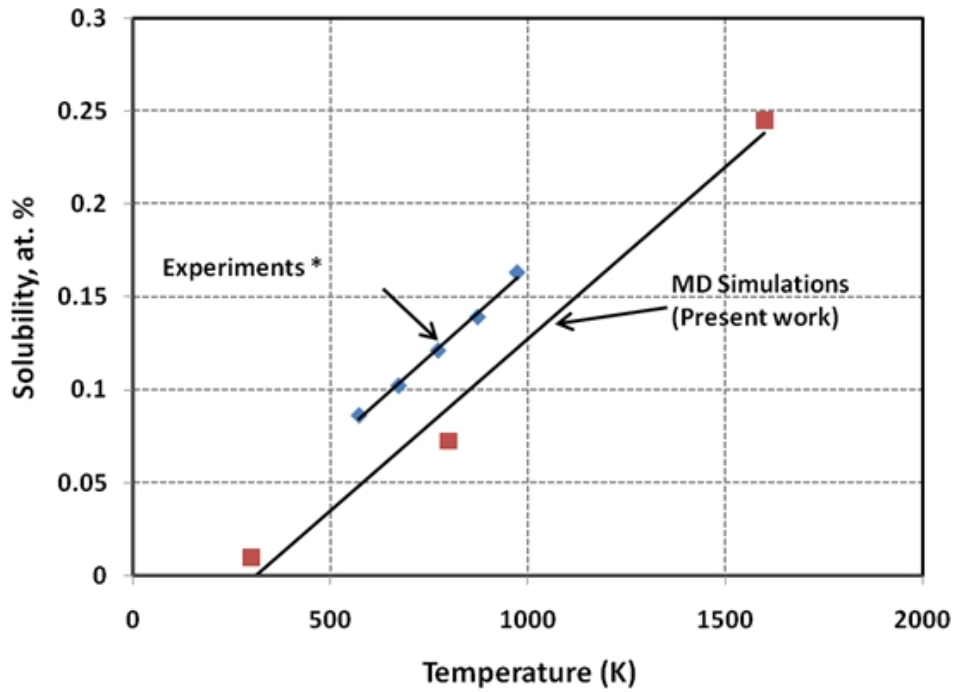
Figure 4.10: Comparison of the solubility of diffused carbon atoms in iron with the experimental results [165]

4.3.2.1 Radial distribution analysis

Figure 4.12 shows the RDF of the carbon atoms at the junction of diamond and iron at temperatures of 300 K, 800 K, and 1600 K. At different temperatures, the RDF distribution remains peaked at 1.54 Å, which is the C-C equilibrium distance in diamond. It can be clearly seen from Figure 4.11 that diamond does not lose its crystallographic structure. This is again in contrast to the situation of a layer of graphite on a diamond surface (see Figure 4.4 for comparison).

4.3.2.2 Fast fourier transform (FFT) analysis

Figure 4.13 shows the FFTs of the temporal variation in the bond distances of the atoms at the contact region of diamond and iron at 300 K, 800 K, and 1600 K. The atoms consid-
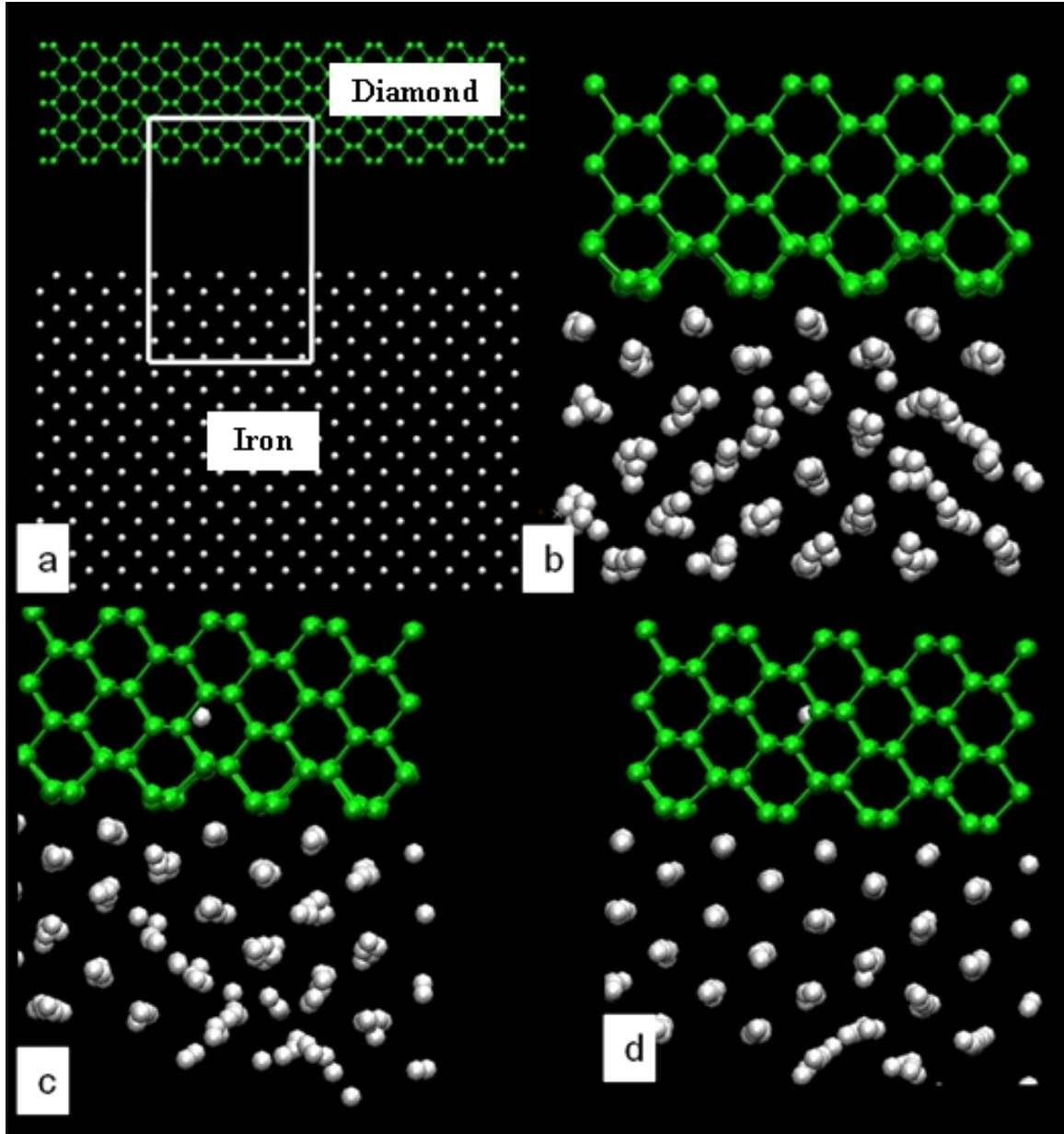
Figure 4.11: Simulation snapshots after (a) Initial setup, (b) 5 ps, (c) 20 ps, and (d) 40 ps, No diffusion of carbon was observed when diamond and iron were used, (Region of analysis is shown by the white box in (a)

ered for FFT are only a few layers from the surface at the junction of iron and diamond. We observed the dominant frequency to be that of diamond. Diamond shows a peak at 1332 cm^{-1} [166].
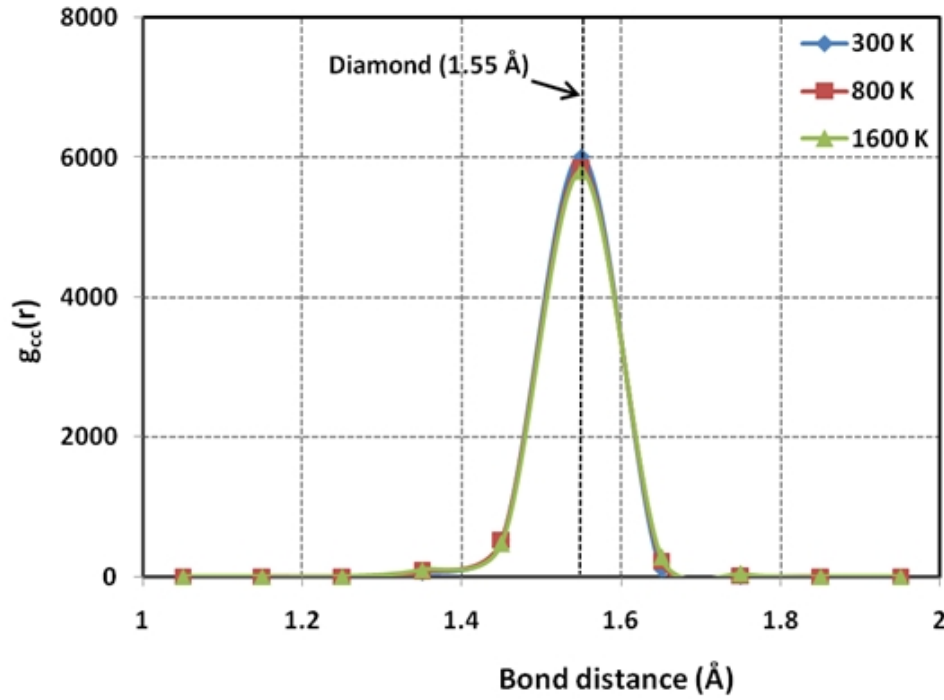
Figure 4.12: Radial Distribution Function (RDF) of carbon atoms at the junction of iron and diamond

The FFTs show a slight shift towards the right with a peak at 1372 cm^{-1}, indicating that the surface layers of diamond atoms are experiencing internal stresses (residual stresses) [167]. No shift towards lower frequencies was observed. We would have expected this shift had iron carbide been formed, as we have observed in the case of the diamond-graphite interface. This shows that no diffusion takes place between iron and carbon when diamond was used without a graphite interface layer.

Experimental diffusion couple tests have been performed previously by Tanaka and Ikawa [10] and Loladze and Bokuchava [168] under equilibrium conditions by heating the system for a very long time compared to the contact time between a cutting tool/abrasive and the workmaterial in machining/grinding. The timescale in MD simulations is extremely small, on the order of 10^{-9} s, compared to the experimental diffusion test results. However, MD may represent a small fraction of the actual experimental contact time in grinding. The
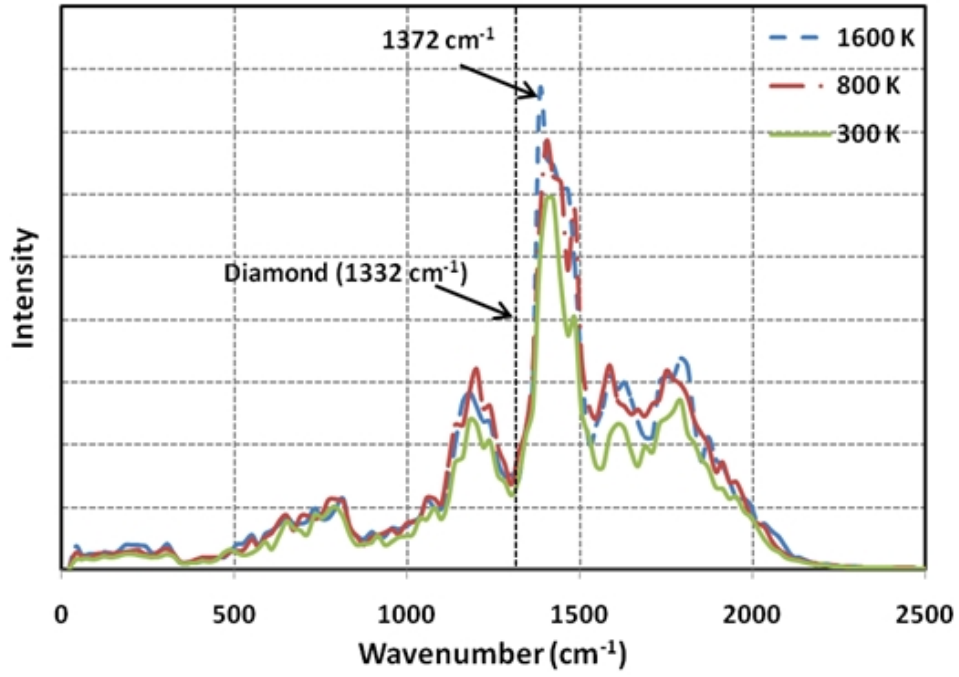
Figure 4.13: FFTs of atoms at the junction of iron and diamond

Table 4.1: Comparison between experimental and MD simulation (present work) results

	Ikawa and Tanaka [10]	Loladze and Bokuchava [168]	Komanduri and Shaw [9]	Present work
Time (ps)	1800×10^{12}	5×10^{11}	2×10^6	40
Temperature (K)	1300	1600	-	1600
Diffusion layer (Å)	2×10^6	80×10^4	160	4.2
Diffusion layer (Theory) (Å)	2.22×10^6	94.3×10^4	105	8.43

grinding test [8] has a contact period of 2×10^{-6} s, which is 10^4 times more than the MD time, but is the closest of all the experimental results comparable with MD simulations. Table 4.1 summarizes the results. Note that the diffusion layer observed in MD simulations

is two orders of magnitude smaller than in the grinding operation.

4.4   Conclusions

Diffusion of carbon into iron was observed only when a diamond-graphite interlayer was added to diamond but not when diamond was used alone. This result provides corroborating evidence supporting the experimental results [8–10, 13, 15, 16] observed previously that diamond initially graphitizes and subsequently diffuses into iron resulting in rapid diamond tool wear.

As can be expected, diffusion of the carbon atoms into iron was observed at higher temperatures (800 K and 1600 K) but no noticeable diffusion was observed at the lower temperature (300 K).

Table 4.2: Diffusion depth of carbon into iron, calculated form MD results, after 40 ps

Temperature (K)	300	800	1600
Diffusion layer (Å)	0-1	2.6	4.2

Diffusion depth increases with increasing temperature (see Table 4.2). Concentration of carbon atoms in iron increases with increasing temperature. At a particular temperature, the concentration of carbon atoms diffused into iron would reach a saturation value with respect to time as steady-state conditions are reached.

CHAPTER 5

WEAR OF DIAMOND IN THE MACHINING OF IRON

5.1 Introduction

It has been shown (Chapter 4) that graphite dissolves in iron in the graphite stable region and precipitates out as diamond in the diamond stable region. Thus carbon in the form of diamond does not react with iron but graphite does. This corrborates with the results reported by the experimentalists [9, 10]. Komanduri and Shaw [8, 9] postulated that diamond at room temperature is in a metastable state (sp^3 bonding) and will transform into graphite (sp^2 bonding) under the appropriate conditions of pressure and temperature. An increase in temperature in cutting/grinding of ferrous materials without a concomitant increase in pressure (relative to diamond-graphite equilibrium) can promote graphitization [11]. This can be accelerated under the influence of properly directed shear stress [12]. The presence of a catalyst/solvent material, e.g. iron, that rapidly converts to graphite from the surface of diamond at high temperature can aid in this transformation [13].

It may be noted that iron is used as a catalyst/solvent in the synthesis of diamond under high pressure-high temperature conditions [14]. It can play a similar role in reverse, namely, the transformation of diamond into graphite in the graphite stable region. During machining, the freshly generated surface under the clearance face or at the tool-chip interface can further assist the graphitization process [15]. All of the above mentioned con-

ditions, namely, high temperatures, pressures below the diamond stable region, presence of hot iron, and newly generated nascent surface exist at the tool-workpiece interface. In this chapter, we investigate the micromechanisms underlying the wear of diamond in the machining of iron using molecular dynamics (MD) simulations[†].

5.2   Simulation setup and test conditions

In machining, almost all of the plastic deformation energy is converted into heat. It has been shown experimentally that of the total heat energy generated in machining, some 80% is carried away by the chip, and 10% each is dissipated into the workpiece and the tool. In MD simulations of nanometric cutting, peripheral atoms are used to incorporate bulk temperature effects so that the heat generated is continuously dissipated away from the cutting region. This is necessary because the size of the system used in an MD simulation of machining is rather small compared to the microscopic model and the use of a very large model is restricted by prohibitive computational time.

MD simulations have been used successfully to model various aspects of nanometric cutting and tribology [169] since the pioneering work of Belak and Stowers [58] on cutting and Hoover *et al.* [170] on indentation at the Lawrence Livermore National Laboratory (LLNL). Factors considered include the effect of cutting parameters [69], tool geometry [70, 71], tool wear [68, 82], effect of crystal orientation and direction of cutting [72], material removal mechanisms in the machining of different work materials, such as copper, aluminum, and silicon [75], indentation and scratching [171], atomic-scale friction [172].

The machining model used in this investigation is a slightly modified form of the model reported earlier [76, 169] in that the moving and the peripheral atoms are incorporated in the workpiece as well as in the tool in the present case and only in the workpiece in the

87
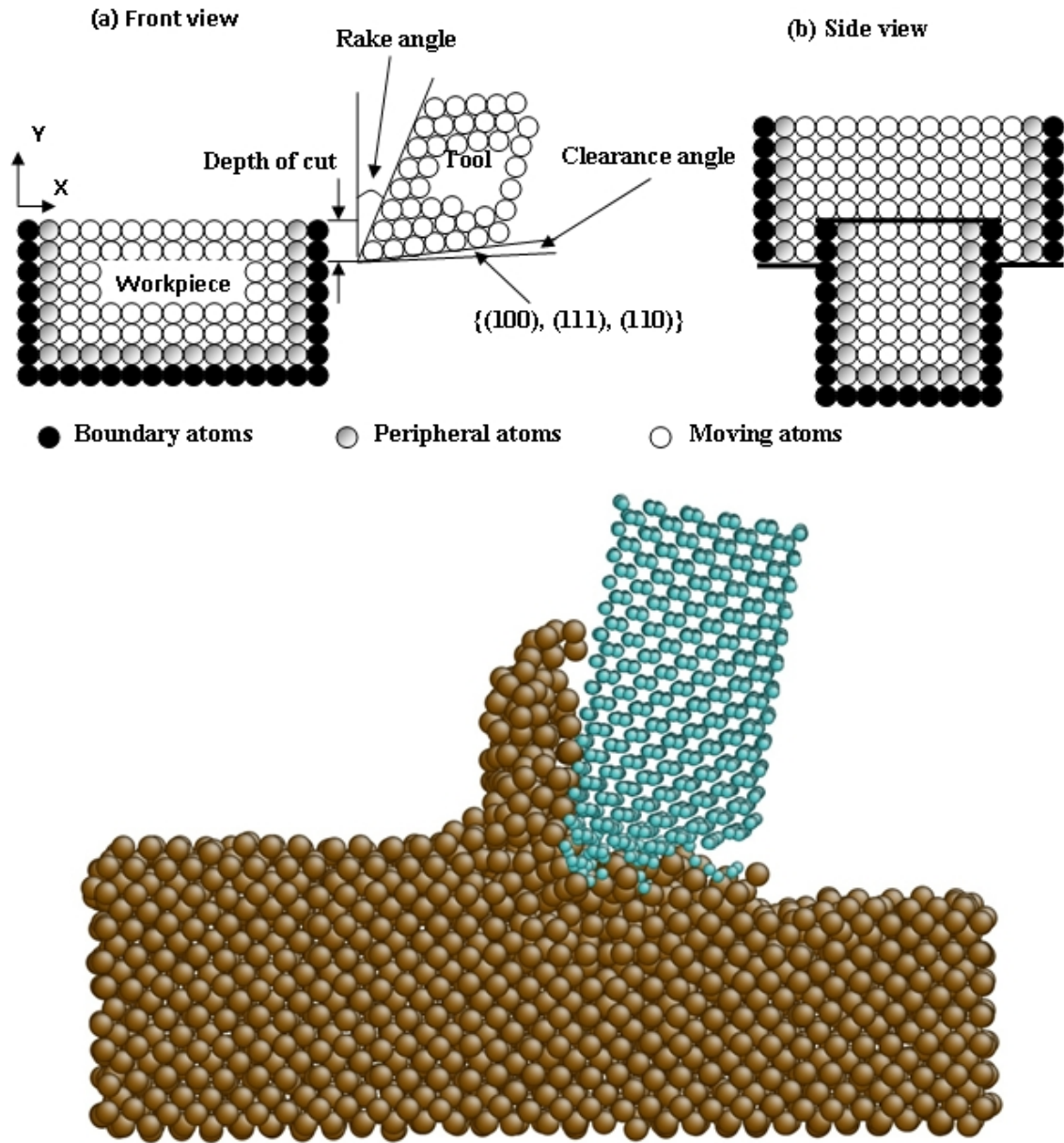
Figure 5.1: (a) Schematic of MD simulation of orthogonal (or 2D) machining with a deformable tool, (b) snapshot of MD simulation of orthogonal machining of iron with a diamond tool

previous model. This was done to dissipate heat from the tool during machining. Figure 5.1 (a) is a schematic of the MD simulation of orthogonal (2D) machining operation showing the distribution of moving, peripheral, and boundary atoms in the tool and the workpiece. Table 5.1 gives details of the iron workpiece, the diamond tool, and the cutting conditions used.

Table 5.1: MD simulation parameters and cutting conditions for nanometric cutting

Workpiece dimensions	86.1 Å x 28.7 Åx 17.22 Å
Workpiece material	Iron
Workpiece machining surface	(010)
Cutting direction	<100>
Tool orientation	(a) (100, 010)
	(b) (11$\bar{2}$, 111)
	(c) (100, 011)
Tool material	Diamond
Rake and clearance angles	10° and 5°
Initial temperature	300 K
Cutting velocity	100 m s^{-1}
Total simulation time	50 ps (50,000 time steps with a step size of 0.1 fs)

The iron workpiece is oriented along (100) machining surface and cutting was performed in the <100> direction of the workpiece. Each tool is shaped with a 10° rake angle and a 5° clearance angle. Machining was conducted at a cutting speed of 100 m s^{-1} to reduce the computational time to a reasonable value.
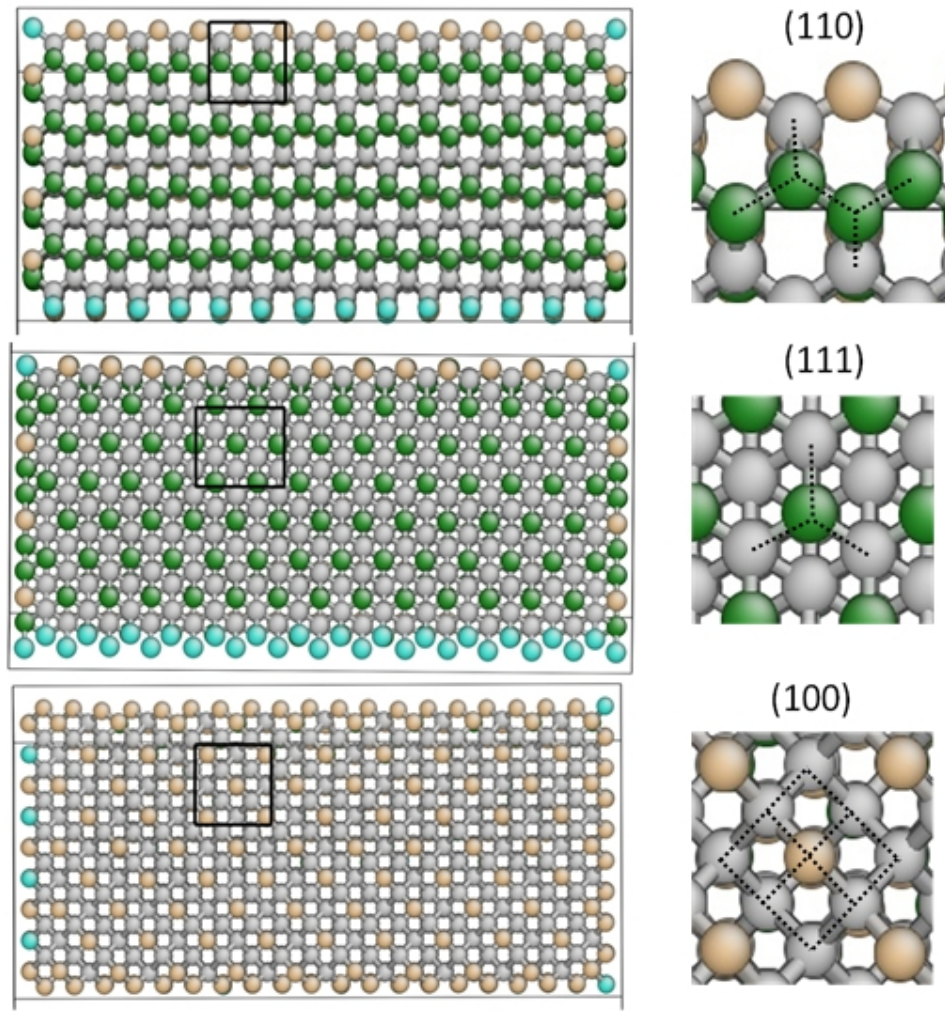
Figure 5.2: Projected view of the (110), (111), and (100) clearance planes of diamond tool in this investigation

Figure 5.1 (b) shows a snapshot of MD simulation of orthogonal cutting (2D) of pure iron with a deformable diamond tool. Three different orientations of the clearance faces, namely, (i) (110), (ii) (111), and (iii) (100) for the diamond tools were considered. The crystallographic orientation of diamond was such that the plane considered coincided with the clearance face. Figure 5.2 shows the projected views of the (111), (110), and (100) clearance faces of the diamond tool used in this investigation showing the crystallographic arrangements of the diamond atoms in each orientation. The total simulation time was 50

ps (500,000 time steps with a step size of 0.1 fs), which corresponds to 50 Å of length of cut. This small step size was chosen to ensure proper MD response to the MEAM potential.

MD simulations of nanometric cutting of iron with a diamond tool require potentials for Fe-Fe, C-C, and Fe-C interactions to model it appropriately. A modified embedded-atom method (MEAM) potential, developed by Baskes and co-workers [45, 52, 53], was used to represent the Fe-Fe and the Fe-C bonds. This potential was shown to represent various physical properties of iron reasonably well [53]. Lee [55] developed MEAM potential parameters for Fe_3C binary systems which reproduce several physical properties of the iron carbide.

In this investigation, MEAM potential was also chosen for Fe-Fe and Fe-C interactions. Currently, with the MEAM potential formalism, only diamond, and not graphite, can be simulated [54]. Hence, there was a need to choose a potential that can represent both diamond and graphite to observe the transformation. The Tersoff potential [39] can represent both diamond and graphite structures as well as their transformation from diamond to graphite [115] and vice versa [110]. This potential, therefore, was chosen for C-C interactions.

Tables 2.1, 2.2, and 2.3 (refer to Chapter 2) give Tersoff potential parameters for carbon-carbon and MEAM potential parameters for iron-iron and iron-carbon, respectively. Large-scale Atomic/Molecular Massively Parallel Simulator (LAMMPS) software [57] developed at the Sandia National Laboratories (http://lammps.sandia.gov) was used for the simulations with these potentials. All atoms, except the boundary atoms, were initialized with velocities corresponding to a room temperature of 300 K. The temperature of the peripheral atoms was maintained at this temperature. At each time step, the temperature of the peripheral atoms was reset using the rescale command in the LAMMPS software for rescaling the velocities [57].

5.3   Results

In the following, wear by graphitization of diamond cutting tool on various clearance face orientations, namely, (110), (110), and (100) in the machining of iron is presented (Figure 5.2).

5.3.1   Case i: Clearance face (110)
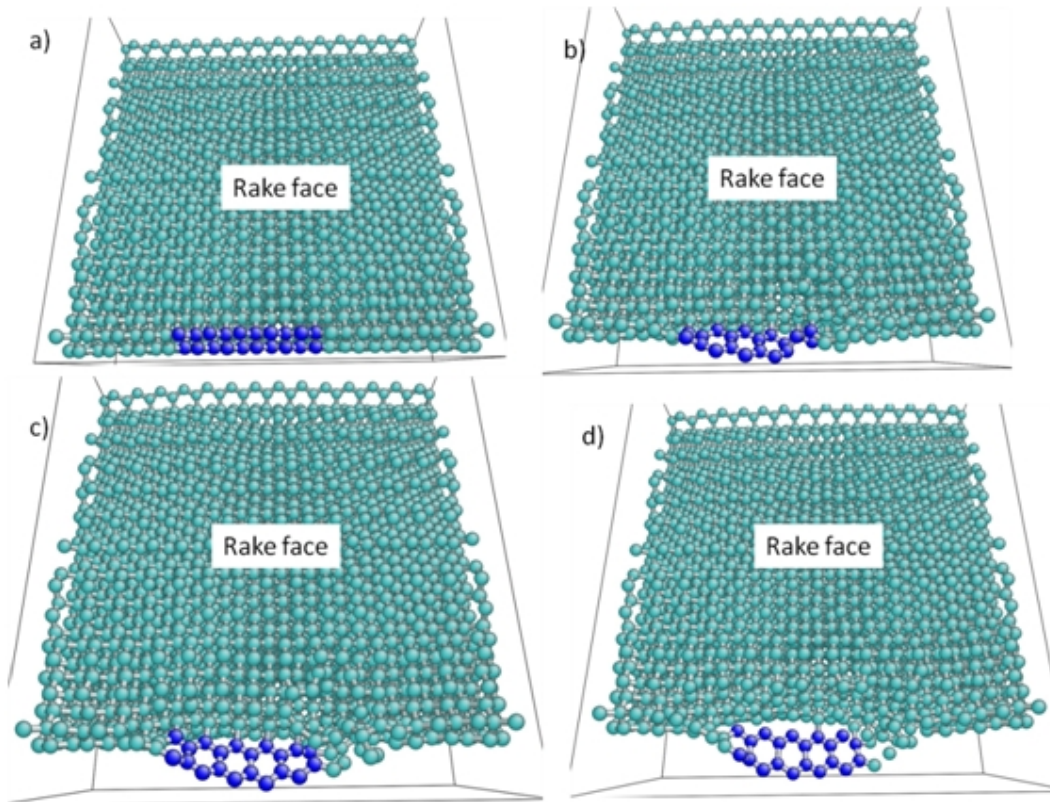
Figure 5.3: MD simulation snapshots at various steps showing graphitization of diamond tool in the machining of iron when the clearance plane coincides with (110) plane

Figures 5.3 (a) to (d) are MD snapshots of the (110) clearance face at various stages of cutting showing progress of graphitization at the tool tip on the clearance face of the

diamond tool as machining progresses. Some atoms at the cutting edge are marked violet to follow the progress of graphitization. It can be seen that graphitization originates, in this case, at the middle of the cutting edge and propagates parallel to the cutting edge on either side. It will be shown that this is very different from the ones observed for cases (ii) and (iii).
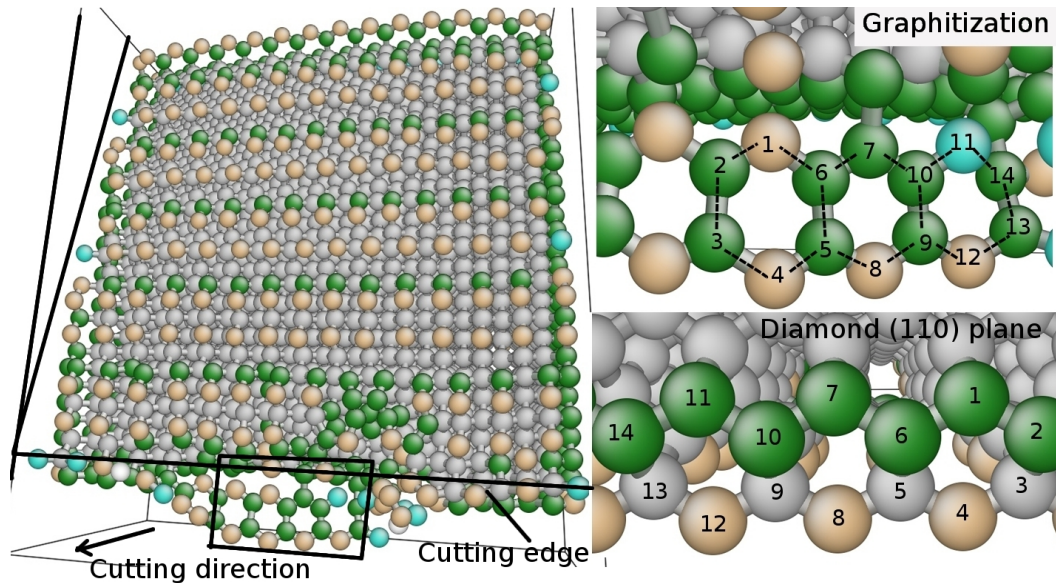
Figure 5.4: (a) Graphitization of diamond in the machining of iron along (110) plane, (b) zoomed-in region of the graphitized diamond, (c) tagged carbon atoms in (b) are backtracked to the initial configuration on the clearance face showing the (110) plane

Figure 5.4 (a) shows the (110) clearance face of the diamond tool after graphitization at the tool cutting edge. Figures 5.4 (b) and (c) show close-up views of diamond and graphite atoms, before and after graphitization, respectively. Atoms are color coded according to their coordination number and are so identified in the figure caption. Coordination numbers are with respect to the other carbon atoms, bulk-4 (Grey), surface-3 (Green), surface-2 (Burlywood), edge-1 (Turqoise), seperated-0 (White).

To identify the transformation from diamond to graphite, atoms that formed graphite after machining were backtracked to the initial configuration (diamond). The plane of graphitization is contained within the clearance face [Figure 5.4 (c)]. This indicates that (110) is the plane of graphitization and it propagates preferentially in the $<01\bar{1}>$ direction over $<100>$.

Figure 5.4 (b) shows graphitized (110) plane of diamond. Figure 5.4 (c) shows the (110) diamond plane. It can be seen that atoms from the cutting edge (tag numbers 4, 8, and 12) along with atoms from the surface (tag numbers 1, 2, 6, 7, 10, 11, and 14) and the bulk (tag numbers 3, 5, 9, and 13) come together to form basal plane of graphite. It was observed that graphite ultimately breaks down because of the shear stress acting along the cutting edge and subsequently react with the iron underneath the clearance face of the tool to form iron carbide, similar to cases (ii) and (iii).

5.3.2   Case ii: Clearance face (111)

Figure 5.5 (a) shows the (111) clearance plane of the diamond tool face. Figures 5.5 (b) and (c) show close-up views of diamond and graphite atoms before and after graphitization, respectively. Atoms are again color coded according to their coordination number and are so identified in the figure caption. Atoms that formed graphite after machining were again, back tracked to the initial configuration (diamond) to identify the transformation from diamond to graphite.

It was found for this case that graphitization propagates perpendicular to the cutting edge. In other words, it propagates in a direction opposite to the cutting velocity but is contained within the clearance face [Figure 5.5 (b)]. This indicates that (111) plane is the graphitization plane and it propagates in $<112>$ direction over $<110>$. Figure 5.5 (c) shows graphitization on (111) plane. We can see that atoms at the cutting edge (tag

numbers 2, 3, and 4) along with atoms from the surface (tag numbers 6, 8, 10, 12, and 14) and the bulk (tag numbers 1, 5, 7, 9, 11 and 13) come together to form graphite. It was observed that graphite eventually breaks down and then reacts with iron atoms underneath the clearance face to form iron carbide.
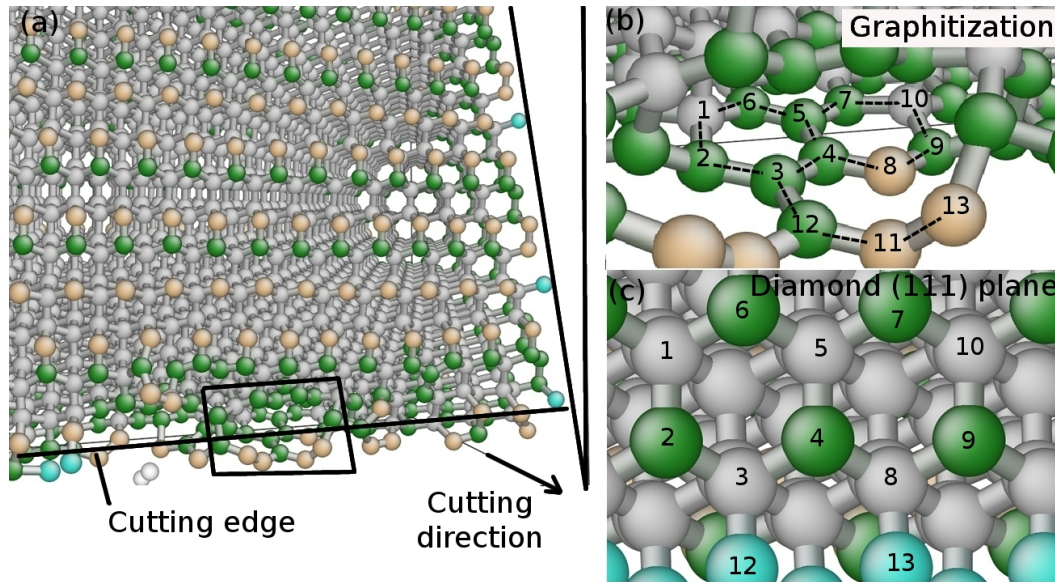
Figure 5.5: (a) Graphitization of diamond in the machining of iron along (111) plane, (b) zoomed-in region of the graphitized diamond, (c) tagged carbon atoms in (b) are backtracked to the initial configuration on the clearance face showing the (111) plane

5.3.3 Case iii: Clearance face (100)

Figure 5.6 (a) shows the (100) clearance plane of the diamond tool and Figures 5.6 (b) and (c) show a close-up view of diamond and graphite atoms before and after graphitization, respectively. Atoms are again color coded according to their coordination number and are so identified in the figure caption. Not much graphitization was observed in this case. This is because (100) plane is not the natural plane for diamond to graphitize; in fact, it is most resistant to graphitization [97]. Here, we observe the wear of diamond to take place along

the rake face. Atoms that formed graphite after machining were again back tracked to the initial configuration (diamond) to identify the transformation from diamond to graphite. It was observed that atoms from the surface (tag numbers 3, 7, 8, 13, and 14) along with bulk (tag numbers 1, 4, 5, 6, 9, 10, 11, 12, 15, and 16) to form the graphitic structure [Figure 5.6 (c)].
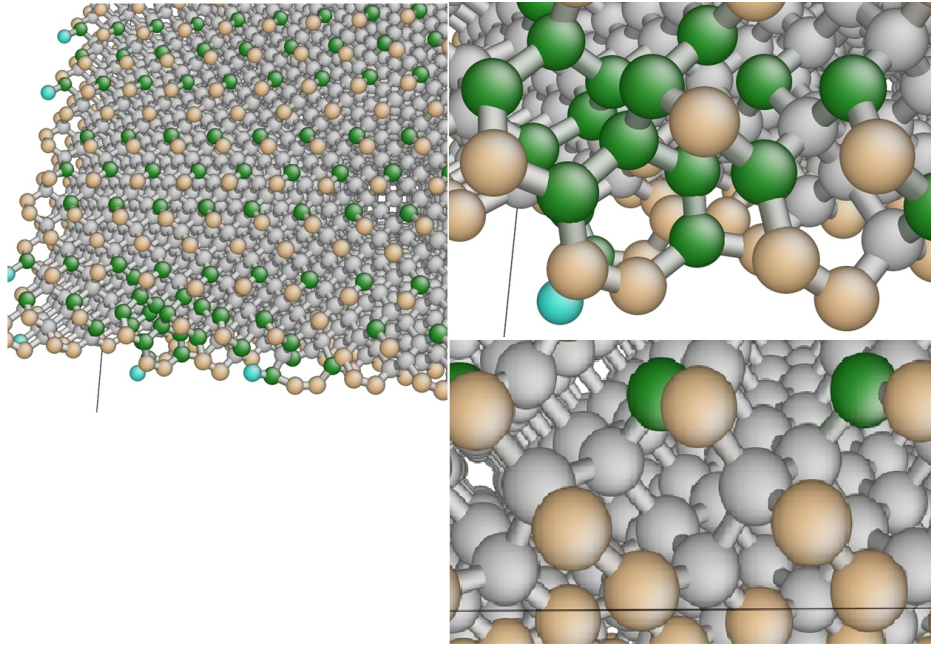
Figure 5.6: (a) Graphitization of diamond in the machining of iron along (100) plane, (b) zoomed-in region of the graphitized diamond, (c) tagged carbon atoms in (b) are backtracked to the initial configuration on the clearance face showing the (100) plane

It can be seen that the plane of graphitization is not the (100) plane. A plane was drawn through the atoms which were tracked in Figure 5.6 (b). We found the approximate plane of graphitization to be (1, 0.83, 0) which is close to (110) [Figure 5.6(d)]. This plane is in the rake face and oblique to the cutting edge of the tool. It was observed that graphite quickly disintegrates and then starts reacting with the iron underneath the clearance face.

The separated carbon atoms from the graphitized diamond tool subsequently diffuse into the iron workpiece thus paving the way to form iron carbide. As machining continues, we observed that in all the three case, diamond tool was found to graphitize under the conditions of high temperature and freshly generated machined surface similar to that found in the experiments [8–10, 15]. Because of the intimate contact under pressure, separated carbon atoms from the graphitized diamond tool subsequently diffuses into the iron workpiece to form iron carbide [Figure 5.7].
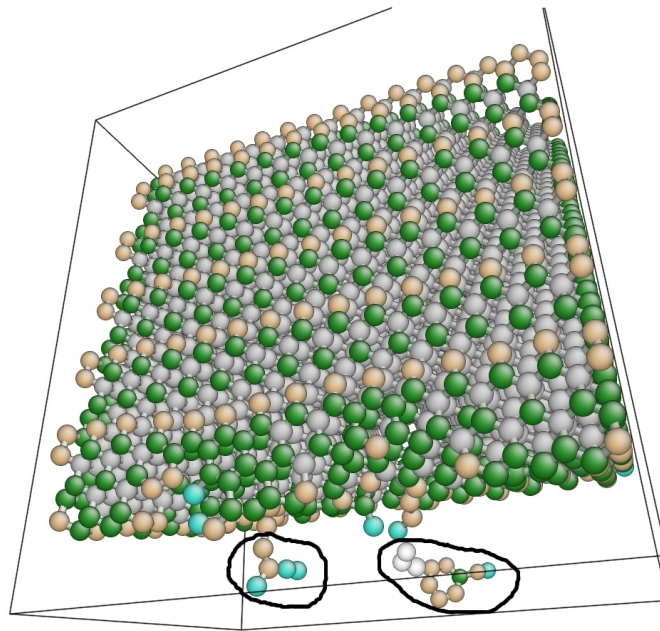
Figure 5.7: Dissolution of graphite in iron during simulated machining (highlighted by circles)

5.4   Discussion

The mechanism observed here using MD simulations was found to be very similar to the one proposed earlier by Komanduri and Shaw [8, 9]. We examined the structures formed after the dissolution of the graphite and found the structure formed to resemble the structure of cementite (Figure 5.8). Multiple simulations were carried out to calculate the number of

97

carbon atoms graphitized from the diamond tool and averaged it over the number of runs conducted. These numbers are 102, 67, and 52 for the cases (i), (ii), and (iii), respectively. This reflects the effect of orientation of diamond on the amount of graphitization.

Considering the statistical variation during simulations, the difference in cases (i) and (iii) is significant, which suggests that (100) plane is more resistant to graphitization than (110) plane. These observations are in accord with the findings of Seal [102], who reported that (110) plane is the least resistant to graphitization while (100) plane is the most resistant. Komanduri and Shaw [8] conducted grinding tests on iron and observed a similar phenomenon that the diffusion is accompanied by graphitization of diamond at the contact surface. In their studies, a concave shaped area was worn out in the direction transverse to the cutting direction and no graphitization was evident on the rake face.

Nath [107] proposed a theoretical model for direct transformation of diamond to graphite which was recently verified by De Vita *ab initio* [114], using quantum calculations. A coinciding mechanism was observed in this study, namely, the puckered (111) diamond planes flatten to form graphite for case (ii). For case (i), graphitization was observed along the (110) planes similar to the mechanism reported by Komanduri and Shaw [8]. Diamond is first transformed into graphite and the graphite flakes separate from diamond and subsequently diffused into or react with iron atoms in the workpiece. This is due to the fact that diamond, unlike graphite, is relatively insoluble in molten iron [173], which is a key element in the synthesis of diamond [14].

Lambrecht *et al.* [125] showed that diamond nuclei form through graphitic precursor due to preferential relationship between graphitic (0001) and diamond (111) planes. If this is the path one expects for direct transformation of graphite to diamond during diamond synthesis, a similar path should be observed for direct transformation of diamond to graphite [case (ii)]. Thornton and Wilks [15] reported that while there was some wear on the rake face of the tool, most of the wear took place on the flank face, which agrees with
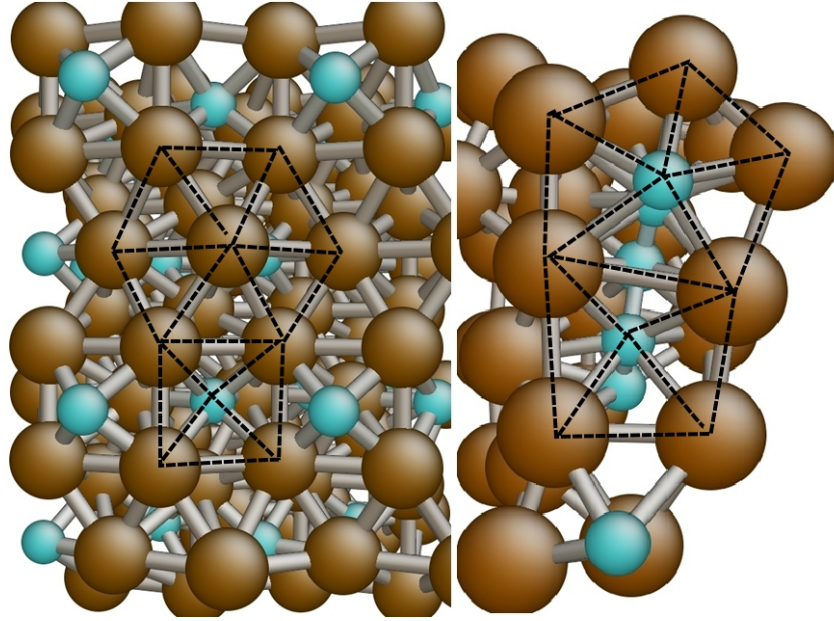
Figure 5.8: (a) Cementite structure, (b) carbide structure observed in one of the simulations in the current study

the results presented in this investigation.

5.5 Conclusions

MD simulations of nanometric cutting of pure iron with a diamond tool convincingly showed initial graphitization of diamond and subsequent formation into iron carbide as the mechanism of wear of diamond in the machining of iron. Consequently, these results are in concurrence with the experimental results of Komanduri and Shaw [8, 9] and the mechanism proposed by Ikawa and Tanaka [10].

Graphitization takes place not atom-by-atom but simultaneously by groups of atoms via an intermediate activated state [Figure 5.5(b)], which is in agreement with the mechanism proposed by Bovenkerk *et al.* [14] for diamond synthesis. It was observed that the diamond (100) plane is most resistant and the (011) plane is least resistant to graphitization with (111) in between. This observation is in agreement with the results of Seal [102].

A direct transition from sp^3 bonding to sp^2 bonding is observed instead of a two stage transition where carbon atoms sublime and condense into graphitic structure, as proposed by Davies and Evans [104]. This is also in agreement with Nath's theoretical model [107] and DeVita's *ab initio* investigation [114].

CHAPTER 6

DEPENDENCE OF THE CRYSTAL ORIENTATION ON GRAPHITIZATION OF DIAMOND IN NANOMETRIC CUTTING OF IRON: AN APPLICATION TO DIAMOND POLISHING

6.1 Introduction

In machining, high temperatures and high mechanical and thermal stresses are generated on the tool. These are the factors that contribute towards wear. Metal cutting involves intensive plastic deformation (shear strain, γ 2 to 5, strain rate, $\dot{\gamma}$ 10^4 s^{-1}) in the vicinity of the cutting edge which makes it easier for chemical reaction and diffusion to take place between the tool and the workmaterial [1, 174]. If the tool (diamond) has great chemical affinity for the workpiece (iron), then wear will be rapid and severe [8–10, 13, 15, 22]. Wear of a diamond tool therefore, depends on its chemical interaction with the workmaterial. In chapter 5, we showed that diamond graphitizes and reacts with iron to form carbide.

Single crystal diamond is anisotropic in nature. Its various physical and mechanical properties, such as wear resistance, hardness depend not only on the crystallographic orientation of the planes but also on the directions of the cutting/polishing. Seal [109] has shown the influence of crystal orientation on the graphitization of diamond. He observed

that {100} planes to be the most resistant and {110} to be least resistant to graphitiza-tion. He pointed out that the directions of fastest graphitization coincide with the fastest growth, and the directions of the slowest graphitization coincide with slowest growth in the diamond synthesis. Graphitization is observed highest in <110> direction and least in <100> direction.
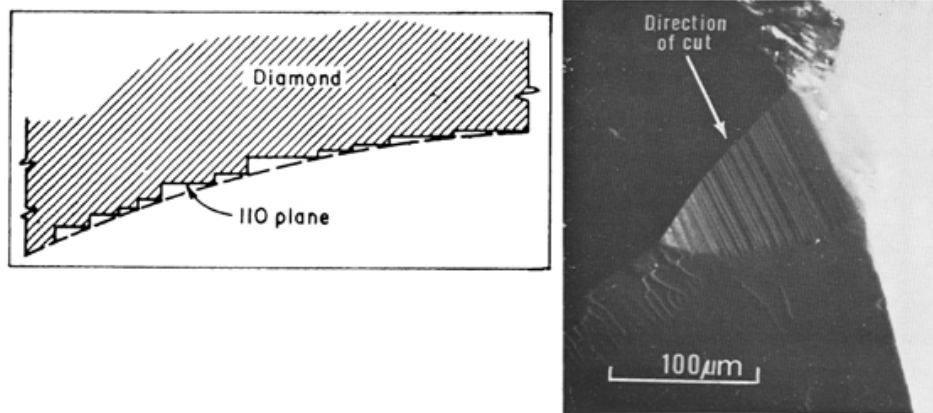
Figure 6.1: (a) Graphical representation of saw tooth marking on diamond grain in the machining of low carbon steel, (b) Micrograph of the wear area of diamond grit [8]

Komanduri and Shaw [8] observed preferential etching of diamond on {110} planes while grinding ferrous materials [Figure 6.1 (a)] which is consistent with the graphitization theory. They reported rapid crater wear on the diamond abrasive in grinding [Figure 6.1 (b)]. Tanaka and Ikawa [13] conducted single grit (diamond abrasive) grinding tests on a mildsteel workpiece and found that diamond exhibits greater wear in <110> direction than in <100> direction on the {100} plane. The rate of graphitization is usually higher on planes {110} and {111} than on {100} planes [175]. Tanaka *et al.* [134] reported that different planes of diamond to have different affinity for forming metal complexes. They concluded that the rate of diamond tool/abrasive wear depends on the surface chemical affinity towards the workmaterial.

102

Thornton and Wilks [15] also reported graphitization as the cause of wear of diamond tool. They reported that clean surfaces generated underneath the tool have different chemical activities than those of the bulk material. They concluded that chemical interaction takes place at the interface and is controlled by the strength of the bonds of the atoms present there, and not by the response of the bulk material. Wilks and Wilks [176] conducted polishing of diamond using a scaife. They concluded that a combination of planes and cutting directions affect wear of diamond. For example, the combination {100} <100>, {110} <100>, and {111} <112> show higher wear rates than {110} <110>, {110} <110>, and {111} <112>.

Sharif Uddin *et al.* [177] investigated the wear of diamond in different crystallographic orientations [combination of (110), (100), and (111) as rake and (100), (100), and (112) as flank, respectively] in nanometric cutting of silicon. Though the wear rate is less compared to the wear observed during the machining of iron, nevertheless, they observed that (110) rake face yields longer tool life and greater wear resistance than (100) and (111) rake planes.

Cheng *et al.* [82] conducted MD simulations of machining of silicon and showed thermochemical wear of diamond. They reasoned that heat generated in cutting decreases the cohesive energy of carbon and weaken the C-C bonding, resulting in tool wear. They calculated wear rate for different orientations of diamond tool and reported (110) plane to have the highest wear rate and (100) plane the least wear rate. Based on this conclusion, they recommended (100) plane to be used as either rake face or flank face. They, however, did not emphasize the direction along the crystallographic plane.

Wear of single crystal diamond tool is of prime concern because it raises machining costs, limits the performance of the tool, and degrades the surface finish before catastrophic tool failure [178]. Hence, it is of paramount importance in minimizing tool wear. Diamond → graphite transformation plays an important role in the wear of diamond while machining

iron (Chapters 4 and 5). As observed in Chapter 5, graphitization occurs in the pico to nanosecond time scale [114–116]. Hence, MD becomes an important tool for investigating such mechanisms. This chapter focuses on the effect of crystallographic orientation of diamond on graphitization and wear in the MD simulations of nanometric cutting of iron. In this attempt, we highlight the preferential planes that are conducive to graphitization (hence wear). Also, we explore various combinations of crystal plane and orientation of cutting edge that demonstrate minimum wear and thus establish a correlation between the orientation of the cutting edge of the tool and wear.

6.2   Setup for MD simulations

The model and the cutting used in this simulation is the same as that used in the Chapter 4 which has been successfully used in demonstrating the mechanism of graphitization/wear of diamond in the machining of iron. Some 4800 atoms in the workpiece and 3000 atoms (varies according to the orientation of the tool) in the tool are considered in the MD simulation of nanometric cutting. Figure 6.2 shows the projected views of the clearance planes a) dodecahedron (011), b) octahedron (111), and c) cube (010) with different orientation of cutting edge used in the simulations. Each tool is shaped with a 10° rake angle and a 5° clearance angle.

6.3   Results

In this investigation, wear of diamond tool with respect to various clearance face orientations, namely, (110), (111), and (100) along different directions during the machining of iron is presented. It may be noted that at the end of the simulation only those atoms which showed separation from the tool were highlighted and does not include those atoms which showed graphitization at the end of the simulation. This was done to observe only those atoms that show wear. Navy blue color was used to highlight these atoms and cyan color
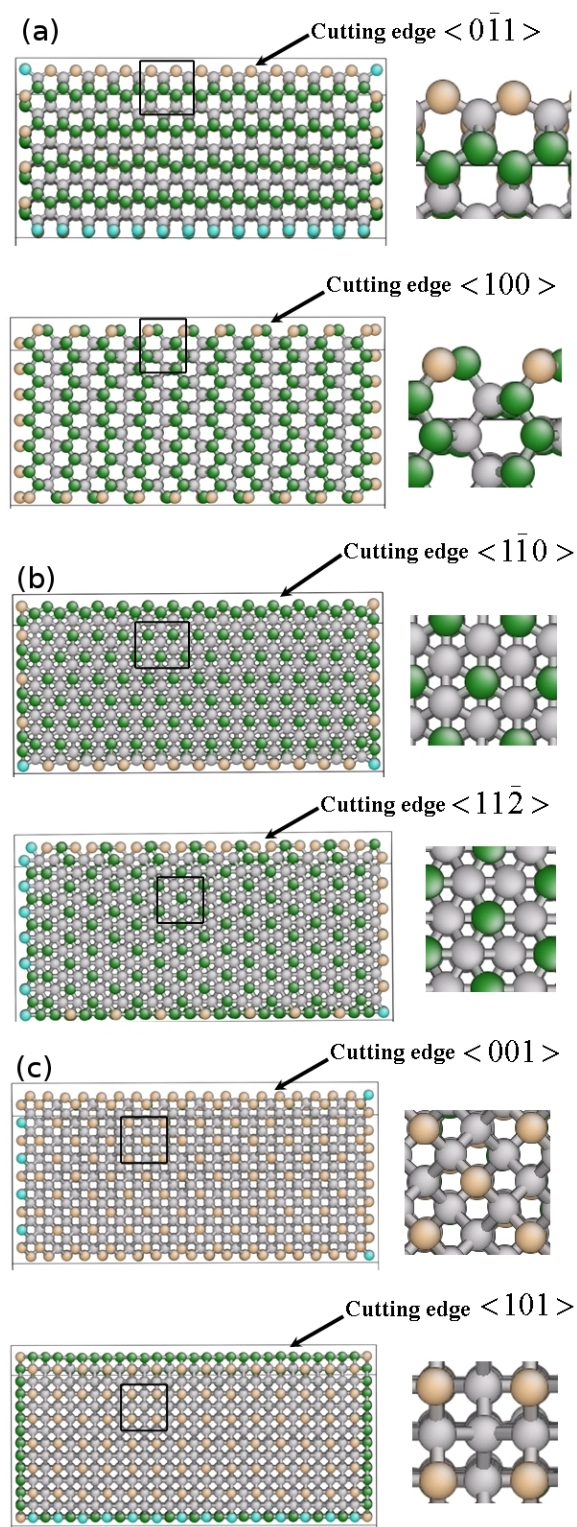
Figure 6.2: Projected view of the clearance plane, (a) dodecahedron (011), (b) octahedron (111), and (c) cube (010), oriented along different cutting edges

was used to represent rest of the tool atoms. These atoms were traced back to the original configuration to emphasize on their location and identify the plane of graphitization or wear.

6.3.1 Case i: Clearance face orientation (011) and direction of cutting edges along a) $<0\bar{1}1>$ and b) $<100>$ directions
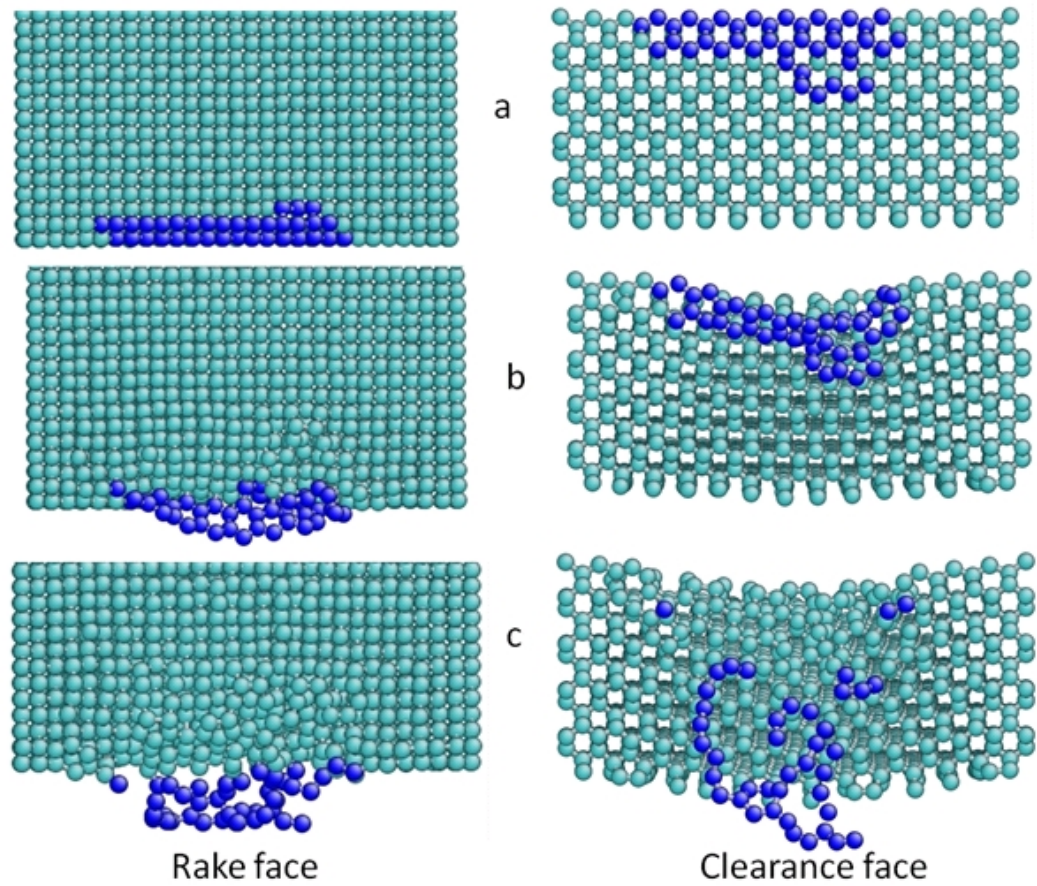
Figure 6.3: Projected views of rake and dodecahedron clearance faces with cutting edge along $<0\bar{1}1>$, [The atoms that get separated from the tool at the end of the simlation are shown in navy blue (dark) color, rest of the atoms are shown in cyan (light) color]

When $<0\bar{1}1>$ was used as the cutting edge of the tool, it was observed that graphi-

tization starts from the cutting edge. The plane of graphitization is contained within the (011) plane. It was observed that diamond graphitizes along the cutting edge first. This indicates that (110) is the plane of graphitization and it propagates preferentially in <011> direction over <100> [Figure 6.3 (a)]. The graphitized atoms eventually separate from the tool and react with the workpiece underneath the clearance face [Figure 6.3 (b) and (c)]. When <100> direction was used as a cutting edge, the carbon atoms did not show any significant sign of graphitization [Figure 6.4 (a)]. However, there are some atoms which still react with the iron atoms. These results [Figure 6.4 (a) to (c)] show a big difference in the graphitization/wear pattern of diamond for the same plane [compare Figure 6.2 (a) and Figure 6.3 (a)].

There are some key differences in the two cutting edges due to crystallographic orientations of diamond lattice. The first difference is the total number of atoms present in the cutting edge that actively participate in machining. It may be noted that the tool is wider than the workpiece. Hence, atoms at the side faces are not participating actively. The second difference is the nature of bonding of the atoms present along the cutting edge (coordination number). In the case of $<0\bar{1}1>$ cutting edge, there are 13 atoms with coordination number two that are present, while in the case of <100>, there are a total of 18 atoms that are present and these are equally divided into coordination numbers 2 and 3. Average coordination number comes out to be ∼2.5. So, not only has the total number of atoms increased in the case of <100>, but also, coordination number is also higher which means more energy is required in order to break these atoms. Even though experimentally the sharp cutting edge of a cutting tool consists of some radius, in simulations, we can get the edge radius at an atomic level resulting in extremely sharp cutting edges. Nevertheless, edges play an important role in the graphitization of diamond [102].
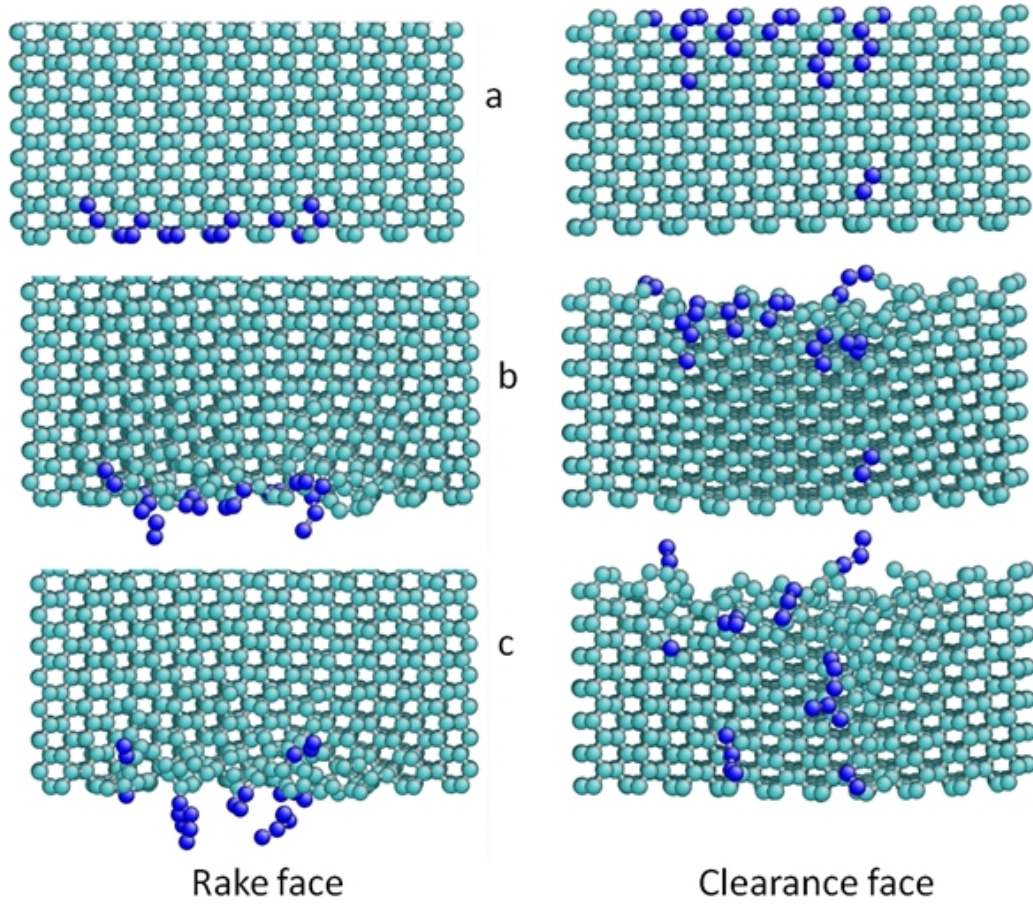
Figure 6.4: Projected views of rake and dodecahedron clearance face with cutting edge along <100>

6.3.2 Case ii: Clearance face orientation (111) and direction of cutting edges along a) <1$\bar{1}$0> and b) <11$\bar{2}$> directions

In both the cases, it was observed that the graphitization starts from the cutting edge. The plane of graphitization is contained within the (111) plane. In the case of <1$\bar{1}$0> cutting edge, it was observed that diamond graphitizes and initiates from the cutting edge first but does not propagate along the cutting edge. Instead, it propagates perpendicular to the cutting edge, i.e, opposite to the direction of cutting. But it stops after two lattices and dissociates before it can reach the other end. This indicates that it propagates preferentially

in $<11\bar{2}>$ direction over $<1\bar{1}0>$ [Figure 6.5 (a)].
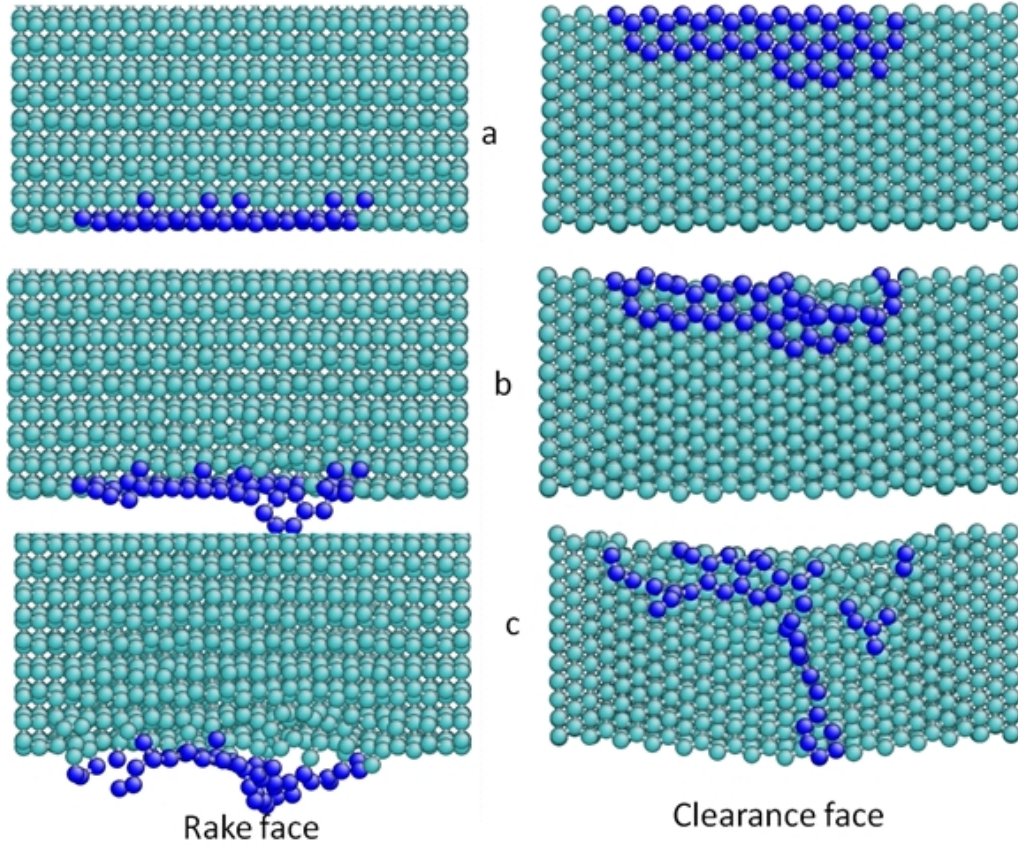
Figure 6.5: Projected views of rake and octohedron clearance face with cutting edge along $<1\bar{1}0>$

The graphitized atoms eventually separate from the tool and react with the workpiece underneath the clearance face [Figure 6.5 (b) and (c)]. In case of $<11\bar{2}>$ cutting edge, more graphitization is observed compared to $<1\bar{1}0>$ cutting edge [Figure 6.6]. The direction of propagation is along $<11\bar{2}>$. This indicates direction $<11\bar{2}>$ is more conducive-to-graphitization than $<1\bar{1}0>$. We can also infer that when conducive-to-graphitization direction is used as the cutting edge, more wear is expected. In other words, the intimate contact of the workpiece along the cutting edge plays an important role. There are 13 atoms with coordination number 3 that are present in the case of $<1\bar{1}0>$ cutting edge whereas only 8
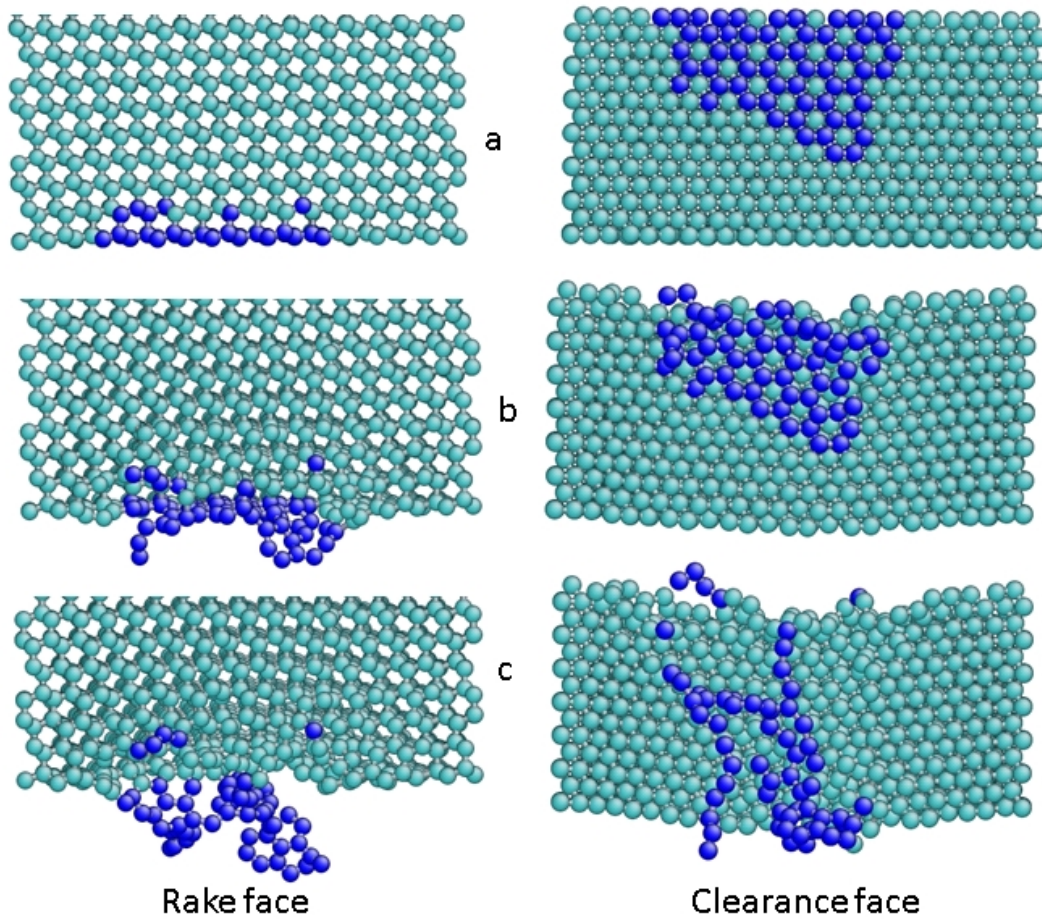
Figure 6.6: Projected views of rake and octohedron clearance face with cutting edge along $<11\bar{2}>$

atoms with coordination number 2 are present in the case of $<11\bar{2}>$ because of the zigzag structure. We can clearly see the importance of the cutting edge due to the crystallographic orientation of the tool.

6.3.3 Case iii: Clearance face orientation (010) and direction of cutting edges along a) $<001>$ and b) $<101>$ directions

As observed previously for other orientations, in both the cases the wear starts from the cutting edge. Interestingly, in the case of $<001>$ cutting edge, it was observed that diamond
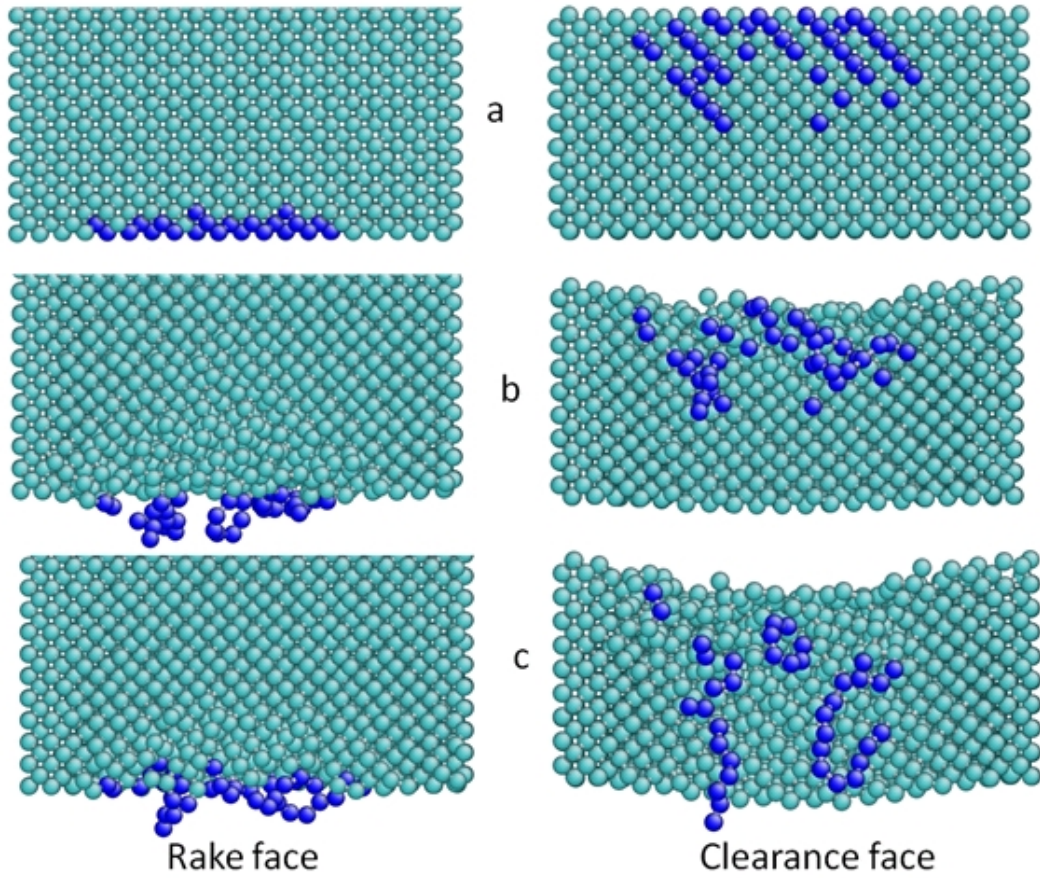
Figure 6.7: Projected views of rake and cube (010) clearance face with cutting edge along <001>

graphitizes and initiates from the cutting edge first but propagates at an angle to the cutting edge [Figure 6.7 (a)]. The plane and direction of propagation was calculated and found that the plane of graphitization is (110) and it propagates along <110> direction. This is due to the exposed (110) atoms from the rake and clearance face. This result is similar to the case ii (110) <1$\bar{1}$0> where plane of graphitization is contained in (110) planes and propagates along <1$\bar{1}$0> direction. This result conforms to the experimental findings that (110) plane is more conducive than (100) plane.

Less wear was observed when the cutting edge was aligned along <101> direction [Figure 6.8]. In this particular case, a few carbon atoms from the cutting edge enter into
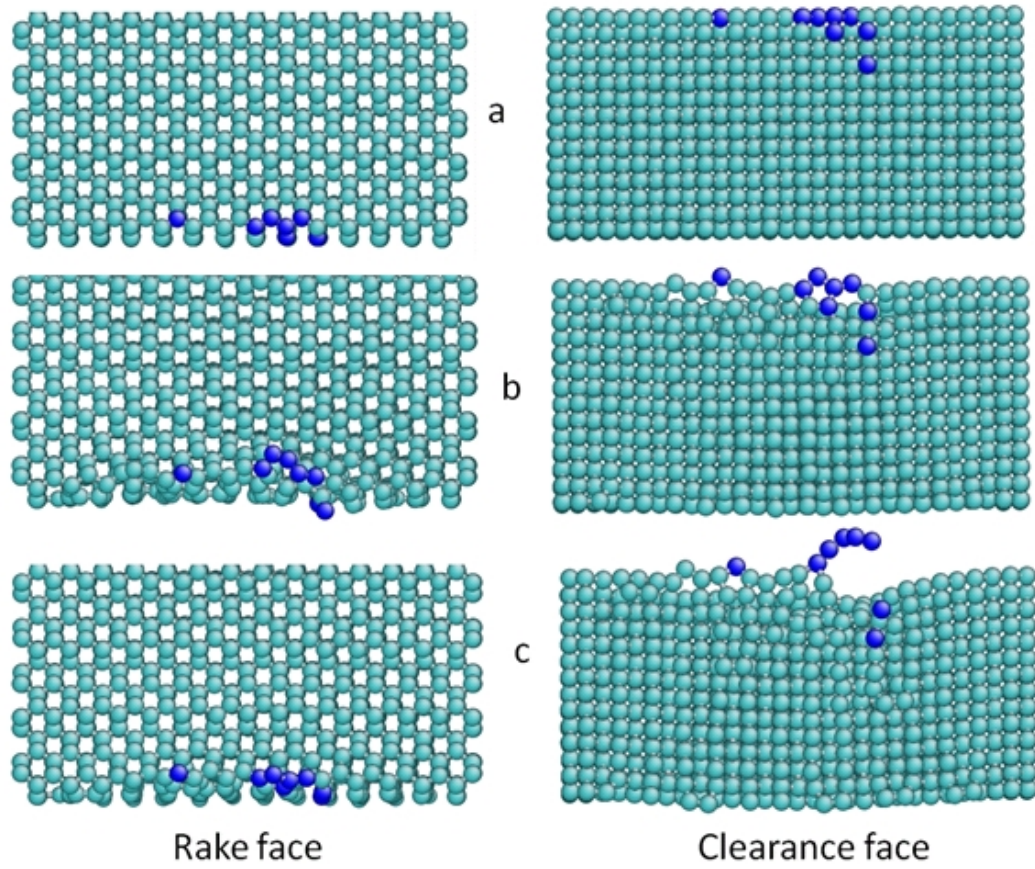
Figure 6.8: Projected views of rake and cube (010) clearance face with cutting edge along <101>

the chip and eventually get carried away from the cutting edge. There are 19 atoms with coordination number 2 in the case of (010) <001> and 14 atoms with coordination number 3 in the case of (010) <101> combination. We observe that the simultaneous contact of tool and workpiece plays a significant role in wear.

6.3.4 Estimation of flank wear

Two different approaches were adopted to estimate tool wear. First, flank wear was measured by calculating the depth H_{max} as shown in Figure 6.9 (a) for all the cases and the values are tabulated in Table 6.1. It was observed that both maximum and minimum wear

112
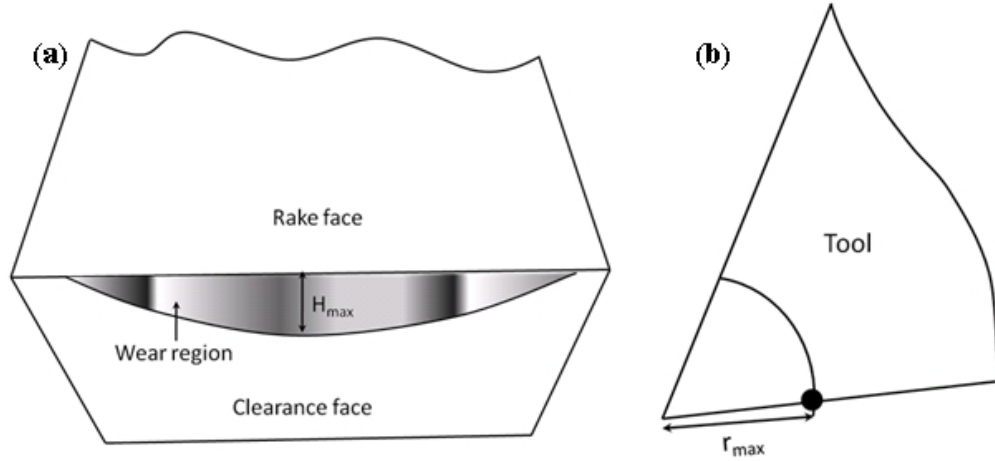
Figure 6.9: Wear estimation, (a) flank wear, (b) effective tool

was shown by plane (010) with combinations <100> and <101>, respectively. It should be noted that in case of (010) <100> combination, the plane of graphitization is (110). Second, in this method, total number of atoms that dissociate was calculated. The wear was defined as:

$$\frac{\text{Total \# of atoms detached}}{\text{Total \# of active atoms}} \qquad (6.1)$$

To calculate the total number of active atoms, distance of the farthest atom from the cutting edge showing wear was calculated for all the cases. The one with the maximum value was chosen as r_{max}. This value comes out to be 8.42 Å. Now the total number of atoms lying inside this radius from the cutting edge [Figure 6.9 (b)] was calculated and used as the active atoms for each case.

This makes calculations independent of the tool dimensions. The values calculated are tabulated in Table 6.1. In this, maximum wear is shown by (111) <11$\bar{2}$> combination and least wear is for (010) <101> combination. In both the calculations the least wear is shown by (010) <101> combination.

113

Table 6.1: Wear estimation of diamond tool along different crystallographic orientations

Clearance plane, cutting edge		Flank wear, H_{max} (Å)	Total wear (%)	Comments
(010)	<001>	2.38	11.5	Wear along (110) plane
	<101>	1.22	3.35	Minimum wear
(111)	<1$\bar{1}$0>	1.46	8.1	
	<11$\bar{2}$>	2.12	14.8	Maximum wear
(011)	<01$\bar{1}$>	2.04	11.8	
	<100>	1.39	6.7	

Table 6.2: Comparison of wear of diamond in machining of iron (present work) and diamond polishing ([176])

Diamond plane	Experimental	MD (present study)
	Hard/Soft directions	Hard/soft cutting edges
Cube (010)	<101>/<001>	<101>/<001>
Octohedron (111)	<$\bar{1}\bar{1}$2>/<11$\bar{2}$>	<1$\bar{1}$0>/<11$\bar{2}$ >
Dodecahedron (011)	<011*>/<100>	<100>/<01$\bar{1}$>

Based on the estimation of wear, for each plane the direction of the cutting edge can be categorized into 'hard' cutting edge and 'soft' cutting edge. Wilks and Wilks [6] conducted diamond polishing experiments on a scaife, in which they categorized resistance of diamond to abrasion into 'hard' and 'soft' directions for different crystallographic orientations of diamond. They showed the importance of direction of abrasion in wear. Table 6.2 gives a comparison of the results.

6.4 Conclusions

In this chapter, dependence of the crystallographic orientation on wear of diamond has been investigated using MD simulations. We observed that wear pattern strongly differs due to changes in the crystal orientations. We conclude that wear not only depends on the crystallographic plane but also on direction of the cutting because along the cutting edge there is intimate contact between cutting tool and the workpiece.

We also conclude that the 'hard' direction in diamond polishing for a particular plane can be used as 'hard' cutting edge for diamond tool in order to minimize wear of the tool. Plane (111) with $<11\bar{2}>$ cutting edge shows maximum wear. In other words, diamond polishing can be done efficiently on plane (111) along $<11\bar{2}>$ direction. We found that the (100) plane with the $<101>$ as cutting edge to show minimum wear. This combination is appropriate for machining with minimum wear on the cutting tool (diamond).

CHAPTER 7

SOLID STATE TRANSFORMATION IN DIAMOND AND IRON AT THE TOOL-CHIP CONTACT: ROLE OF IRON IN THE GRAPHITIZATION OF DIAMOND

7.1 Introduction

Both carbon and iron exhibit allotropic transformations with temperature, i.e. different crystal structures under conditions of different temperature and pressure conditions. For example, carbon exists in cubic and hexagonal forms, and iron in BCC, FCC, or HCP depending upon the pressure and temperature. Moreover, iron and carbon form different compounds with different crystallographic structures. For example, Fe_3C (cementite and austenite). Interestingly, carbon also plays an important role as an alloying element with iron in forming steels and cast irons. This strong affinity of iron for carbon plays a vital role in the wear of diamond tool in the machining of iron and low carbon steels.

Despite diamond's excellent properties as a cutting tool [1], it exhibits rapid wear in the machining of pure iron and low carbon steels [8, 9]. In Chapters 5 and 6 we showed that during machining of iron, diamond graphitizes and reacts with iron to form iron carbide. A similar mechanism was reported by Opitz [174] but for cemented tungsten carbide tool. Because of the high affinity of γ-iron for carbon, tungsten carbide at the surface is reported

to decompose into tungsten and carbon and the carbon atoms diffuse into the surface of the chip. But he also reported that when machining ferrous alloys with cemented tungsten carbide tool, there is a transformation observed from α-iron to γ-iron in the chip. This chapter is devoted towards the understanding of the role of iron in the wear of diamond during machining of iron. Molecular dynamics (MD) simulations of diffusion-couple test were conducted simulating tool-chip contact at experimental speeds (1 m s^{-1}) have been conducted. The results are reported here.

7.2 Model

Four different crystallographic orientations were considered for the diamond surface in contact with a [100] iron surface in the simulation. The diamond surfaces considered were (i) [1$\bar{2}$1], (ii) [111], (iii) [110], and (iv) [110]. The total number of carbon atoms in the simulations were 5819, 5193, 5565, and 5090 for cases (i), (ii), (iii), and (iv) respectively. The count of iron atoms in the simulation were 4500. The atomic velocities in diamond tool and iron workpiece were initialized corresponding to a temperature of 300 K. Then iron and diamond were brought to a firm contact [Figure 7.2 (b)]. The system was then equilibrated for 10^4 timesteps to properly randomize all the vibrational phase angles. The system was then heated to a new temperature (800 K, 1000 K, and 1600 K). The system was then equilibrated and trajectory of atoms was observed for the next 5×10^6 timesteps (total contact time of 500 ps). During the simulation, the temperature of the system was maintained constant using temperature rescale command in the LAMMPS program [57]. Figure 7.2 (c) shows a snapshot at the start of the simulation when iron and diamond were brought into contact.
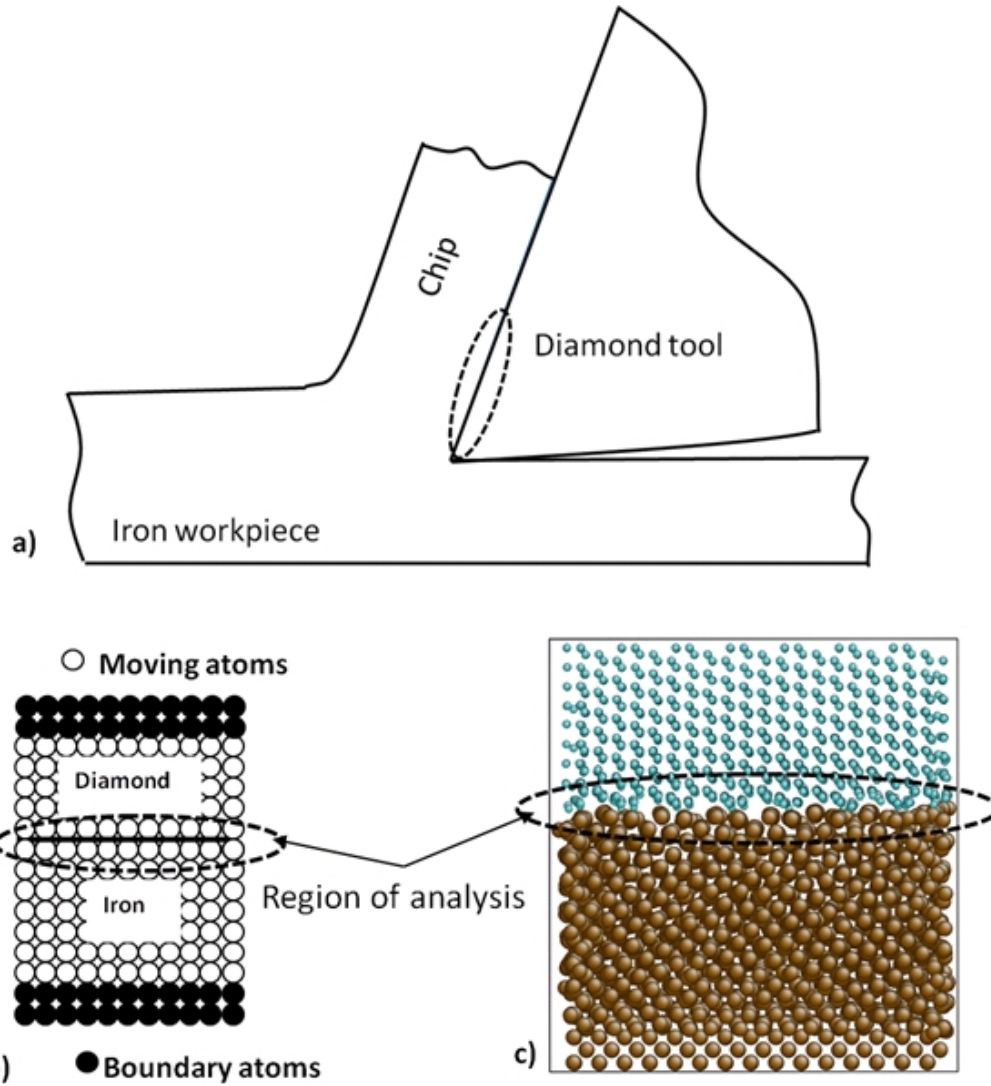
Figure 7.1: (a) Schematic of machining highlighting the tool-chip contact area, (b) the model of tool-chip contact for four cases of diamond surfaces [1$\bar{2}$1], [111], [110], and [100], (c) Case I, [Carbon atoms are shown in cyan color (smaller atoms) and iron atoms in ochre color (bigger atoms)]

7.3 Results

7.3.1 Graphitization of diamond

At 1600 K, it was observed that all the planes except the [100] plane exhibited significant graphitization. In the case of [100] plane, the degree of graphitization was less

noticeable and highly localized. This suggests that (100) is not the natural plane for graphitization.
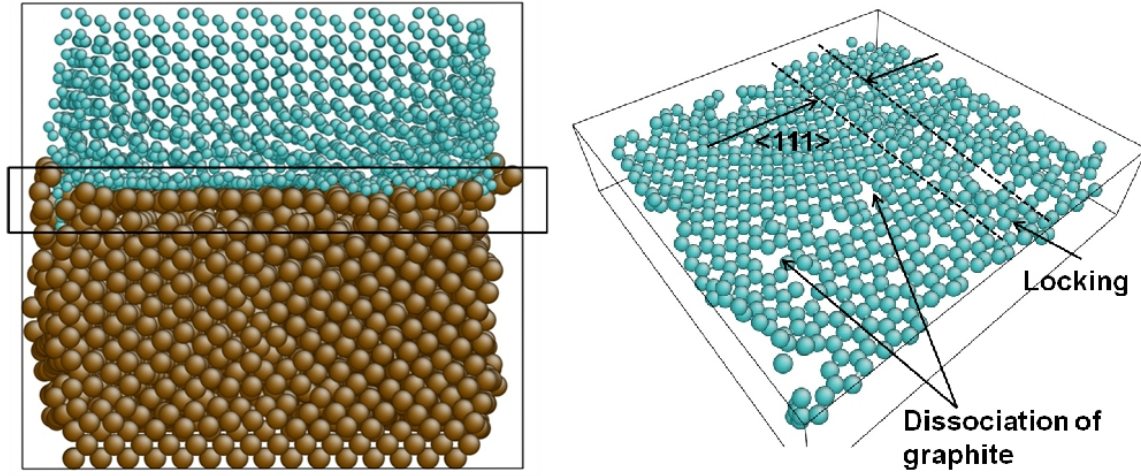
Figure 7.2: (a) Snapshot of the tool-chip contact at time t = 500 ps for Case (i), (b) graphitized diamond [1$\bar{2}$1] surface

Figure 7.2 (a) shows the snapshot of tool-chip contact [Case (i)] at the end of the simulation. The box shown in the figure is the region of observation. Figure 7.2 (b) shows the graphitized [1$\bar{2}$1] surface. It was observed that the surface graphitizes from the edge. The surface first graphitizes in the <101> directions and subsequently graphitization propagates in the <111> directions creating locking along the <101> directions. This observed anisotropy illustrates the preferential direction of graphitization in the <111> for [1$\bar{2}$1] surface. Some dissociation of bonds can also be seen in the figure indicating possible reaction between iron and carbon.

Figure 7.3 (a) shows the Case (ii) at the end of the simulation. It was observed that diamond surface was completely graphitized. The graphite surface can be seen free from locking [Figure 7.3 (b)] which is different than what was observed for Case (i). [111] surface has shown no special preference for graphitization in <1$\bar{2}$1> or <101> directions.

Figure 7.4 (a) shows Case (iii) at the end of the simulation. Surface [110] shows a sim-
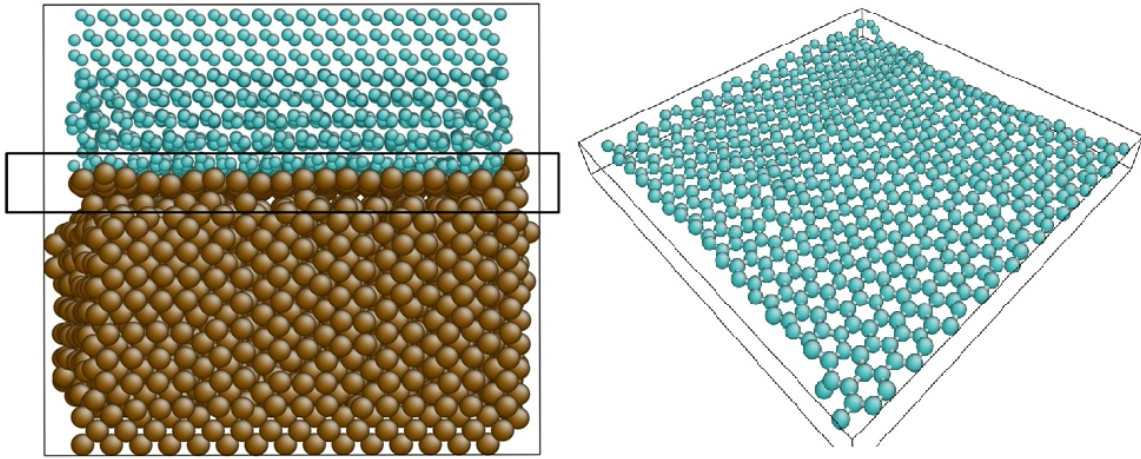
Figure 7.3: (a) Snapshot of the tool-chip contact at time t = 500 ps for Case (ii), (b) graphitized diamond [111] surface
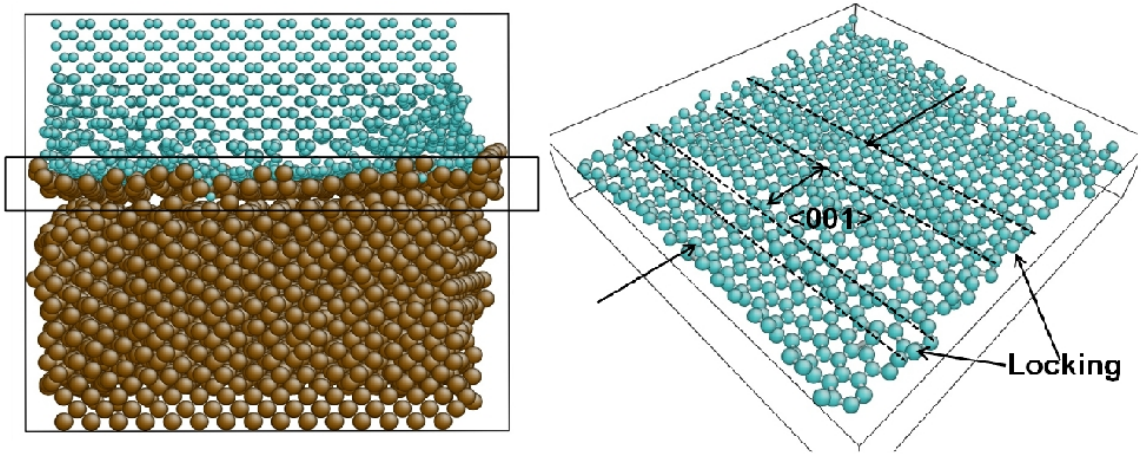
Figure 7.4: (a) Snapshot of the tool-chip contact at time t = 500 ps for case (iii), (b) graphitized diamond [110] surface

ilar pattern of graphitization to that of [121] surface [Figure 7.4 (b)]. In this case, multiple locking was observed suggesting the preferential path of propagation of graphitization in the <110> over the <001> direction. Lesser dissociation of bonds was observed in comparison with Case (i). Case (iv) shows almost no graphitization, though some localized graphite was observed. This suggests that [100] plane is most resistant to graphitization.
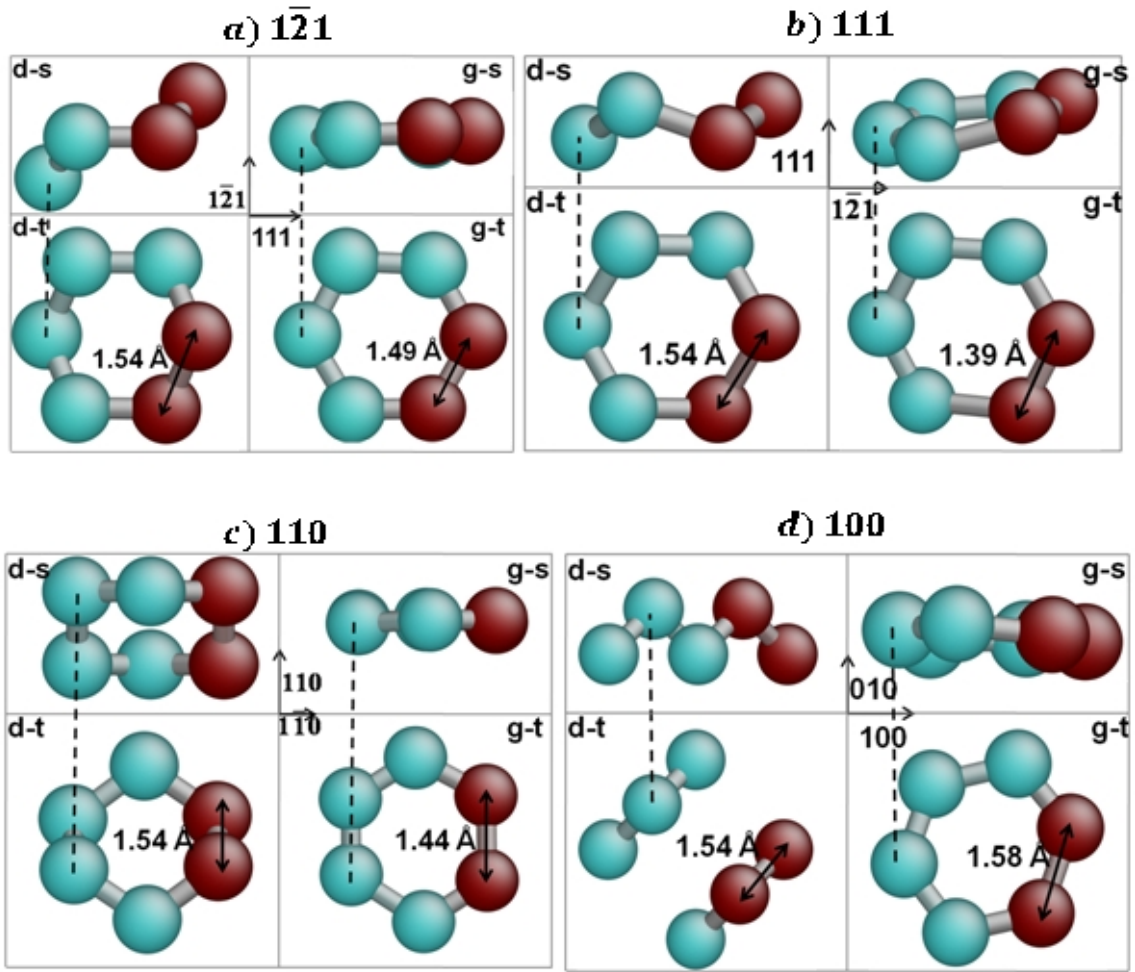
Figure 7.5: Graphitization of diamond along different planes (a)[1$\bar{2}$1], (b) [111], (c) [110], and (d) [110] (d-diamond, g-graphite, s-side view, t-top view)

Figure 7.5 shows four different planes of diamond which graphitize during the simulations at 1600 K. In the figure, diamond and graphite structures are denoted by "d" and "g", respectively, and side and top views are denoted by "s" and "t", respectively. For e.g. g-t represents top view of graphite. Bond distance between two atoms (red colored) from the diamond structure and their corresponding distance in graphitic structure are also shown in the figure. The equilibrium bond distance in a diamond structure [4] is 1.54 Å and that in graphite structure [179] is 1.42 Å. The bond distances in the graphitic structure formed in the cases of (111) and (110) planes are 1.39 Å and 1.44 Å respectively and are closest to

the equilibrium bond distance of graphite (1.42 Å) among all the four planes. These are the planes conducive to graphitization.

A temperature of 1600 K is not sufficiently high to allow diamond to graphitize by itself [11, 97]. This illustrates that the temperature at which diamond is transformed into graphite is lowered in the presence of a metal catalyst, in this case iron. To corroborate this, we conducted a separate simulation wherein diamond alone was heated to 1600 K and no graphitization was observed after 500 ps. This observation is in accordance with the experimental results reported in the literature [10].

At 1000 K, complete graphitization was observed only for [111] and [110] planes. For [1$\bar{2}$1] plane, partial graphitization was observed, and the [100] plane showed no evidence of graphitization. At 800 K, complete graphitization was observed only for [111] plane and no evidence of graphitization was found for [1$\bar{2}$1], [110], and [100] planes. We can observe anisotropy in diamond along different crystallographic orientation as well as the effect of temperature. At all temperatures, (100) plane is most resistant to graphitization. At low temperature, plane [111] seems to be least resistant to graphitization. The results of graphitization are summarized in Table 7.1.

Table 7.1: Graphitization of different crystallographic orientations of diamond, at different temperatures

Orientation	800 K	1000 K	1600 K
[1$\bar{2}$1]	No	Partial	Complete
[111]	Yes	Complete	Complete
[110]	No	Complete	Complete
[100]	No	No	Partial

7.3.2 Transformation in iron
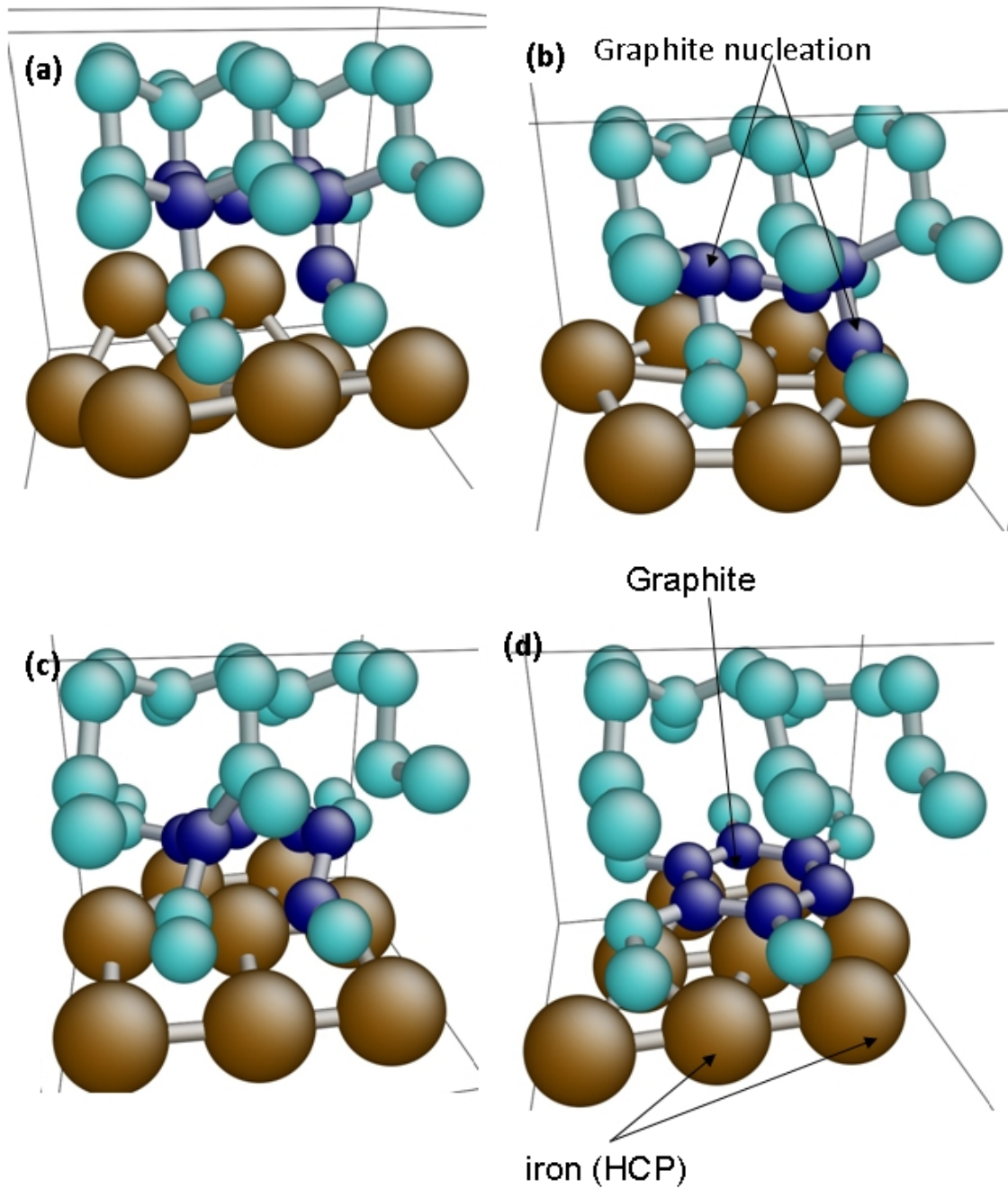
Figure 7.6: Step-by-step solid state transformation in iron [100] and diamond [1$\bar{2}$1] surfaces

Another interesting phenomenon observed here was that during the graphitization of di-

amond, iron atoms at the contact junction transform into an intermediate hexagonal structure. This transformation takes place only at the contact surface and does not affect the bulk. Figure 7.6 shows step-by-step solid-state transformations in iron [100] and diamond [1$\bar{2}$1] surfaces. The atoms shown were isolated from the bulk. The central atom from BCC iron moves in the <010> direction, simultaneously the corner atoms move in the <$\bar{1}$00> directions to accommodate central atom to form a planar structure [Figure 7.6 (b)]. Then the corner iron atoms displace in <001> direction to from the final hexagonal structure [Figure 7.6 (c), (d)]. Net displacement of the corner atoms is in <011> direction. Localized shear is evident from the net displacement of the corner atoms [compare Figure 7.6 (c) and (d)]. Shear may be required to initiate the BCC-to-HCP transformation, as shear tends to stabilize the HCP phase [180].

To verify whether the structural transformation in iron assists graphitization of diamond, separate simulations were conducted for Cases (i) and (ii). In this simulation, iron atoms were not allowed to change their structure. This was achieved by resetting the change in atomic position after the solution of Newtonian equations to zero after each timestep. In other words, no vibrational motion was given to the iron atoms. We observed that there was very little (localized) or no graphitization at all. This is in contrast to the previous results where entire surface is graphitized. This suggests that at high temperatures, structural change in iron plays an important role in the graphitization of diamond.

7.4 *Ab initio* modeling of carbon-iron interaction

We conducted classical trajectory calculations [181, 182] using the Atom Centered Density Matrix Propagation (ADMP) molecular dynamics model [28–30] provided in the Gaussian software [31] on Adamantane ($C_{10}H_{16}$) and different number of iron atoms to further understand the reactivity between iron and carbon. Such a study may shed some light on the nature of the bonding and intermediate structures formed. Adamantane has
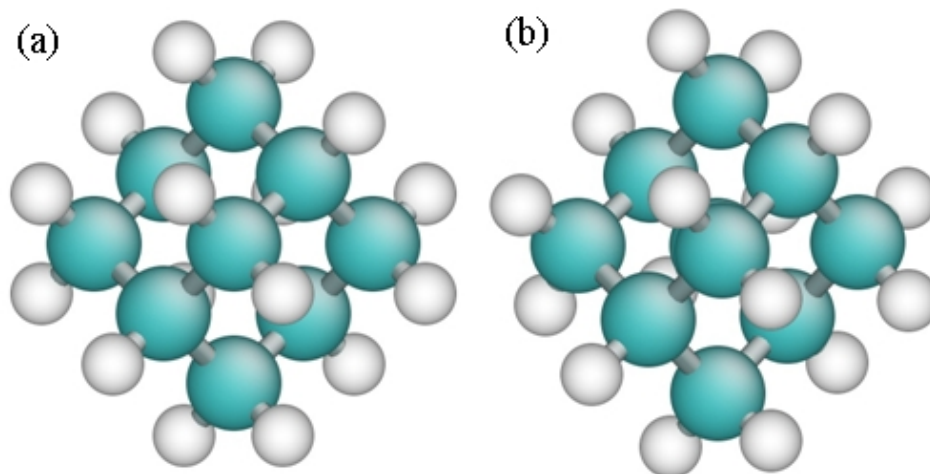
Figure 7.7: Adamantane, (a) initial configuration, (b) after 100 fs

a structure analogus to the unit cell of diamond [183] [See Figure 7.7(a)]. Figure 7.7 (b) shows the adamantane structure after 100 fs. We did not observe any kind of structural deformation over that period. Due to the reactivity between carbon and iron, we should observe some reaction to take place.

Though 100 fs is a very small reaction time, it took $\sim$ 42 hrs on a 3.2 GHz single processor to complete the calculations on adamantane which consists of 76 electrons. The time for calculations increases dramatically as we increase the number of electrons. For example, in the presence of one iron atom (additional 26 electrons) the time increases to 4434 minutes and in the presence of two iron atoms calculation time jumps to $\sim$ 42 hrs, which is 180% increase in time. All the DFT calculations were conducted using 6-31G(d) basis set with initial nuclear kinetic energy of 0.10 Hartree. No thermostat was chosen to control nuclear temperature. Time step taken was 0.1 fs.

7.4.1 Case I: Adamantane in the presence of single Fe atom

Breakage of C-H bonds was observed in the presence of iron atom to release hydrogen H_2. The dissociation energy of C-H bond is 413 KJ/mol and the formation of H-H bond
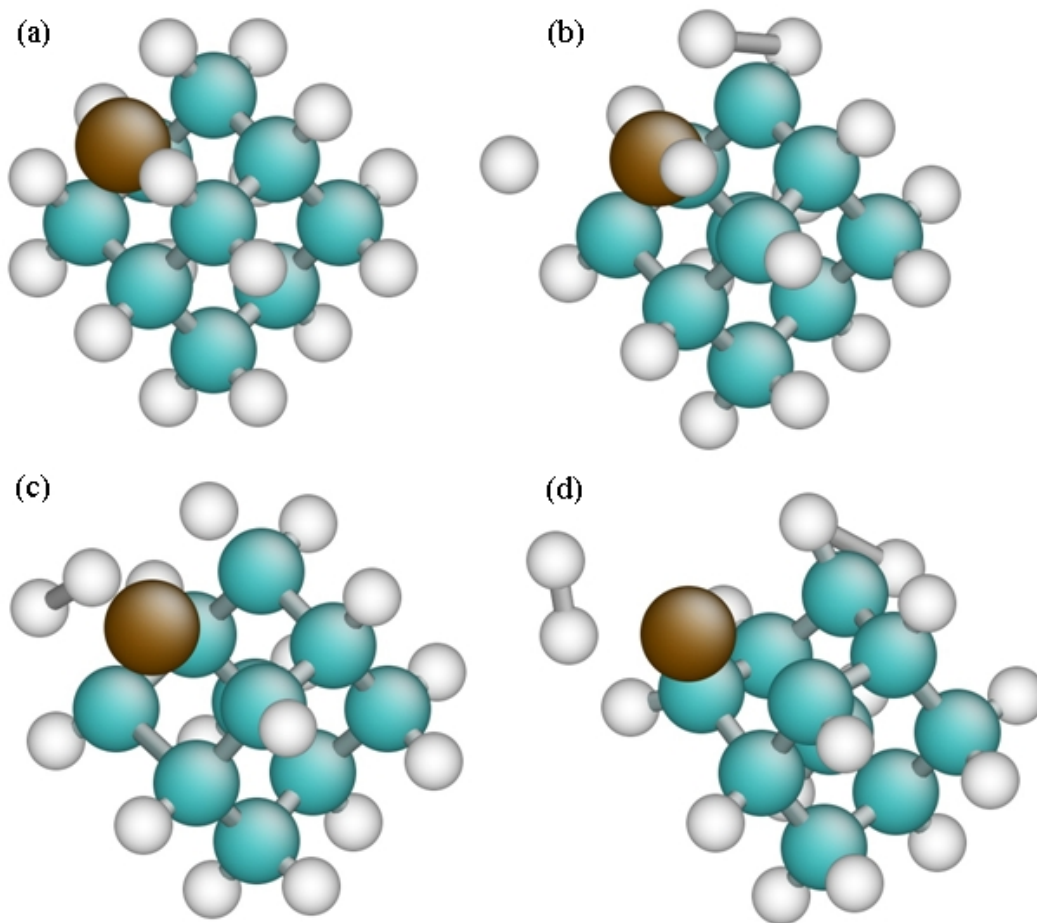
Figure 7.8: Effect of one iron atom on adamantane, (a) 0 fs, (b) 10 fs, (c) 23.5 fs, and (d) 100 fs

436 KJ/mol. The system thus moves to a more stable state in the presence of iron with the extraction of hydrogen molecule. Moreover, iron atom in not forming any bonds with the hydrogen atoms. Just in the presence of iron atom those carbon atom which lost the bonding with hydrogen, must have formed double bonds with the adjacent carbon atoms to satiate their vaccancies. Also, no noticeable structural change was observed in the carbon arranged in the diamond structure.
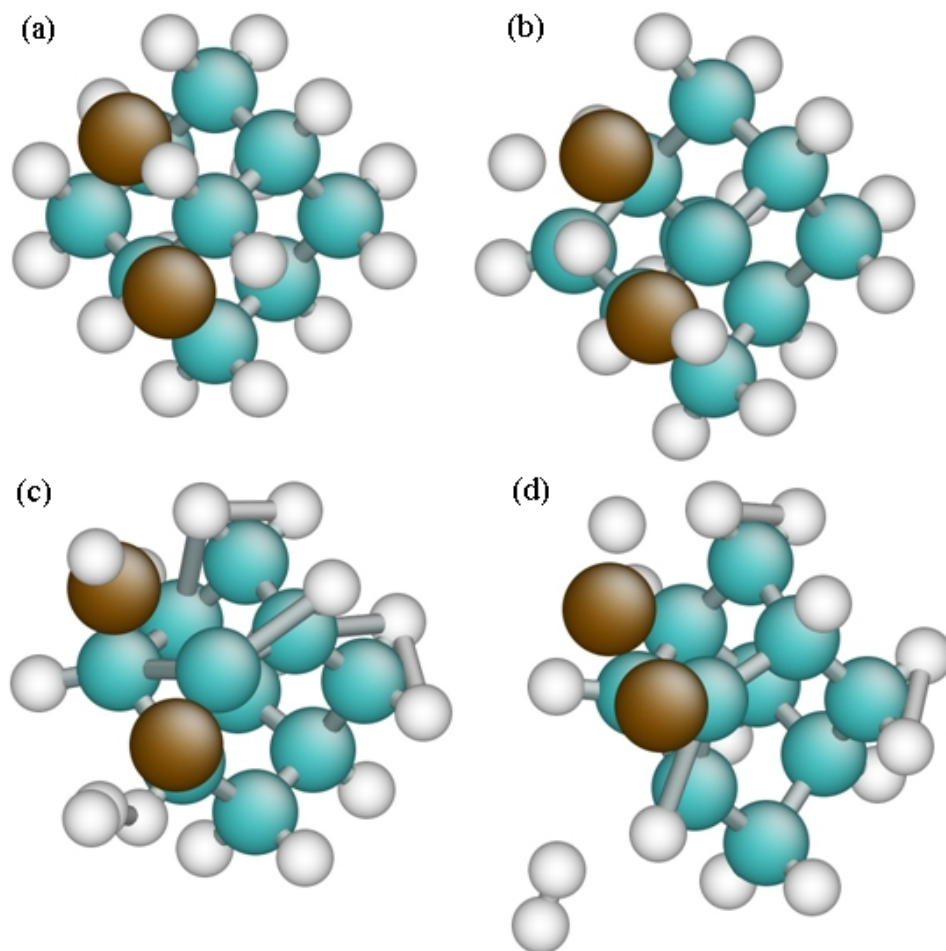
Figure 7.9: Effect of two iron atoms on adamantane, (a) 0 fs, (b) 23.5 fs, (c) 53 fs, and (d) 100 fs

7.4.2 Case II: Adamantane in the presence of two Fe atoms

In the presence of two iron atoms, a hydrogen molecule is extracted along with a hydrogen atom. Two iron atoms come closer to each other and more structural deformation is observed in the carbon atoms arranged in the diamond structure compared to Case i. This structural deformation is prominent in the Section 7.5 (Results) where more number of iron atoms is present resulting in the complete graphitization of diamond.

7.5   Discussion

The transformation in iron from BCC-to-HCP along with graphitization of diamond was observed. The transformation in iron seems to play an important role in the graphitization of diamond. This transformation in iron may be explained by the observations made by other researchers experimentally and theoretically which are discussed as follows.

For carbon atoms, the octahedral site is energetically more favorable than the tetrahedral site [55, 184]. When a large amount of carbon is present around the octahedral sites, extremely high pressure may be generated locally [185]. This may cause the structural transformation of iron from BCC-to-HCP. γ-Fe (FCC) is less stable than ε-Fe (HCP) at high pressures and temperatures because of the positive γ-ε slope [185–188], which could be the reason why α-iron (BCC) converts to ε-Fe (HCP) rather than γ-Fe (FCC).

Tokumitsu and coworkers [185, 186] reported supersaturation of hexagonal solutions during the mechanical alloying of Fe-C powder in an inert (argon) atmosphere by following a path of BCC $\rightarrow$ cementite (Fe_3C) $\rightarrow$ HCP. This rate is reported to be faster with higher carbon concentration during the mechanical alloying of elemental powders ($Fe_{75}C_{25}$, $Fe_{70}C_{30}$, $Fe_{60}C_{40}$, and $Fe_{50}C_{50}$). Similar situation of high carbon concentration (1:1 ratio) and high pressure exist when diamond is in firm contact with iron; hence favoring the transform of BCC iron to HCP structure. In other words, when energy is added to cementite, it is converted into the HCP structure. So, if energy is released by the HCP system, it should revert to cementite structure. At the tool-chip interface, energy is constantly generated during machining. During cooling this energy is released and this may eventually lead to the formation of iron carbide (cementite).

Cementite is unstable at high temperatures and is readily dissociates into iron + graphitic carbon [Fe_3C (cementite) $\rightleftharpoons$ 3Fe + C (graphite)] [189]. So, it is highly unlikely that cementite will be observed at the temperatures used in the simulations (note that these tempera-

tures represent the machining condition at the tool-chip contact and cannot be reduced). The formation of cementite from iron and graphite is exothermic (Δ H$_{form}$ = -30 kJ/-mol) [190], which is in accordance with the observation made by Tokumitsu and coworkers [185, 186] that when energy is added, cementite transforms to HCP structure. On the other hand, ambient pressure is favorable for the formation of cementite (Fe$_3$C) [186]. So, it is less likely cementite will form at high pressure generated at the contact of diamond and iron.

Another possibility is that this transformation is energetically favorable. Shibuta and Maruyama [158] observed regularly allocated transition metal embedded in the hexagonal network of carbon atoms. This creates hexagonal structure of transitional metals. They reported that carbon atom prefers to stay at the apex of hexagonal network. It may be noted that the lattice constant for HCP-iron is 2.48 Å. The distance between centers of two adjacent graphite atoms comes to 2.88 Å. So, if iron atoms find equilibrium positions at the center of graphite, they will form HCP structure with the dimension a = 2.88 Å.

Another perspective is the ease of formation of cementite structure from a hexagonal network [191]. Iron atoms need to accommodate carbon atoms in the ratio of 3:1. The pleated layer of iron atoms in the cementite structure can be deduced from hexagonal structure (A$_3$) of iron, with a = 2.522 Å, and can be defined by a single parameter, the fold-angle at the (11$\bar{2}$0) mirror planes. This proposed dimension of HCP iron earlier by Fasiska and Jeffery [191] is very close to the dimension observed in the simulations (a = 2.88 Å).

7.6   Conclusions

In this chapter, we report an intermediate path of transformation that takes place prior to the formation of carbide and subsequent cause of wear of diamond in the machining/grinding of iron. High temperature and intimate contact between diamond and iron not only transform diamond into graphite but also transform iron into hexagonal structure. This

is because high pressure is generated due to presence of ample amount of carbon around the octahedral sites of iron. This causes iron (BCC) to transform into hexagonal phase. This transformation provides a path that is favorable energetically and geometrically for chemical reaction of carbon with iron to form iron carbide (Fe_3C).

Diamond graphitizes in the presence of iron. Plane (100) is most resistant to graphitization, and plane (111) graphitizes at all elevated temperatures. The temperature at which diamond graphitizes is lowered in the presence of iron. Anisotropy was observed in the graphitization.

Hexagonal iron was observed at the interface between of iron and diamond. The transformation of BCC iron to HCP iron plays an important role in the graphitization of diamond. This path is favorable energetically and geometrically for the subsequent diffusion of carbon into iron, or actually formation of chemical reaction to form iron carbide (Fe_3C).

CHAPTER 8

PARAMETERIZATION OF ANALYTICAL FORMS WITH NEURAL NETWORK

8.1　Introduction

Paul *et al.* [22] reported that oxygen enhances the rate of graphitization of diamond in the machining of iron. In order to understand the effect of oxygen on the wear of diamond, it was necessary to develop potentials that accurately define O-O interactions. Usually empirical potential surfaces are employed for the force fields that represent the system under investigation. In most cases, the functional forms present in these potentials are selected on the basis of chemical and physical intuitions. The parameters of the potential surface are frequently adjusted to fit a very small set of experimental data that comprise of bond energies, equilibrium bond distances and angles, fundamental vibrational frequencies, and measured barrier heights to the reactions of interest. Such potentials generally yield only qualitative or semi-quantitative descriptions of the system dynamics.

One such widely used functional form is the Tersoff potential [38]. This potential represents the interaction terms in diamond/graphite, silicon, and germanium reasonably well. Recently, this potential has been extended to represent various elements other than tetrahedral elements, such as nitrogen [46], boron nitride [192], and silicon dioxide [193]. Due to this, the choice of Tersoff potential becomes obvious to represent the bond interac-

tions between O-O. Moreover, Tersoff potential can be improved by making the parameters parametrized functions of the coordinates defining the instantaneous positions of the atoms of the system. In this chapter, we impliment this approach on Si_5 and $O_2 + O \rightleftharpoons O_3$ system. The following method has been jointly developed with my colleague Mr. Milind Malshe, who will also report these findings in his dissertation. These results have been jointly published in the J. Chem. Phys.[‡]

8.2   General method

We assume that there exists an appropriate parameterized empirical potential function $V(q_i; A, B, C, \ldots)$ where the q_i are the coordinates specifying the configuration of the system, and A, B, C, ... are the adjustable parameters contained within the empirical function. The problem is to obtain the best fit possible to the database by adjustment of the parameters, where some of the parameters may be functions of q_i.

We first partition the parameter set into two parts; those that are to be regarded as functions of q_i and those whose values are independent of q_i. Let $\vec{A}(q_i)$ be a column vector containing M_1 parameters functionally dependent upon q_i, where $A_n(q_i)$, (n = 1, 2, ...,M_1) are the elements of $\vec{A}(q_i)$. The remaining M_2 parameters, B_j(j = 1, 2, ..., M_2) are independent of q_i. They form a column vector $\vec{B}$. The objective is to adjust the functional dependence of the parameters in $\vec{A}$ upon the q_i and the parameters in $\vec{B}$ so as to minimize the difference between the potential given by $V(q_i, A, B)$ and the target values for the potential.

Figure 8.1 shows a flow diagram of the overall NN method for the adjustment of the parameters of $V(q_i, \vec{A}, \vec{B})$. The input vector, $\vec{P_k}$ of the NN comprises of a set of q_i that specify the kth configuration of the system. Typically, the elements of $\vec{P_k}$ are interatomic distances,

---

[‡]M. Malshe, **R. Narulkar**, L. M. Raff, M. Hagan, S. Bukkapatnam, P. M. Agrawal, and R. Komanduri, "Parameterization of Analytical Interatomic Function using Neural Network (NN)," J. Chem. Phys. Vol. 129, (2008) pp. 044111/1-9
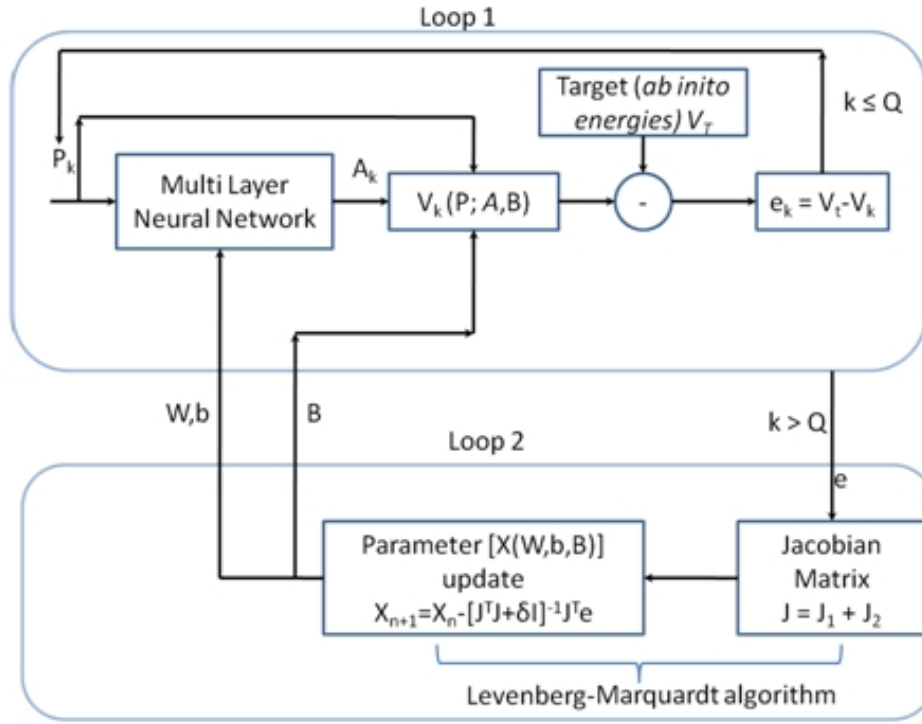
Figure 8.1: Flow diagram for the operation of the NN procedure for empirical parameter adjustment to a database. Q is the number of points in the database [194]

bond angles, and dihedral angles. The elements of $\overrightarrow{P_k}$ are combined with the weight and bias matrices of the network, $\overrightarrow{W}$, and $\overrightarrow{B}$, respectively, to produce the corresponding elements of $\overrightarrow{A_k}$. These results are then used along with the current values of the elements of $\overrightarrow{B}$ to compute $V\left(\overrightarrow{P_k}, \overrightarrow{A_k}, \overrightarrow{B}\right)$. This potential is combined with the target potential, $V_{T,k}$, for the kth configuration, which is generally obtained from *ab initio* calculations at some level of accuracy to compute the interpolation error $\vec{e}_k$ for the kth input vector $\overrightarrow{P_k}$:

$$e_k = V_{T,k} - V\left(\overrightarrow{P_k}, \overrightarrow{A_k}, \overrightarrow{B}\right) \tag{8.1}$$

As indicated in Loop 1 of Figure 8.1, this procedure is repeated for each of the Q

configurations present in the database. In the general case, the NN for a system containing n atoms will usually be a two-layer network comprising of one hidden layer and an output layer along with the input vector. The input vector will have at least (3n-6) elements to specify the system configuration. However, in some cases, it may be convenient to over specify the configuration. For example, a common choice is the ensemble of interatomic distances or inverse distances. If this choice is made, the input vector will contain $n*(n-1)/2$ elements. The number of neurons in the hidden layer, K, is arbitrary. The optimum value is generally determined by empirical investigation to find the minimum value of K required to achieve sufficient interpolation accuracy. The output layer contains M_1 neurons that produce the M_1 required values of the elements in A_k.

In the next step, the Levenberg-Marquardt algorithm [195] is employed to update the elements of $\vec{B}$ and the weight and bias matrices of the NN so as to minimize the error. This procedure requires computation of the Jacobian matrix which consists of partial derivatives of the error ($\vec{e}_k$) with respect to the parameters of the potential. Since the parameters in $\vec{A}_k$ are treated differently than the parameters in $\vec{B}$, we split the computation of the Jacobian matrix into two parts. We first compute J_1, which comprises the partial derivatives of $\vec{e}_k$(k = 1, 2, 3, ..., Q) with respect to the weights and biases of the NN that determine the elements of $\vec{A}_k$. In the second step, we calculate the derivatives of $\vec{e}_k$(k = 1, 2, 3, ..., Q) with respect to the elements of B to obtain J_2. The total Jacobian, J, is a $Q \times (N + M_2)$ matrix, where N is the total number of elements in $\vec{W}$ and $\vec{b}$. J is obtained from concatenation of J_1 and J_2. This overall procedure is illustrated diagramatically in Loop 2 of Figure 8.1.

After the execution of one epoch of optimization using the Levenberg-Marquardt procedure, the updated weights and biases along with the updated B matrix are returned to Loop 1 for execution of the next cycle of optimization. The iterative procedure is continued until convergence is attained using either an early-stopping procedure with a validation set or some other suitable method.

In order to avoid being trapped in the local minima of the multi-dimensional parameter hyperspace and to average out statistical errors present in the fitting, the NN procedure is repeated several times using different initial guesses for $\overrightarrow{W}$, $\vec{b}$, and $\vec{B}$ and a different partitioning of the database into training, testing, and validation sets to generate a committee of networks. The final predicted value for the potential can be taken as the average of the committee of networks or as the result from the single NN producing the best fit can be used.

8.3 Fitting of Tersoff functional form

For an arbitrary system, the Tersoff function E is given by equation 8.2.

$$\sum_i E_i = \frac{1}{2}\sum_{i \neq j} V_{ij},$$ (8.2)

where, V_{ij} is the interaction between atom i and j which is given by:

$$V_{ij} = f_c(r_{ij})\left[f_R(r_{ij}) + b_{ij}f_A(r_{ij})\right],$$ (8.3)

f_c is the cutoff function, f_R and f_A are repulsive and attractive parts of the potential, respectively, and are given by:

$$f_R(r_{ij}) = C_{ij}\exp(-\lambda_{ij}r_{ij}),$$ (8.4)

$$f_A(r_{ij}) = -D_{ij}\exp(-\mu_{ij}r_{ij}),$$ (8.5)

$$f_c(r_{ij}) = \begin{cases} 1, & r_{ij} < R_{ij} \\ \frac{1}{2} + \frac{1}{2}\cos\left[\pi\frac{(r_{ij}-R_{ij})}{(S_{ij}-R_{ij})}\right], & R_{ij} < r_{ij} < S_{ij} \\ 0, & rij > S_{ij} \end{cases}$$ (8.6)

b_{ij} is a three-body interaction which is given by:

$$b_{ij} = \chi_{ij}(1 + \beta_i^{n_i}\xi_i^{n_i})^{-\frac{1}{2n_i}},$$ (8.7)

where,

$$\xi_i = \sum_{k \neq i,j} f_c(r_{ik})\omega_{ik}g(\theta_{ijk}),$$ (8.8)

and

$$g(\theta_{ijk}) = 1 + \frac{c_i^2}{d_i^2} - \frac{c_i^2}{[d_i^2 + (h_i - cos\theta_{ijk})^2]}, \tag{8.9}$$

The cut off function, $f_c(r_{ij})$, is given by Eq (8.6). Its use produces a potential E that is continuous with continuous first derivatives. However, the second derivatives are discontinuous at the cutoff points, R_{ij} and S_{ij}.

Physical considerations and preliminary calculations suggest that C and D parameters in the two-body terms should be strongly dependent upon the Si_5 configuration. These multiplicative parameters play a key role in determining the Si-Si bond strength, which is very different in Si_3 than is the case for Si_2. Therefore, we place C and D in matrix $\vec{A}_k$ that contains the parameters whose values are to be functions of the configuration of the system. The $\vec{B}$ matrix comprises the remaining nine parameters. With these assignments, $\vec{A}_k$ becomes a (2×1) column vector while $\vec{B}$ is a (7×1) vector.

We have adopted a simple (1-2) NN shown in Figure 8.2 to compute C_{ij} and D_{ij}. When the $\vec{P}_k$ are presented to the network in Loop 1 of Figure 8.2, each of the three elements of $\vec{P}_k$ are input into the NN, one at a time, to produce the corresponding values of C and D for that particular element. This simple choice for the NN makes the values of the two-body C and D parameters linear functions of the corresponding interparticle distance:

$$C_{ij} = W_1 r_{ij} + b_1 \tag{8.10}$$

$$D_{ij} = W_2 r_{ij} + b_2 \tag{8.11}$$

where C_{ij} and D_{ij} are the parameters that are associated with the two-body, Tersoff term whose input elements are r_{ij}. After computation of the error vector $\vec{e}$ whose elements are the errors for all Q configurations in the database, control is transferred to Loop 2 in Figure 8.2 for the execution of one training epoch using the Levenberg-Marquardt algorithm [195]. The required J_1 matrix has dimensions $Q \times (N + M_2)$, where N is the number of weights and biases in the NN. For the present illustrative example, N = 4 and M_2 = 7. The elements
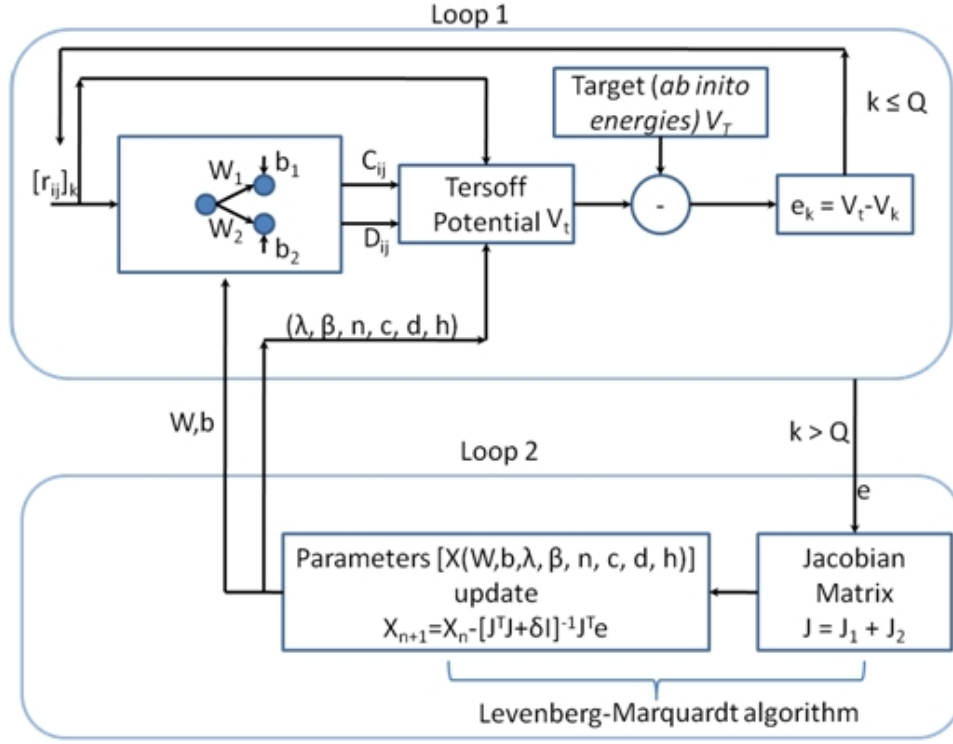
Figure 8.2: Flow diagram showing the procedure for the operation of the NN for empirical parameter adjustment to a database for a Tersoff potential with C and D treated as functions of the 2-body interparticle distances. Q is the number of points in the database [194]

of J_1 are the derivatives of the errors with respect to the weights and biases of the NN. Therefore, the J_1 matrix is given by Eq (8.12)

$$J_1 = \begin{bmatrix} \partial e_1/\partial W_1 & \partial e_1/\partial W_2 & \partial e_1/\partial b_1 & \partial e_1/\partial b_2 & 0 & 0 & \dots & 0 \\ \partial e_2/\partial W_1 & \partial e_2/\partial W_2 & \partial e_2/\partial b_1 & \partial e_2/\partial b_2 & 0 & 0 & \dots & 0 \\ \vdots & \vdots & \vdots & \vdots & 0 & 0 & \dots & 0 \\ \partial e_Q/\partial W_1 & \partial e_Q/\partial W_2 & \partial e_Q/\partial b_1 & \partial e_Q/\partial b_2 & 0 & 0 & \dots & 0 \end{bmatrix}_{Q \times 11} \tag{8.12}$$

The elements of J_1 are most conveniently computed using the standard chain rule. That is

137

$$\frac{\partial e_J}{\partial W_1} = \frac{\partial (V_{T,J} - V_J)}{\partial W_1} = -\sum_i^9 \sum_{j>i}^{10} \frac{\partial e_J}{\partial C_{ij}} \frac{\partial C_{ij}}{\partial W_1}, \tag{8.13}$$

$$\frac{\partial e_J}{\partial W_2} = \frac{\partial (V_{T,J} - V_J)}{\partial W_2} = -\sum_i^9 \sum_{j>i}^{10} \frac{\partial e_J}{\partial D_{ij}} \frac{\partial D_{ij}}{\partial W_2}, \tag{8.14}$$

with analogous expressions for the derivatives of e_k with respect to b_1 and b_2. The J_2 Jacobian is the matrix of derivatives of the errors with respect to the potential parameters contained in vector B. J_2 is given by Eq (8.15):

$$J_2 = \begin{bmatrix} 0 & \dots & \partial e_1/\partial \lambda & \partial e_1/\partial \mu & \partial e_1/\partial n & \partial e_1/\partial c & \partial e_1/\partial d & \partial e_1/\partial h \\ 0 & \dots & \partial e_2/\partial \lambda & \partial e_2/\partial \mu & \partial e_2/\partial n & \partial e_2/\partial c & \partial e_2/\partial d & \partial e_2/\partial h \\ \vdots & \ddots & \vdots & \vdots & \vdots & \vdots & \vdots & \vdots \\ 0 & \dots & \partial e_Q/\partial \lambda & \partial e_Q/\partial \mu & \partial e_Q/\partial n & \partial e_Q/\partial c & \partial e_Q/\partial d & \partial e_Q/\partial h \end{bmatrix}_{Q \times 11}, \tag{8.15}$$

The gradients of the Tersoff potential with respect to the parameters contained in the B vector are given by Equations (8.16) to (8.22).

$$\frac{\partial V_{ij}}{\partial \lambda_{ij}} = -r_{ij} f_C(r_{ij}) f_R(r_{ij}), \tag{8.16}$$

$$\frac{\partial V_{ij}}{\partial \mu_{ij}} = -r_{ij} b_{ij} f_C(r_{ij}) f_A(r_{ij}), \tag{8.17}$$

$$\frac{\partial V_{ij}}{\partial \beta_i} = -\frac{1}{2} b_{ij} f_C(r_{ij}) f_A(r_{ij}) \left[\frac{\xi_{ij}^{n_i} \beta_i^{n_i-1}}{(1 + \xi_{ij}^{n_i} \beta_i^{n_i})} \right], \tag{8.18}$$

$$\frac{\partial V_{ij}}{\partial n_i} = \frac{1}{2} b_{ij} f_C(r_{ij}) f_A(r_{ij}) \left[\frac{ln(1 + \xi_{ij}^{n_i} \beta_i^{n_i})}{n_i^2} - \frac{\xi_{ij}^{n_i} \beta_i^{n_i} (ln\xi_{ij} + ln\beta_i)}{n_i(1 + \xi_{ij}^{n_i} \beta_i^{n_i})} \right], \tag{8.19}$$

138

$$\frac{\partial V_{ij}}{\partial c_i} = -b_{ij}f_C(r_{ij})f_A(r_{ij})\frac{\xi_{ij}^{n_i-1}\beta_i^{n_i}}{(1+\xi_{ij}^{n_i-1})}$$

$$\times \left[\sum_{k(\neq i,j)}\left(\frac{c_i}{d_i^2} - \frac{c_i}{(1+d_i^2+(h_i-\cos\theta_{ijk})^2)}\right)\omega_{ik}f_c(r_{ik})\right]$$

(8.20)

$$\frac{\partial V_{ij}}{\partial d_i} = -b_{ij}f_C(r_{ij})f_A(r_{ij})\frac{\xi_{ij}^{n_i-1}\beta_i^{n_i}}{(1+\xi_{ij}^{n_i-1})}$$

$$\times \left[\sum_{k(\neq i,j)}\left(-\frac{c_i^2}{d_i^3} - \frac{c_i^2 d_i}{(1+d_i^2+(h_i-\cos\theta_{ijk})^2)}\right)\omega_{ik}f_c(r_{ik})\right]$$

(8.21)

$$\frac{\partial V_{ij}}{\partial h_i} = -b_{ij}f_C(r_{ij})f_A(r_{ij})\frac{\xi_{ij}^{n_i-1}\beta_i^{n_i}}{(1+\xi_{ij}^{n_i-1})}$$

$$\times \left[\sum_{k(\neq i,j)}\left(-\frac{c_i^2 d_i(h_i-\cos\theta_{ijk})}{(1+d_i^2+(h_i-\cos\theta_{ijk})^2)}\right)\omega_{ik}f_c(r_{ik})\right]$$

(8.22)

8.3.1 Si$_5$ database

For a general system, the Tersoff parameters differ for each unique bonding pair. In the present case, all pairs correspond to Si-Si bonds. Consequently, the $i - j$ subscripts on the potential parameters can be dropped. This simplification leaves a total of 12 parameters, C, D, λ, μ, R, S, β, n, ω, c, d, and h. In this illustration, we elected to set the value of ω to unity and those for R and S to 2.850 Å and 3.000 Å, respectively. This decision leaves nine parameters to be adjusted to the *ab initio* Si$_5$ database.

The values of the elements of A and B obtained after about 800 training epochs using the Levenberg-Marquardt algorithm for three particular initial choices for the parameters are given in Table 8.1. A more quantitative measure of the fitting accuracy may be obtained from the computed rms error at each of the 10,202 points in the database. The best result we obtained using three different initial estimates of the fitting parameters is an rms error of 0.0148 eV (1.43 kJ mol^{-1}) for solution-1 in Table 8.1. The other two solutions (Solutions 2 and 3 in Table 8.1) both yield an rms error higher by 0.0005 eV. Before optimization, using

the flow diagram shown in Figure 8.2, the rms error using the initial guess for Solution-1 was 14.083 eV. This large fitting error is reduced to by a factor of 951.6 in about 800 iterations (epochs) of the loop shown in Figure 8.2. These iterations required about 80 hours of CPU time on a single processor with a 2.6 GHz clock speed.

Table 8.1: Parameters for the modified Tersoff potential with parameters C and D treated as linear functions of the two-body interatomic distance [194]

Parameter	Solution I	Solution II	Solution III
W_1 (eV/Å)	0.0000	-243.721813	-243.77000676
W_2 (eV/Å)	-0.0014	0.135643281	-0.472394167
b_1 (eV)	713.4128	398.4742375	398.5871931
b_2 (eV)	410.1866	-0.892099763	- 0.727862883
λ (Å^{-1})	2.0815	1.637737984	1.637775465
μ (Å^{-1})	1.3273	1.637755192	2.023039578
β	0.3077	0.001906998	0.001906998
n	0.0098	0.009909063	0.009909061
c	1068.6001	10686.00999	10686.00999
d	18.5451	18.553194	18.553194
h	-1.2943	0.294251	0.294251
rms error (eV)	0.0148	0.0153	0.0153

The distribution of errors at the 10,202 points in the database is shown as a histogram in Figure 8.3. As can be seen, the large majority of errors lie between -0.02 eV and +0.02 eV. Solution-1 in Table 8.1 is close to the best fit possible using a Tersoff potential form [38] for the Si_5 system where C and D are assumed to be linear functions of the Si-Si distance involved in the two-body term.
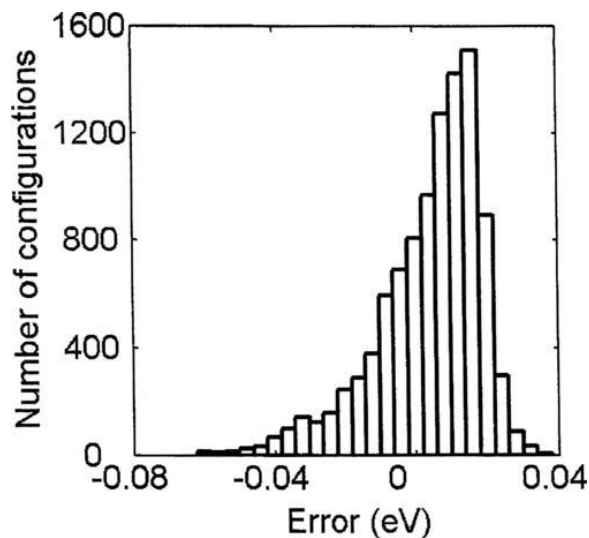
Figure 8.3: Distribution of errors for Solution-1 in Table 8.1. Total number of points in the database is 10,202. The rms error for the distribution is 0.0148 eV $(1.43 \text{ kJ mol}^{-1})$ [194]

If more of the parameters were made simultaneous functions of all the elements of $\vec{P}_k$ with a more elaborate NN employed to adjust the weights and biases, the results would be substantially improved. However, even the present simple treatment yields fitting accuracy comparable to or better than most previously reported generalized fitting methods.

8.3.2 $O_2 + O \rightleftharpoons O_3$ database

This method is extended to fit a database that is the lowest of the singlet and pentet O_3 energies obtained from electronic structure calculations for a large ensemble of O_3 configurations that sample the configuration space important in dissociation dynamics. Since only three internal coordinates are required to specify the O_3 configuration, it is possible to use a simple grid technique to sample the entire configuration space.

We employ the two O-O interatomic distances and the included angle in the grid sampling. The nodes of the grid are defined by varying each O-O distance from 1.0 Å to 2.9 Å

141

in increments of 0.10 Å while the angle spans the range from 100° to 132° in increments of 1.6°. This yields a total of 8,000 nodes.

Electronic structure calculations [31] using unrestricted, fourth-order Möller-Plesset perturbation theory [196] with singlet, doublet, and quartet excitations [UMP$_4$(SDQ)] and a 6-31G** basis set were executed on the O$_3$ configuration present at each of the 8,000 nodes. In each case, the singlet, triplet, and pentet energies were computed. For convenience of interpretation, the resulting energies were converted to eV relative to the energy of three separated, ground-state oxygen atoms.

The final *ab initio* target database was obtained by selecting the lowest of the three energies at each O$_3$ configuration. Except in a small region of configuration space corresponding to a variation of less than 0.2 Å in the O-O separation, the lowest O$_3$ energy is either singlet or pentet. Consequently, for purposes of this fitting study, we have not included in the database those points at which the triplet is at the lowest energy state. Some of the points on the grid lie outside the cutoff range for the Tersoff potential. Since those points will have no effect on the fitting process, they were not included in the final database. Occasionally, the UMP$_4$ (SDQ) calculations failed to converge or exhibited a discontinuity. These results were also not included in the final database. These procedures produced a final database comprising of the lowest energy at 4,102 O$_3$ configurations.

We have also executed UMP$_4$ (SDQ) calculations on O$_2$ with a 6-31G** basis set. The O-O distance was varied from 1.0 Å to 3.9 Å in increments of 0.10 Å. In its electronic ground state, O$_2$ is triplet. As the molecule dissociates to O + O, the multiplicity changes to pentet. The UMP$_4$ calculations indicate the triplet and pentet surfaces cross at an O-O separation of about 2.15 Å (Figure 8.4), which corresponds to an O-O bond extension of about 0.9 Å beyond equilibrium. We have assumed that this crossing point corresponds to the transition from O$_2$ to O + O and have used this to obtain our initial guess for the R and S parameters of the Tersoff potential.
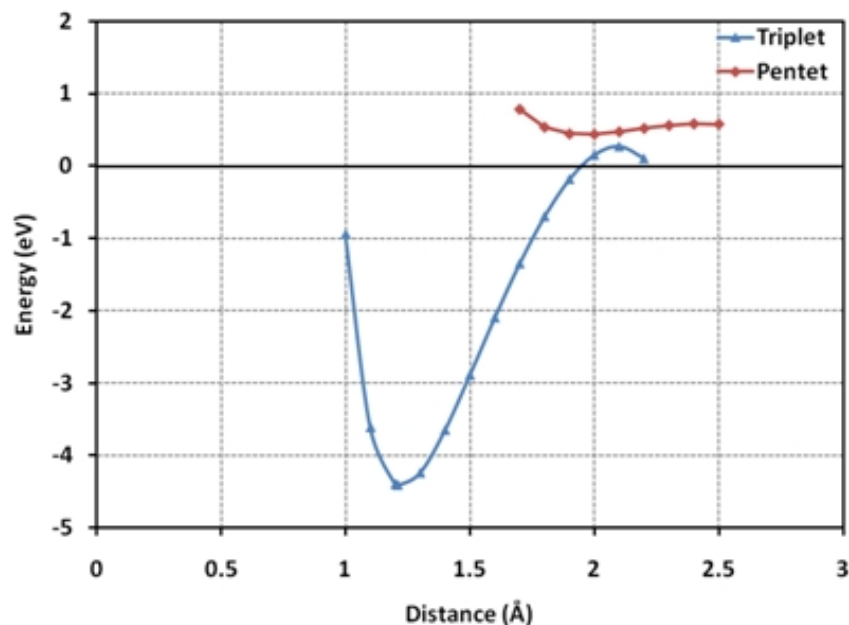
Figure 8.4: Parameters for the modified Tersoff potential with parameters C and D treated as linear functions of the two-body interatomic distance for O_3 database

The values of the elements of C and D obtained after a total of 10,000 training epochs using the Levenberg-Marquardt algorithm for one particular initial choice for the parameters are given in Table 8.2. Figure 8.5 (a) shows the potential contours resulting from the *ab initio* calculations as a function of r_{12} and r_{13}, where oxygen atom 1 is the apex atom in O_3, at a fixed O-O-O angle of 117.6°. Figure 8.5 (b) is the corresponding result from the fitted Tersoff potential. The essential features of the surface are correctly represented by the empirical potential.

A more quantitative measure of the fitting accuracy may be obtained from the computed rms error at each of the 4,102 points in the database. The best result we obtained using different initial estimates of the fitting parameters is 0.2385 eV. Therefore, this represents the best fit possible using a Tersoff potential form for the O_3 system where C and D are assumed to be linear functions of the O-O distance involved in the two-body term. If more

of the parameters were made simultaneous functions of all the elements of $\vec{P}_k$ with a more elaborate NN employed to adjust the weights and biases, the results could probably be substantially improved.

Table 8.2: Parameters for the modified Tersoff potential with parameters C and D treated as linear functions of the two-body interatomic distance for $O_2 + O \rightleftharpoons O_3$ database

Parameter	Solution
W_1 (eV/Å)	-8.8021
W_2 (eV/Å)	927.6048
b_1 (eV)	27.9028
b_2 (eV)	-692.4939
λ (Å^{-1})	0.0979374
μ (Å^{-1})	2.5635396
β	1.15855 x 10^{-6}
n	17.1142
c	100002.1609
d	32.8627
h	13.1919
rms error (eV)	0.2385

8.4 Dissociation dynamics of Ozone

We have carried out MD calculations of O_3 dissociation rates to $O_2 + O$ on the fitted Tersoff potential. Decay curves at four different internal energies between 2.12 eV and 2.50 eV were computed. In each case, the internal energy was microcanonically distributed over the three vibrational modes of the molecule and 1000 MD trajectories were computed with
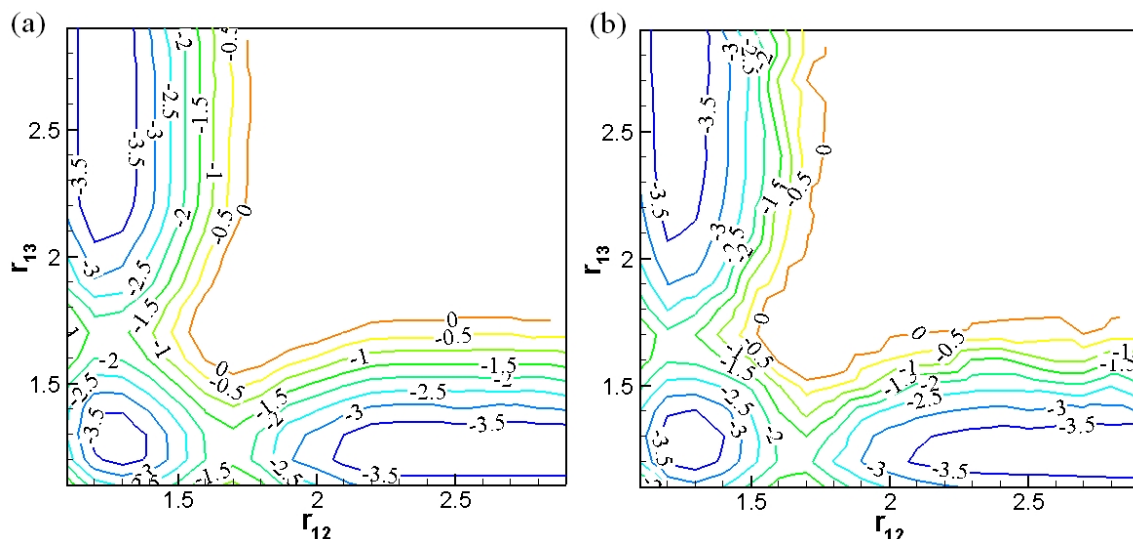
Figure 8.5: O_3 contour maps at an O-O-O angle of 117.6°, (a) *ab initio* data (b) fitted Tersoff potential

each trajectory being followed for 10 ps. Figure 8.6 shows a typical decay curve at an O_3 internal energy of 2.3695 eV. The line is a least-square fit to the trajectory data. As can be seen, the dissociation shows excellent first-order behavior, as expected. The dissociation rate coefficients are given by the negative slopes of the least-squares lines.

In a classical calculation, such as the MD methods, Rice, Ramsperger, and Kassel (RRK) theory [197] assumes that the dissociation rate of a molecule with internal energy E is proportional to the number of ways that the energy E can be distributed among the m internal vibrational modes of the molecule. This is subject to the constraint that the critical dissociation coordinate contains at least the minimum energy required for dissociation, E*. If all the internal vibrational modes freely exchange energy at a rate that is fast relative to the dissociation rate, then the dissociation rate coefficient at energy E, k(E), is given by:

$$k(E) = v \left[\frac{E - E*}{E} \right]^{m-1} \tag{8.23}$$

where v is constant and m is the number of vibrational modes present, 3n-6. If energy transfer between some vibrational modes is restricted or hindered, m will generally be

145
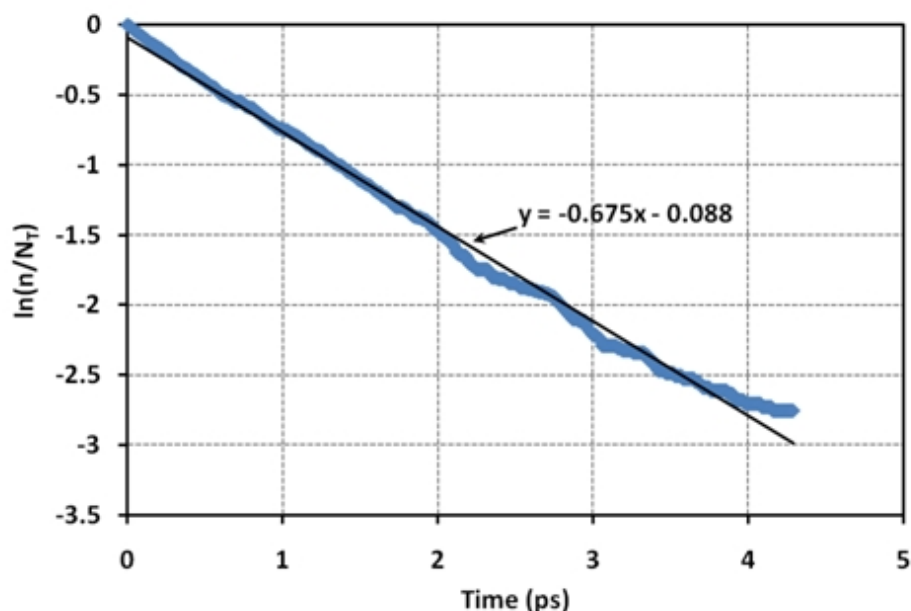
Figure 8.6: A typical decay curve at an O_3 internal energy of 2.3695 eV. The line is a least-square fit to the trajectory data. The slope of the line yields a dissociation rate coefficient of 0.675 ps^{-1}

found to be less than 3n-6.

Figure 8.7 shows such an RRK plot. We have assumed that E* is given by the barrier to O_3 dissociation on the fitted Tersoff potential. This barrier is 2.0312 eV. The linearity of the result is reasonably good. The slope of the least-squares line is 1.948 so that m = 2.948, which is very close to the theoretical value of 3 expected when all modes exchange energy rapidly and freely. When the molecule is a simple three-atom system, such as O_3, the vibrational modes are usually observed to exchange energy rapidly. The present result confirms that this is the case for O_3.

8.5   Conclusions

A generalized method that permits the parameters of an arbitrary empirical potential to be efficiently and accurately fitted to a database has been presented. The method permits
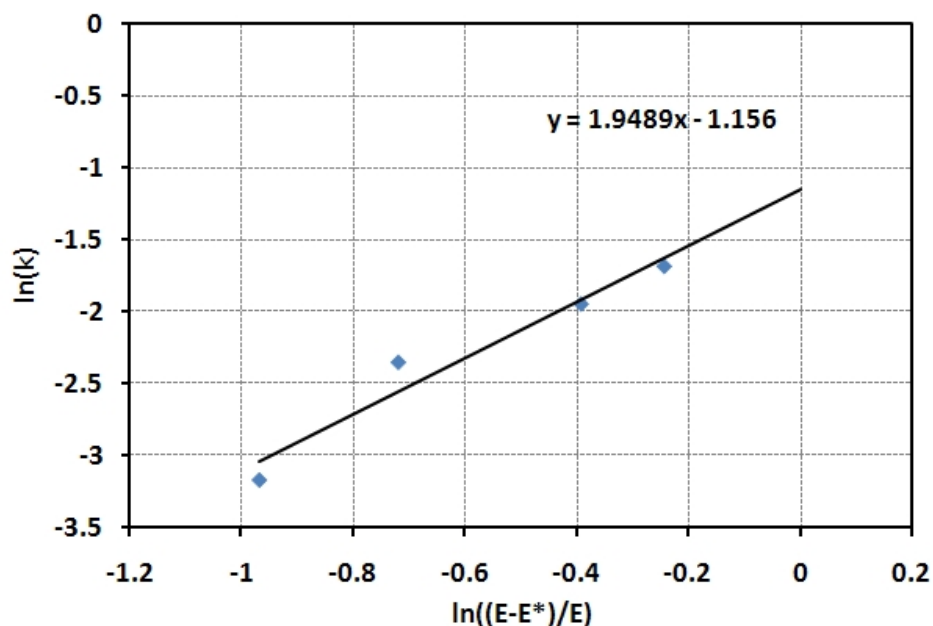
Figure 8.7: RRK plot for O_3 decomposition ($O_3 \rightleftharpoons O_2 + O$), E* = 2.0312 eV, the slope of least-squares line suggests that all the O_3 vibrational modes are exchanging energy rapidly relative to the unimolecular dissociation rate

the values of an arbitrary subset of the potential parameters to be considered as general functions of the internal coordinates that define the instantaneous configuration of the system. The parameters in this subset are computed by a generalized NN with an input vector containing at least 3n-6 elements, where n is the number of atoms in the system. Therefore, the method minimizes the fitting error not only with respect to the values of the constant parameters but also with respect to the functional form of the dependence of this subset of parameters upon the configuration of the system being fitted. This is the case since Hornik *et al.* [198] have shown that two-layer NNs with sigmoid transfer functions in the first hidden layer and linear functions in the output layer are universal approximators for analytic functions. Whatever the optimum functional forms are for the dependence of the parameters upon the system configuration, the NN will find them.

The Levenberg-Marquardt algorithm is employed to efficiently effect the optimization

of the weights and biases of the NN as well as all other potential parameters being treated as constants rather than as functions of the input coordinates. In order to effect this minimization, the usual Jacobian employed in NN operations is modified to include the Jacobian of the computed errors with respect to the parameters of the potential function. The total Jacobian employed in each epoch of minimization is the concatenation of the two Jacobians.

About 800 training epochs are required to converge the NN to the Si_5 database. The rms fitting error averaged over all 10,202 points in the database is found to vary from 0.0148 eV to 0.0153 eV depending upon the initial guesses made for the parameters. This favorable result is achieved because the Tersoff potential is well-suited for fitting the Si_5 database. In cases where the empirical surface is not well-judged, fitting accuracy will be reduced. The present method cannot convert a poorly devised empirical surface into a good one. It can, however, determine something close to the best possible fit even in cases with some or all of the parameters that are made complex functions of the configuration of the system.

An illustration of the above point is seen when the same Tersoff potential described in Section 8.3 is fitted to a database that samples configuration points on the potential surface for the non-adiabatic reaction $O_3 \rightleftharpoons O_2 + O$, where both reactants and products are in their electronic ground states. When the database comprises the lower of the singlet and pentet energies resulting from *ab initio* $UMP_4(SDQ)$ calculations with a 6-31G** basis set at 4,102 configuration points for this reaction, the rms error for the best fit of a Tersoff potential is 0.2385 eV. The fitting method locates something close to the best fit, but the functional form assumed for the fitting potential precludes a more accurate fit.

The power of the present method derives from three considerations-

First, it obviates the problem of selecting the form of the functional dependence of the parameters upon the system's coordinates by employing a neural network. If this network contains a sufficient number of neurons, it will automatically find something close to the

best functional form.

Second, the entire fitting procedure is automated so that excellent fits are obtained rapidly with a minimum of human effort.

Third, the neural network method provides a procedure to avoid local minima in the multi-dimensional parameter hyperspace. The Si_5 and $O_3 \rightleftharpoons O_2 + O$ systems are just a simple illustration of the technique. The real advantages will be realized when the method is applied to much more demanding systems.

CHAPTER 9

DEVELOPMENT OF GENERALIZED POTENTIAL ENERGY SURFACE (GPES)

9.1 Introduction

Molecular dynamics (MD) simulations have been playing an increasingly important role in the fundamental understanding of the material response at the atomistic level that is difficult to obtain from experiments. One such example is wear of diamond in the machining of iron. The mechanism behind this wear is graphitization of diamond in the presence of iron under the conditions of cutting(Chapter 5). This mechanism operates in the time frame of pico to nano seconds which is difficult to capture with the currently existing experimental techniques.

Central to the atomistic simulations is the interatomic potential, the accuracy of which determines the quality of the results and the complexity determines the computational load. A wide range of interaction potentials have been developed from pair-wise potentials [36, 37], embedded atom method (EAM) potential [43, 44] modified embedded atom method (MEAM) for metals [45] to potentials based on the bond order formalization for covalent bonded systems (e.g. Brenner [42] and Tersoff [38–40] potentials), to potentials based on first principles electronic structure calculations [159]. In this chapter, we present a generalized method for the development of potential-energy hyper surfaces using many-

body expansions, moiety energy (ME) approximation, and neural networks (NN). The following method has been jointly developed with my colleague Mr. Milind Malshe, who will also report these findings in his dissertation. These results have been jointly published in the J. Chem. Phys.[§]

A potential can be defined as a sum of two-body, three-body, and many-body interaction terms as given below:

$$V = \sum_{j>i} f_{rij} + \sum_{j,k>i} f_{\theta ijk} + \sum_{j,k,l>i} f_{\varphi ijkl} + \cdots + \sum_{j,k,l,\ldots,m>i} f_{\phi ijkl\ldots m} \qquad (9.1)$$

Depending on the complexity of a problem, one can decide on the number of many-body terms needed to characterize the system accurately. For example, a 2-body potential may be sufficient to represent interaction between two hydrogen atoms in a molecule (H_2). But the pair potential will inadequately represent a more complex structure, such as diamond. The selection of the number of many-body terms, in order to represent a potential accurately, is completely dependent on the user.

Such many-body expansions have been frequently employed to develop empirical potential surfaces. For example, the Tersoff potential [38–40] has been frequently employed to represent the potential force field for covalently bonded, non-metallic systems. This potential truncates the above expansion after the three-body term. The Brenner potential [42] for hydrocarbon systems is also a many-body expansion that include only the two- and three-body terms. Bolding and Anderson [199] have used such an expansion for Si_nH_m systems including one four-body term. All of these empirical potentials employ parameterized functional forms for the various terms in the expansion. In general, the parameters contained in the functional forms for the various terms are obtained by fitting the expansion to some database of experimental data, configuration energies obtained from electronic

[§]M. Malshe, **R. Narulkar**, L. M. Raff, M. Hagan, S. Bukkapatnam, P. M. Agrawal, and R. Komanduri, "Development of Generalized Potential Energy Surface (GPES) using many body terms, Neural Network (NN), and Moiety Energy (ME) Approximation," J. Chem. Phys. Vol. 130, (2009) pp. 184102/1-9

structure calculations, or both. Since the functional forms used in the expansion are arbitrary, they automatically limit the fitting and interpolation accuracy of the expansion.

In this chapter, a potential method to develop a generalized potential that can be applied to various categories of crystal structures, elements, and thier alloys is presented. This can be achieved by substituting neural networks for each of the m body-terms. The prime advantage of using neural networks is that it avoids presumption of the functional form *a priori*. In other words, neural network can take any shape thus providing the required flexibility needed to represent a complex potential surface.

As an illustration of the method, three examples are considered. First example contains two cases, case (i) for Si_5 system, case (ii) for multi-cluster system with Si_3, Si_4, and Si_5, and case (iii) for multi-cluster system with Si_3, Si_4, ..., Si_7 clusters elaborated to explain the selection of many-body terms. The second example is for vinyl bromide (C_2H_3Br) and all products for dissociation into six open reaction channels (12 if the reverse reactions are counted as separate open channels) that include C-H and C-Br bond scissions, three-center HBr dissociation, and three-center H_2 dissociation. The third example contains iron-carbon clusters, such as FeC, FeC_2, FeC_3, FeC_4, and Fe_3C.

9.2 Illustration of the method for fitting *ab initio* energies of silicon clusters

9.2.1 Si_5 clusters

In a cluster of m atoms, there are $^mC_2$ 2-body, $^mC_3$ 3-body, ..., and ^mC_m m-body terms, where

$$^mC_k = \frac{m!}{(m-k)!k!} \tag{9.2}$$

In the fitting of Si_5 clusters, we first include only two-body and three-body terms. The sufficiency of the interactions terms considered will be reflected by the fitting error of

the expansion to the database. If the error is too high, higher-order many-body terms are needed. There are ten two-body and ten three-body terms in Si$_5$ clusters. For a five-
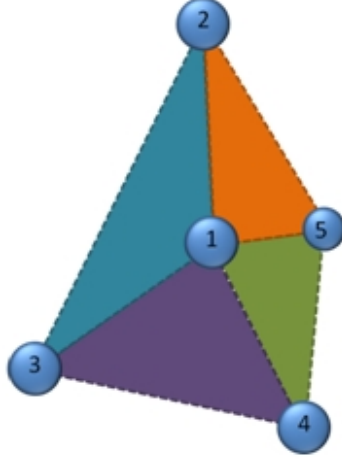
Figure 9.1: A 5-atom silicon cluster showing 3-body term by a unique colored triangle (i=1)

atom cluster, the 10 two-body distances and 10 three-body terms are represented with the following notation:

$$r_{ij} = \{r_{12}, r_{13}, \ldots, r_{45}\} \tag{9.3}$$

$$\theta_{ijk} = \{\theta_{123}, \theta_{13}, \ldots, \theta_{345}\} \tag{9.4}$$

Thus, the potential through three-body interactions can be represented as summation of 2- and 3-body terms which can be represented by equations as follows

$$f_r = \sum_{j>i} f_r(r_{ij}) \tag{9.5}$$

$$f_\theta = \sum_{j>i,k>i,j} f_\theta(r_{ij}, r_{ik}, r_{jk}) \tag{9.6}$$

The terms f_r and f_θ are each represented by a two-layer NN whose weights and biases are obtained iteratively using the Levenberg-Marquardt optimization algorithm [195]. This iterative procedure is illustrated in Figure 9.2.
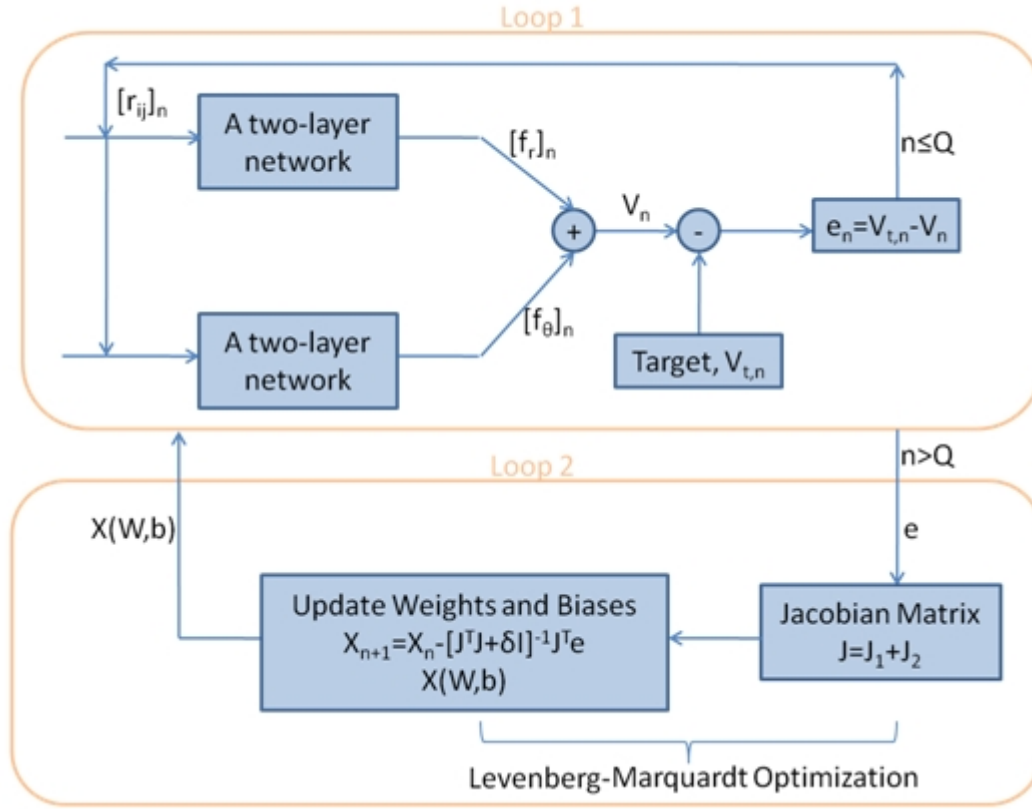
Figure 9.2: Flowchart for the development of generalized potential functions using neural networks [200]

In general, the Jacobian matrix, J, required by the Levenberg-Marquardt algorithm to fit a database containing Q data points when the many-body expansion is continued through the m-body terms will contain Q rows and $\{[3S_2 + 1] + [5S_3 + 1] ... + [(3m-4)S_m +1]\}$ columns, where S_k is the number of neurons in the first hidden layer of the NN for the k-body term. The elements of J all have the form $[\partial e_n/\partial w_{ij}^k]$ or $[\partial e_n/\partial b_j^k]$, where e_n represents the interpolation error of the potential for the nth data point, w_{ij}^k is the NN weight connecting the jth input to the ith neuron of the kth layer of network, and b_j^k is the bias for the ith neuron of the kth layer of the network. These derivatives can be computed using the Jacobian back propagation algorithm [195].

In this application, we have employed a (1-25-1) NN for the two-body term and a (3-

25-1) NN for the three-body term. However, this choice is arbitrary. If required, larger networks can be easily employed. In both networks, logsigmoid-linear transfer functions were used. In the fitting, a total of 10,202 five-atom silicon configurations were considered. The target values (*ab initio* energies) were produced by using a density functional theory (DFT) method with a 6-31G** basis set and the B3LYP procedure for incorporating correlation energy. The 10,202 Si_5 configurations were obtained from MD simulations of nanometric cutting of a silicon workpiece using a single-point cutting tool and sampling configurations within a 3 Å cutoff radius in front of and immediately below the cutting tool [75]. With these choices, the Jacobian required by the training algorithm contains 10,202 rows and 202 columns. A general Jacobain is given as:

$$
J = \begin{bmatrix}
\partial e_1/\partial W_1^1 & \partial e_1/\partial W_2^1 & \dots & \partial e_1/\partial b_1^1 & \dots & \partial e_1/\partial b_2^1 \\
\partial e_2/\partial W_1^1 & \partial e_2/\partial W_2^1 & \dots & \partial e_2/\partial b_1^1 & \dots & \partial e_2/\partial b_2^1 \\
\vdots & \vdots & \ddots & \vdots & \ddots & \vdots \\
\partial e_Q/\partial W_1^1 & \partial e_Q/\partial W_2^1 & \dots & \partial e_Q/\partial b_1^1 & \dots & \partial e_Q/\partial b_2^1
\end{bmatrix}_{Q \times [(3S_1+1)+(5S_2+1)]}
\tag{9.7}
$$

A root-mean-squared error of $8.143e^{-4}$ eV was obtained for the fitting with mean absolute error of $5.693e^{-4}$ eV. This fitting accuracy, which corresponds to 4.6 cm^{-1} or 0.055 kJ mol^{-1}, is the best thus far reported for a system of this complexity with such an extensive database. Clearly, there is no need to include four-body or higher terms for this Si_5 system.

9.2.2 Si_n (n=3, 4, 5) clusters

The general method, similarly, can be easily extended to a multi-cluster system. Here, we demonstrate the method for Si_3, Si_4, and Si_5 clusters. The procedure for training the network described above for the Si_5 system is repeated, but the database now includes energies of three-, four-, and five-atom silicon clusters observed in the MD cutting simulations [75]. This database comprises 300 Si_3, 260 Si_4, and 500 Si_5 configurations giving
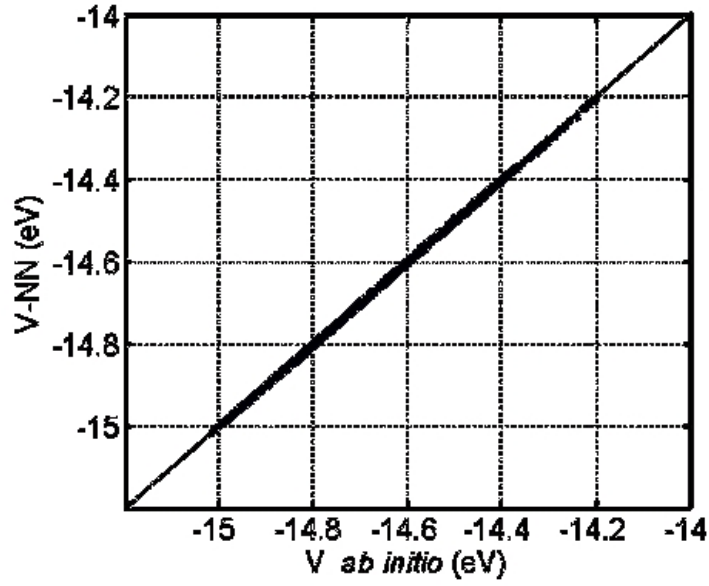
Figure 9.3: Comparison of GPES using NN with *ab initio* energies for Si_5 clusters [200]

us a total of 1060 configurations. Since the number of Si_3 and Si_4 clusters observed in the cutting experiments is much less than the number of Si_5 configurations, we have randomly selected 500 Si_5 configurations so that the total number of configurations for each type of cluster is roughly the same. If this is not done, the fitting will be dominated by the Si_5 data. We also have an additional 597 configurations that we employ as a testing set to evaluate the interpolation accuracy of the final fit. With this training database, one iteration cycle of the training is illustrated in Figure 9.2 requires about 10 minutes of CPU time on a PC with a clock speed of 2.6 GHz. A total of 860 iterations were required to obtain convergence of the weights and biases of the NN's.

The electronic structure calculations employed to obtain the energies of these configurations is the same as that used for the Si_5 clusters. For the training set, a root-mean-squared error of 0.0338 eV was obtained for the fitting with mean absolute error of 0.0192 eV. For the testing set, the rms error is 0.0437 eV and the mean absolute error is 0.0249 eV. Examination of the results for each type of cluster shows that the fitting error is relatively higher

156

for Si_4 clusters than for either Si_3 or Si_5. If it is judged that a fitting error with an rms deviation of 0.0437 eV is too large, the results can be further improved by simply adding higher m-body terms.
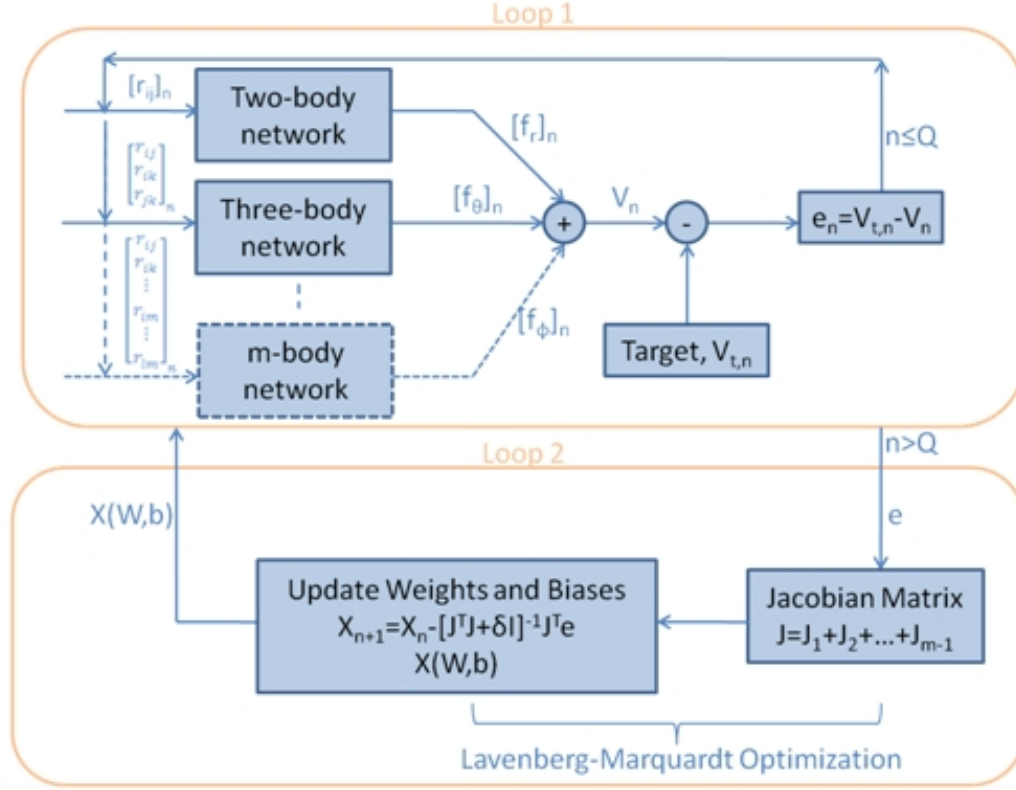
Figure 9.4: Flow chart for a generalized potential energy surface (GPES) for silicon clusters (m=4) [200]

As an illustration, we have added the four-body terms in the expansion. The resulting iterative procedure to fit the potential is shown in Figure 9.4 with an additional NN added in series to compute the four-body terms. We have employed a (6-25-1) NN for these terms. We have incorporated only 4-body terms. This incorporation increased the size of Jacobian matrix to $Q \times [(3S_1 + 1) + (5S_2 + 1) + (8S_3 + 1)]$ and added term f_φ in the potential.

With this choice and the database previously described, the Jacobian matrix required for the fitting contains 1060 rows and 403 columns. For the training set, the resulting
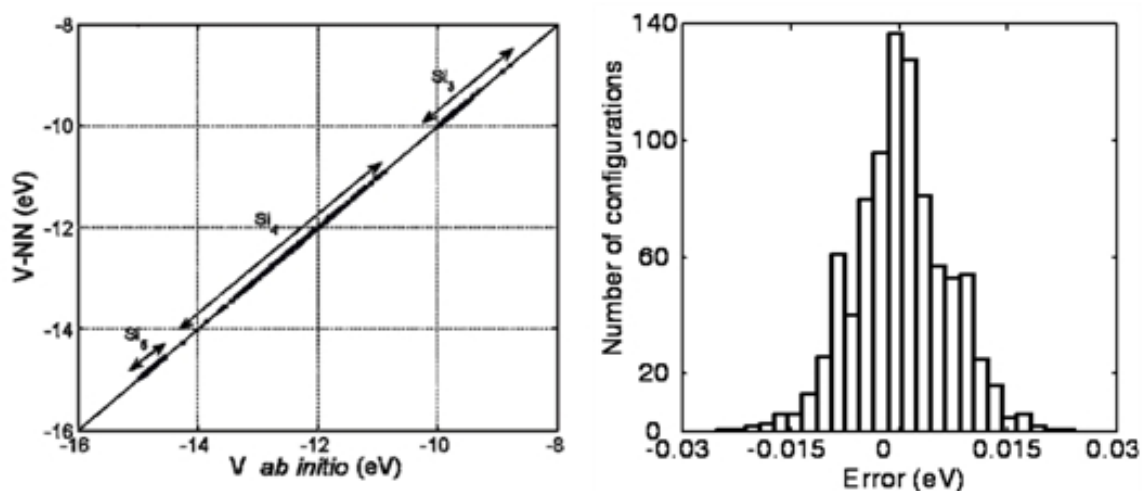
Figure 9.5: (a) Comparison of GPES with *ab initio* energies, (b) distribution of errors for the testing set for Si_3, Si_4, and Si_5 with four-body term included [200]

rms error is 0.0038 eV, and the mean absolute error is 0.0030 eV. For the testing set, the rms interpolation error is 0.0076 eV and the mean absolute error is 0.0056 eV. Thus, the inclusion of four-body terms in the potential reduces the rms error for the testing set by a factor of 5.8 and the mean absolute error by a factor of 4.4. The mean absolute error for the testing set corresponds to 0.54 kJ mol^{-1} or 45 cm^{-1}. As such, it is one of the most accurately fitted empirical potentials thus far reported in the literature. The fitting is compared in Figure 9.5 (a). The distribution of fitting errors for Si_3, Si_4, and Si_5 is shown in Figure 9.5 (b).

9.2.3 Si$_n$ (n=3, 4, ..., 7) clusters

The silicon clusters occurring in the MD simulations of silicon machining [75] also include Si_6 and Si_7 clusters for a cutoff radius of 3.0 Å. The many-body expansion/NN/ME method can easily be extended to include such clusters. The number of Si$_n$ clusters for the various values of n used in the training set for the NNs are given in Table 9.1.

Table 9.1: Number of configuration for Si_n clusters

Cluster size	Number of configurations
3	300
4	260
5	500
6	360
7	117
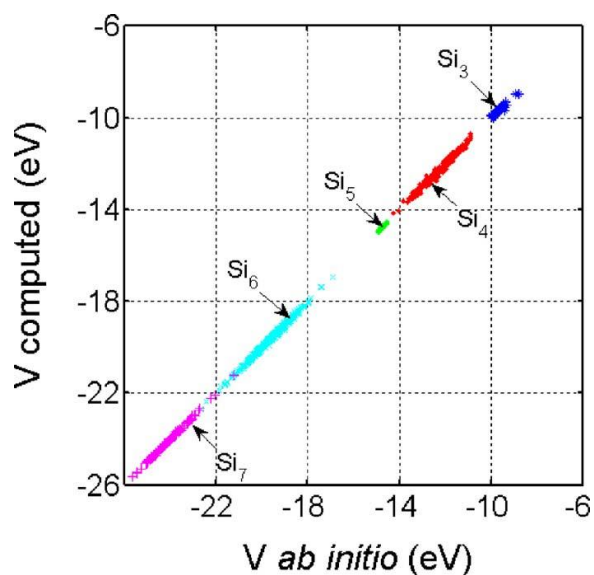
Figure 9.6: Comparison of GPES with *ab initio* energies for multiple silicon clusters [200]

The *ab initio* electronic structure calculations for these cluster congurations were performed in the same manner as previously described for the Si_3, Si_4, and Si_5 clusters. We have examined the effect of network conguration upon the average testing set error by fitting the above data-base with three different NN congurations each having 403-468 total weight and bias parameters. In each case, overfitting is avoided by use of a validation set. The mean absolute errors for the testing set varied from a low of 0.0212 eV for calculation

3 to 0.0353 eV for calculation 1. Since the conguration space spanned by the Si_n (n = 3, 4, ..., 7) clusters is about 17 eV, these errors correspond to percent errors of 0.12% and 0.21%, respectively. The fitting is shown in Figure 9.6.

9.3 *Ab initio* energies of vinyl bromide (C_2H_3Br) clusters and all products for dissociation into six open reaction channels

To investigate the vinyl bromide system and its dissociation products into six energetically open reaction channels (12 if the back reactions are counted as separate channels) is one of the most demanding systems yet to be addressed using *ab initio* methods to obtain the database and a generalized interpolation method to obtain the potential-energy surface from that database. The difficulty arises because there are six atoms present that include C, H, and Br atoms and also because there exist six energetically open reaction channels at 6.44 eV of internal energy. Because all six atoms are involved, the reaction mechanisms for the three-center dissociation channels and the total volume of configuration space of importance in the reaction dynamics is very large. This is seen by the fact that previous investigations [201] have shown that nearly 72,000 configuration points must be included in the database to obtain convergence of the potential-energy surface for the system.

Malshe *et al.* [201] obtained the *ab initio* potential-energy for this system using trajectory and novelty sampling methods to sample the configuration space of the system and UMP4(SDQ) methods to compute the energies of the 71,969 configurations thus obtained. These points were fitted using a single, six-body (15-140-1) NN. The reported interpolation error of this NN fit for the testing set was a mean absolute error of 0.065 eV. The configuration space of the system spans an energy range of about 7.5 eV and this error corresponds to an average absolute percent error of about 0.87%.

Here, we explore the possibility of using the many-body expansion/NN/ME method to fit the database for the vinyl bromide system. There are five non-equivalent two-body sets,

six non-equivalent three-body sets, and five non-equivalent four-body sets in vinyl bromide. Therefore, the general method illustrated in Figure 9.4 requires a corresponding number of NNs to be employed in the two-, three-, and four-body summations of the expansion for a total of 16. Without the use of ME approximation, this number would be 50. Using novelty sampling methods [159], we have selected the energies for 45,000 configurations as our training set. The remaining 26,969 points in the database are divided equally and randomly between the validation and testing sets.

9.4   Iron-Carbon clusters

To further understand the chemistry between iron and carbon, a robust potential is required to capture the chemical aspects based on quantum calculations. To develop a potential for iron-carbon system, different sizes of clusters were considered. These clusters are shown in the Figure 9.7. In this application, we have employed a (1-5-1) NN for the
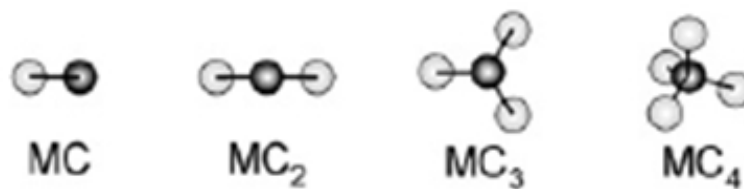
Figure 9.7: Structures of iron-carbon clusters [151]

two-body terms representing Fe-C and C-C interactions and a (3-15-1) NN for the three-body term representing C-C-C and Fe-C-C interactions. These networks constitute a total of 184 parameters. However, this choice is arbitrary. If required, larger networks can be easily employed. In both networks, log sigmoid-linear transfer functions were used. In the training, a total of 5,304 iron-carbon configurations were considered spanning over a range of 20 eV. Table 9.2 provides more details on the types of cluster used. The target values (*ab initio* energies) were produced by using a density functional theory (DFT) method with a 6-31G** basis set and the B3LYP procedure for incorporating correlation energy.

Table 9.2: Distribution of cluster types and training and fitting errors for iron-carbon clusters

Cluster type	Training	Testing
FeC	-	57
FeC$_2$	1394	441
FeC$_3$	2644	1528
FeC$_4$	1236	405
RMSE (eV)	0.157	0.215
% error	0.715	0.976
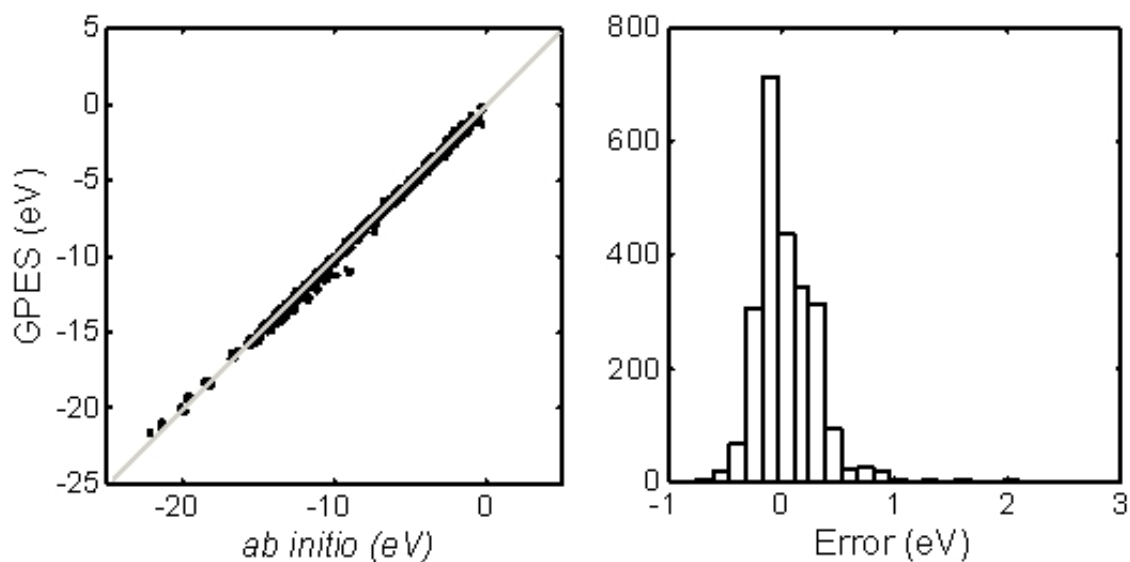
Figure 9.8: (a) Comparison of generalized potential energies using NN with *ab initio* energies, (b) distribution of errors for the testing set with upto three-body terms included for iron-carbon clusters

9.5 Advantages of the GPES method

The rms error obtained in the fitting of Si$_5$ structure is 8.143×10^{-4} eV or 6.6 cm^{-1}. This error is within the UV spectroscopic accuracy. Hence, the method has the ability to

produce high accuracy for a ten-dimensional surface.

The prime advantage of this method is that it is not limited by a fixed functional form. Once the system is trained, the potential parameters are easily transferable. Due to the simplistic analytical form of the transfer functions, the programming involved for running the MD trajectories is fairly simple and computational times are low.

The method can be expanded to multiple clusters so as to permit the treatment of bulk properties. This can be achieved by introducing periodic boundary conditions (PBC) during the *ab initio* calculations. Because of its ability to handle multi-dimensional, complex surfaces, this method can be extended not only to different crystal structures, such as BCC or FCC but also to various compounds, such as Fe_3C. For example, modified embedded atom method (MEAM) potential is represented as following:

$$E_{tot} = \frac{1}{2}\sum_{ij}V(r_{ij}) + \sum_{i}F(\rho_i), \tag{9.8}$$

Each of the two functions, $V(r_{ij})$ and $F(\rho_i)$, can be represented by two neural networks (one for each function) acting in series. The output of these networks can be summed to calculate the potential energy of the system.

As the system increases in complexity, additional, higher-order many-body terms can be added conveniently. This advantage is achieved by adding additional neural networks in series, each corresponding to different multi-body terms. Moreover, this potential can be extended not only to study covalent systems, but also to investigate ionic or long range coulombic potential. The idea can be based upon existing potentials, except each part of the potential can be replaced with a neural network.

The functional form is m-times differentiable, thus providing continuous first and second derivatives, which are used in the calculations of MD trajectories and frequencies. Because of the simple analytical form of the network transfer functions, the analytical forces are easy to compute.

CHAPTER 10

CONCLUSIONS

10.1 Diffusion couple tests

In diffusion couple tests, diffusion of carbon into iron was observed only when a diamond-graphite interlayer was added to diamond but not when diamond was used alone. This result provides corroborating evidence supporting the experimental results of machining [8–10, 13, 15, 16] observed previously that diamond initially graphitizes and subsequently diffuses into iron resulting in rapid diamond tool wear.

Diffusion depth increases with increasing temperature (see Table 4.2). Concentration of carbon atoms in iron increases with increasing temperature. At a particular temperature, the concentration of carbon atoms diffused into iron would reach a saturation value with respect to time as steady-state conditions.

10.2 Machining tests

MD simulations of nanometric cutting of pure iron with a diamond tool convincingly showed initial graphitization of diamond and subsequent formation of iron carbide as the mechanism of wear of diamond in the machining of iron. Consequently, these results are in concurrence with the experimental results of Komanduri and Shaw [8, 9] and the mechanism proposed by Ikawa and Tanaka [10].

164

Graphitization takes place not atom-by-atom but simultaneously by groups of atoms via an intermediate activated state [Figure 5.5(b)], which is in agreement with the mechanism proposed by Bovenkerk *et al.* [14] for diamond synthesis. It was observed that the diamond (100) plane is most resistant and the (011) plane is least resistant to graphitization with (111) in between. This observation is in agreement with the results of Seal [102].

A direct transition from sp^3 bonding to sp^2 bonding is observed instead of a two stage transition where carbon atoms sublime and condense into graphitic structure, as proposed by Davies and Evans [104]. This is also in agreement with Nath's theoretical model [107] and DeVita's *ab initio* investigation [114].

Dependence of the crystallographic orientation on wear of diamond has been investigated using MD simulations. We observed that wear pattern strongly differs due to changes in the crystal orientations. We conclude that wear not only depends on the crystallographic plane but also on the direction of the cutting because along the cutting edge there is intimate contact between cutting tool and the workpiece.

We also conclude that the 'hard' direction in diamond polishing for a particular plane can be used as 'hard' cutting edge for diamond tool in order to minimize wear of the tool. Plane (111) with $<11\bar{2}>$ cutting edge shows maximum wear. In other words, diamond polishing can be done efficiently on plane (111) along $<11\bar{2}>$ direction. We found that the (100) plane with the $<101>$ as cutting edge to show minimum wear. This combination is appropriate for machining with minimum wear on the cutting tool (diamond).

We report an intermediate path of transformation that takes place prior to the formation of carbide and subsequent cause of wear of diamond in the machining/grinding of iron. High temperature and intimate contact between diamond and iron not only transform diamond into graphite but also transform iron into hexagonal structure. This is because high pressure is generated due to the presence of ample amount of carbon around the octahedral

sites of iron. This causes iron (BCC) to transform into hexagonal phase. This transformation provides a path that is favorable energetically and geometrically for chemical reaction of carbon with iron to form iron carbide (Fe_3C).

Diamond graphitizes in the presence of iron. Plane (100) is most resistant to graphitization, and plane (111) graphitizes at all elevated temperatures. The temperature at which diamond graphitizes is lowered in the presence of iron. Anisotropy was observed in the graphitization.

Hexagonal iron was observed at the interface between iron and diamond. The transformation of BCC iron to HCP iron plays an important role in the graphitization of diamond. This path is favorable energetically and geometrically for the subsequent diffusion of carbon into iron, or actual formation of chemical reaction to form iron carbide (Fe_3C).

10.3   Development of GPES

A generalized method that permits the parameters of an arbitrary empirical potential to be efficiently and accurately fitted to a database has been presented. The method permits the values of an arbitrary subset of the potential parameters to be considered as general functions of the internal coordinates that define the instantaneous configuration of the system. The parameters in this subset are computed by a generalized NN with an input vector containing at least 3n-6 elements, where n is the number of atoms in the system. Therefore, the method minimizes the fitting error not only with respect to the values of the constant parameters but also with respect to the functional form of the dependence of this subset of parameters upon the configuration of the system being fitted.

The Levenberg-Marquardt algorithm is employed to efficiently effect the optimization of the weights and biases of the NN as well as all other potential parameters being treated as constants rather than as functions of the input coordinates. In order to effect this minimiza-

tion, the usual Jacobian employed in NN operations is modified to include the Jacobian of the computed errors with respect to the parameters of the potential function. The total Jacobian employed in each epoch of minimization is the concatenation of the two Jacobians.

About 800 training epochs are required to converge the NN to the Si_5 database. The rms fitting error averaged over all 10,202 points in the database is found to vary from 0.0148 eV to 0.0153 eV depending upon the initial guesses made for the parameters. This favorable result is achieved because the Tersoff potential is well-suited for the fitting the Si_5 database. In cases where the empirical surface is not well-judged, fitting accuracy will be reduced. The present method cannot convert a poorly devised empirical surface into a good one. It can, however, determine something close to the best possible fit even in cases with some or all of the parameters that are made complex functions of the configuration of the system.

A new method is proposed here that allows the development of generalized potential surface energy (GPES) as a sum of many-body terms. This method can be applied to develop potential for any physical system.

CHAPTER 11

FUTURE WORK

Generalized potential energy surface (GPES), as described in Chapter 9, is a method that can be implemented for the development of potential energy surface (PES) to simulate the bulk, based on quantum calculations. Quantum calculations can be conducted on the system of interest using periodic boundary conditions. This will allow the user to get rid of the dangling bonds on the surface, thus simulating bulk material. *Ab initio* calculations can be conducted using quantum calculations software. The two sotware we have considered for this study are Gaussian [31] and SIESTA (Spanish Initiative for Electronic Simulations with Thousands of Atoms) [202].

Gaussian software has been used by our research group for more than 10 years. This software provides high level energy calculations when used with or without periodic boundary conditions (PBC). However, with PBC the software consumes considerable amount of memory and is computationally exhaustive even at lower basis set. This makes the computational time intractable. Siesta, on the other hand, provides faster computations based on density functional theory (DFT) but is less accurate than high level energy calculations of Gaussian. However, taking into consideration the time versus the accuracy, Siesta still provides an acceptable amount of accuracy within a reasonable amount of time.

Siesta [202] implements a self consistent DFT method using standard norm-conserving pseudopotentials [203, 204] and a flexible, numerical linear combination of atomic orbitals

(LCAO) basis set, which includes multiple-zeta and polarization orbitals. Exchange and correlation are treated with the local spin density (LDA/LSD) [205] or generalized gradient approximations (GGA) [206]. The basis functions and the electron density are projected on a real-space grid, in order to calculate the Hartree and exchange–correlation (XC) potentials and matrix elements. They have used a modified energy functional, whose minimization produces orthogonal wavefunctions and the same energy and density as the Kohn–Sham energy functional, without the need for an explicit orthogonalization. Additionally, they have used localized Wannier-like electron wavefunctions that allows the computation time and memory required to minimize the energy to also scale linearly with the size of the system.

11.1   Extending generalized potential energy to Diamond

Figure 11.1 shows an unit of cell of diamond under periodic boundary conditions. There are a total of 18 atoms in a diamond unit-cell. But to implement PBC, this number is reduced to 8 atoms.
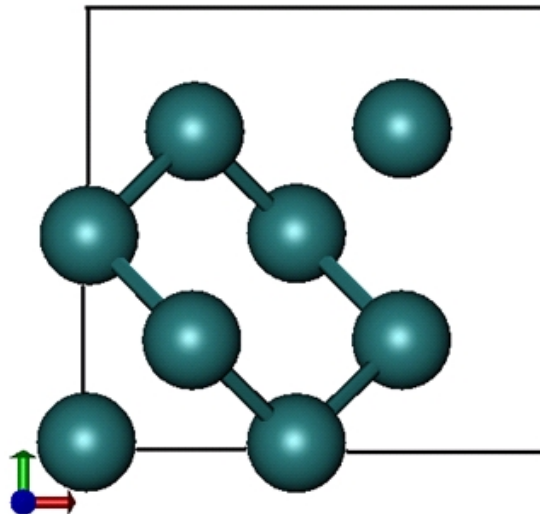
Figure 11.1: PBC model for an unit cell of diamond

Future work inculdes conducting quantum calculations using Siesta on the structure at different temperature ranges to cover a reasonable configuration space. The next step would be to employ GPES on the database and obtain a reasonable fitting. Once that is achieved, it will be able to conduct MD studies to simulate bulk material and thereby obtain the material properties.

BIBLIOGRAPHY

[1] R. Komanduri, "Cutting-Tool Materials," in *Encyclopedia of Chemical Technology*, p. 2027, Wiley, 1999.

[2] E. M. Trent and P. K. Wright, *Metal Cutting*. Butterworth-Heinemann Ltd, 4th ed., 2000.

[3] J. J. Gilman, "Why Silicon is Hard," *Science*, vol. 261, pp. 1436–1439, 1993.

[4] W. H. Bragg and W. L. Bragg, "The Structure of Diamond," *Proc. R. Soc. A*, vol. 89, no. 610, pp. 277–291, 1913.

[5] N. Ikawa, S. Shimada, and H. Morooka, "Technology of Diamond Tool for Ultra-precision Metal-Cutting," *Bull. Jap. Soc. Prec. Engrs.*, vol. 21, pp. 233–238, 1987.

[6] J. Wilks and E. M. Wilks, *Properties and Applications of Diamond*. London: Butterworth Heinemann, 1991.

[7] R. Komanduri and M. C. Shaw, "New Method of Nucleating Diamond," *Nature*, vol. 248, pp. 582–584, 1974.

[8] R. Komanduri and M. C. Shaw, "Wear of Synthetic Diamond When Grinding Ferrous Metals," *Nature*, vol. 255, pp. 211–213, 1975.

[9] R. Komanduri and M. C. Shaw, "On the Diffusion Wear of Diamond in Grinding Pure Iron," *Phil. Mag.*, vol. 34, no. 2, pp. 195–204, 1976.

[10] N. Ikawa and T. Tanaka, "Thermal Aspects of Wear of Diamond Grain in Grinding," *Annals of CIRP*, vol. 19, no. 1, pp. 153–157, 1971.

[11] F. S. Phinney, "Graphitization of Diamond," *Science*, vol. 120, no. 3114, pp. 393–394, 1954.

[12] Y. Gogotsi, A. Kailer, and K. G. Nickel, "Transformation of Diamond to Graphite," *Nature*, vol. 401, pp. 663–664, 1999.

[13] T. Tanaka and N. Ikawa, "Thermal Aspects of Wear of Diamond Abrasive Grain in Grinding Mild Steel," *Bull. Jap. Soc. Prec. Engrs.*, vol. 7, no. 4, p. 97, 1973.

[14] H. P. Bovenkerk, F. P. Bundy, H. T. Hall, H. M. Strong, and R. H. Wentorf, "Preparation of Diamond," *Nature*, vol. 184, pp. 1094–1098, 1959.

[15] A. G. Thornton and J. Wilks, "Clean Surface Reactions Between Diamond and Steel," *Nature*, vol. 274, pp. 792 – 793, 1978.

[16] A. G. Thornton and J. Wilks, "Tool Wear and Solid State Reactions During Machining," *Wear*, vol. 53, pp. 165–187, 1979.

[17] H. W. Kroto, J. R. Heath, S. C. O'Brien, R. F. Curl, and R. E. Smalley, "C60: Buckminsterfullerene," *Nature*, vol. 318, pp. 162–163, 1985.

[18] S. Iijima, "Helical Microtubules of Graphitic Carbon," *Nature*, vol. 56-58, 1991.

[19] Jacquelain *Ann. d. Chim. et Phys.*, vol. 20, p. 468, 1847.

[20] X. Wang, S. Scandolo, and R. Car, "Carbon Phase Diagram from *Ab initio* Molecular Dynamics," *Phys. Rev. Lett.*, vol. 95, no. 185701, pp. 1–4, 2005.

[21] J. E. Field, *The Properties of Diamond*. London, U.K.: Academic Press, 1979.

[22] E. Paul, C. Evans, A. Mangamelli, M. L. McGlauflin, and R. S. Polvani, "Chemical Aspects of Tool Wear in Single Point Diamond Turning," *Prec. Eng.*, vol. 18, pp. 4–19, 1996.

[23] Y. Q. Xie, "Electronic Structure and Properties of Pure Iron," *Acta Mat.*, vol. 42, no. 11, pp. 3705–3715, 1994.

[24] J. F. Berry, E. Bill, E. Bothe, S. D. SGeorge, B. Mienert, F. Neese, and K. Wieghardt, "An Octaheral Coordination Comple of Iron (VI)," *Science*, vol. 312, pp. 1937–1941, 2006.

[25] O. D. Sherby, J. Wadsworth, D. R. Lesuer, and C. K. Syn, "The c/a Ratio in Quenched Fe-C and Fe-N steels - a Heuristic Story," 2006.

[26] I. R. Shein, N. I. Medvedeva, and A. L. Ivanovskii, "Electronic and Structural Properties of Cementite-type M_3X (M = Fe, Co, Ni; X = C or B) by First Principles Calculations," *Physica B*, vol. 371, p. 126132, 2006.

[27] K. W. Andrews, "The Structure of Cementite and its Relation to Ferrite and Epsilon Carbide - ii," *Acta Meta.*, vol. 12, pp. 921–929, 1963.

[28] S. S. Iyengar, H. B. Schlegel, J. M. Millam, G. A. Voth, G. E. Scuseria, and M. J. Frisch, "*Ab initio* Molecular Dynamics: Propagating the Density Matrix with Gaussian Orbitals. ii. Generalizations Based on Mass-weighting, Idempotency, Energy Conservation and Choice of Initial Conditions," *J. Chem. Phys*, vol. 115, pp. 10291–302, 2001.

[29] H. B. Schlegel, J. M. Millam, S. S. Iyengar, G. A. Voth, G. E. Scuseria, A. D. Daniels, and M. J. Frisch, "*Ab Initio* Molecular Dynamics: Propagating the Density Matrix with Gaussian Orbitals," *J. Chem. Phys*, vol. 114, pp. 9758–63, 2001.

[30] H. B. Schlegel, S. S. Iyengar, X. Li, J. M. Millam, G. A. Voth, G. E. Scuseria, and M. J. Frisch, "*Ab Initio* Molecular Dynamics: Propagating the Density Matrix with Gaussian Orbitals III Comparison with Born-Oppenheimer Dynamics," *J. Chem. Phys*, vol. 117, pp. 8694–704, 2002.

[31] M. J. Frisch, G. W. Trucks, and H. B. Schlegel, "Gaussian 03," 2003.

[32] E. Neyts, *Mathematical Simulation of the Deposition of Diamond-like Carbon (DLC) Films*. PhD thesis, Universiteit Antwerpen, 2006.

[33] B. J. Alder and T. E. Wainwright, "Phase Transition for a Hard-sphere System," *J. Chem. Phys.*, vol. 27, pp. 1208–1209, 1957.

[34] B. J. Alder and T. E. Wainwright, "Studies in Molecular Dynamics. i. General Method," *J. Chem. Phys.*, vol. 31, pp. 459–66, 1959.

[35] B. J. Alder and T. E. Wainwright, "Studies in Molecular Dynamics. ii. Behavior of a Small Number of Elastic Spheres," *J. Chem. Phys.*, vol. 33, pp. 1439–51, 1960.

[36] P. M. Morse, "Diatomic Molecules According to the Wave Mechanics. ii. Vibrational Levels," *Phys. Rev.*, vol. 34, p. 57, 1929.

[37] J. E. Lennard-Jones, "On the Determination of Molecular Fields. ii. From the Equation of State of a Gas," *Proc. Royal Soc. Lon. A*, vol. 106, p. 463, 1924.

[38] J. Tersoff, "Empirical Interatomic Potential for Silicon with Improved Elastic Properties," *Phys. Rev. B*, vol. 38, no. 14, pp. 9902–9905, 1988.

[39] J. Tersoff, "Empirical Interatomic Potential for Carbon, with Application to Amorphous Carbon," *Phys. Rev. Lett.*, vol. 61, no. 25, pp. 2789–2882, 1988.

[40] J. Tersoff, "Modeling Solid-state Chemistry: Interatomic Potential for Multicomponent Systems," *Phys. Rev. B*, vol. 39, no. 8, pp. 5566–5568, 1989.

[41] D. W. Brenner, "Tersoff-type Potentials for Carbon, Hydrogen, and Oxygen," *Mat. Res. Soc. Symp. Proc.*, vol. 141, pp. 59–64, 1989.

[42] D. W. Brenner, "Empirical Potential for Hydrocarbons for use in Simulating the Chemical Vapor Deposition of Diamond Films," *Phys. Rev. B*, vol. 42, no. 15, pp. 9458–9471, 1990.

[43] M. S. Daw and M. I. Baskes, "Semiempirical, Quantum Mechanical Calculation of Hydrogen Embrittlement in Metals," *Phys. Rev. Lett.*, vol. 50, no. 17, pp. 1285–1288, 1983.

[44] M. S. Daw and M. I. Baskes, "Embedded-atom Method: Derivation and Application to Impurities, Surfaces, and Other Defects in Metals," *Phys. Rev. B*, vol. 29, no. 12, pp. 6443–6454, 1984.

[45] M. I. Baskes, "Modified Embedded-atom Potentials for Cubic Materials and Impurities," *Phys. Rev. B*, vol. 46, no. 5, pp. 2727–2742, 1992.

[46] P. M. Kroll. Ph.d, Technische Hochschule, 1996.

[47] G. Simonelli, R. Pasianot, and E. Savino, "Embedded-Atom-Method Interatomic Potentials for BCC-iron," in *Mat. Res. Soc. Symp. Proc.*, vol. 291, (Pittsburgh, PA), p. 567, 1993.

[48] M. Ruda, D. Farkas, and J. Abriata, "Interatomic Potentials for Carbon Interstitials in Metals and Intermetallics," *Scripta Materialia*, vol. 46, pp. 349–355, 2002.

[49] J. Häglund, G. Grimvall, and T. Jarlborg, "Electronic Structure, X-ray Photoemission Spectra, and Transport Properties of Fe_3C (Cementite)," *Phys. Rev. B*, vol. 44, no. 7, pp. 2914–2919, 1991.

[50] M. I. Baskes, "Atomistic Potentials for the Molybdenum-Silicon System," *Mat. Sci. and Eng. A*, vol. 261, no. 1-1, pp. 165–168, 1999.

[51] J. H. Rose, J. R. Smith, F. Guinea, and J. Ferrante, "Universal Features of the Equation of State of Metals," *Phys. Rev. B*, vol. 29, pp. 2963 – 2969, 1984.

[52] B. J. Lee and M. I. Baskes, "Second Nearest-Neighbor Modified Embedded-Atom-Method Potential," *Phys. Rev. B*, vol. 62, no. 13, pp. 8564–8567, 2000.

[53] B. J. Lee, M. I. Baskes, H. Kim, and Y. K. Cho, "Second Nearest-Neighbor Modified Embedded-Atom-Method Potentials for BCC Transition Metals," *Phys. Rev. B*, vol. 64, pp. 1–11, 2001.

[54] B. J. Lee and J. W. Lee, "A Modified Embedded-Atom-Method Interatomic Ppotential for Carbon," *Computer Coupling of Phase Diagrams and Thermochemistry*, vol. 29, pp. 7–16, 2005.

[55] B. J. Lee, "A Modified Embedded-Atom-Method Interatomic Potential for the Fe-C System," *Acta Mat.*, vol. 54, pp. 701–711, 2006.

[56] B. J. Lee, "A Modified Embedded-Atom-Method Interatomic Potential for the Fe-N System: A Comparative Study with the Fe-C System," *Acta Mat.*, vol. 54, pp. 4597–4607, 2006.

[57] S. J. Plimpton, "Fast Parallel Algorithms for Short-Range Molecular Dynamics," *J. Comp. Phys.*, vol. 117, pp. 1–19, 1995.

[58] J. Belak and I. F. Stowers, "A Molecular Dynamics Model of the Orthogonal Cutting Process," *Proc. ASPE Annual Conference*, p. 7679, 1990.

[59] J. Belak, D. A. Lucca, R. Komanduri, R. L. Rhorer, T. Moriwaki, K. Okuda, S. Ikawa, S. Shimada, H. Tanaka, T. A. Dow, J. D. Drescher, and I. F. Stowers, "Molecular Dynamics Simulation of the Chip Forming Process in Single Crystal Copper and Comparison with Experimental Data," *Proc. ASPE Annu. Conf.*, p. 100, 1991.

[60] N. Ikawa, S. Shimada, H. Tanaka, and G. Ohmori, "Atomistic Analysis of Nanomet-

ric Chip Removal as Affected by Tool-work Interaction in Diamond Turning," *CIRP Annals*, vol. 40, no. 1, pp. 551–554, 1991.

[61] S. Shimada, S. Ikawa, H. Tanaka, G. Ohmori, J. UchiKoshi, and H. Yoshinaga, "Feasibility Study on Ultimate Accuracy in Microcutting Using Molecular Dynamics Simulation," *Annals of CIRP*, vol. 42, no. 1, p. 91, 1993.

[62] S. Shimada, S. Ikawa, H. Tanaka, and J. UchiKoshi, "Structure of Micromachined Surface Simulated by Molecular Dynamics Analysis," *Annals of CIRP*, vol. 43, no. 1, p. 51, 1994.

[63] S. Shimada, "Molecular Dynamics Analysis of Nanometric Cutting Process," *Int. J. Jpn. Soc. Precis. Eng.*, vol. 29, no. 4, p. 283, 1995.

[64] T. Inamura, H. Suzuki, and N. Takezawa, "Cutting Experiments in a Computer Using Atomic Models of Copper Crystal and a Diamond Tool," *Int. J. Jpn. Soc. Precis. Eng.*, vol. 25, no. 4, p. 259, 1991.

[65] T. Inamura, N. Takezawa, and N. Taniguchi, "Atomic-scale Cutting in a Computer Using Crystal Models of Copper and Diamond," *Annals of CIRP*, vol. 41, no. 1, p. 121, 1992.

[66] T. Inamura, N. Takezawa, and Y. Kumaki, "Mechanics and Energy Dissipation in Nanoscale Cutting," *Annals of CIRP*, vol. 42, no. 1, pp. 79–82, 1993.

[67] T. Inamura, N. Takezawa, Y. Kumaki, and T. Sata, "On a Possible Mechanism of Shear Deformation in Nanoscale Cutting," *Annals of CIRP*, vol. 43, no. 1, p. 47, 1994.

[68] K. Maekawa and A. Itoh, "Friction and Tool Wear in Nano-scale Machining - A Molecular Dynamics Approach," *Wear*, vol. 188, no. 1-2, pp. 115–22, 1995.

[69] N. Chandrasekaran, A. Noori-Khajavi, L. M. Raff, and R. Komanduri, "A New Method for Molecular Dynamics Simulation of Nanometric Cutting," *Phil. Mag. B*, vol. 77, no. 1, p. 7, 1998.

[70] R. Komanduri, N. Chandrasekaran, and L. M. Raff, "Effect of Tool Geometry in Nanometric Cutting: A Molecular Dynamics Simulation Approach," *Wear*, vol. 219, pp. 84–97, 1998.

[71] R. Komanduri, N. Chandrasekaran, and L. M. Raff, "Some Aspects of Machining with Negative Rake Tools Simulating Grinding: A Molecular Dynamics Simulation Approach," *Phil. Mag. B*, vol. 79, no. 7, pp. 995–968, 1999.

[72] R. Komanduri, N. Chandrasekaran, and L. M. Raff, "Orientation Effects in Nanometric Cutting of Single Crystal Materials: An MD Simulation Approach," *Annals of CIRP*, vol. 48/1, pp. 67–72, 1999.

[73] R. Komanduri, N. Chandrasekaran, and L. M. Raff, "M.D. Simulation of Nanometric Cutting of Single Crystal Aluminum – Effect of Crystal Orientation and Direction of Cutting," *Wear*, vol. 242, pp. 60–88, 2000.

[74] R. Komanduri, N. Chandrasekaran, and L. M. Raff, "MD Simulation of Exit Failure in Nanometric Cutting," *Mat. Sci. and Eng. A*, vol. 311, pp. 1–12, 2001.

[75] R. Komanduri, N. Chandrasekaran, and L. M. Raff, "Molecular Dynamics Simulation of the Nanometric Cutting of Silicon," *Phil. Mag. B*, vol. 81, pp. 1989–2019, 2001.

[76] R. Komanduri, R. Narulkar, and L. M. Raff, "Monte Carlo Simulation of Nanometric Cutting," *Phil. Mag.*, vol. 84, no. 11, pp. 1155–1183, 2004.

[77] R. Komanduri and Z. B. Hou, "Thermal Modeling of the Metal Cutting Process – Part III: Temperature Rise Distribution Due to the Combined Effects of Shear

Plane Heat Source and the Tool-Chip Interface Frictional Heat Source," *International Journal of Mechanical Sciences*, vol. 43, pp. 89–107, 2001.

[78] R. Narulkar, L. M. Raff, and R. Komanduri, "Monte CarloSteepest Descent (MC-SD) Simulations of Nanometric Cutting," *J. Nanoengineering and Nanosystems*, vol. 218, no. Part N2, pp. 7–16, 2005.

[79] J. Belak, "Nanotribology: Modeling Atoms When Surfaces Collide," tech. rep., Lawrence Livermore Laboratory, 1994.

[80] M. D. Perry and J. A. Harrison, "Molecular Dynamics Investigations of the Effects of Debris Molecules on the Friction and Wear of Diamond," *Thin Solid Films*, vol. 290-291, pp. 211–215, 1996.

[81] L. Zhang and H. Tanaka, "Towards a Deeper Understanding of Wear and Friction on the Atomic Scale - A Molecular Dynamics Analysis," *Wear*, vol. 211, pp. 44–53, 1997.

[82] K. Cheng, X. Luo, R. Ward, and R. Holt, "Modeling and Simulation of the Tool Wear in Nanometric Cutting," *Wear*, vol. 255, pp. 1427–1432, 2003.

[83] F. P. Bundy, H. T. Hall, H. M. Strong, and R. H. Wentrorf Jr., "Man-made Diamond," *Nature*, vol. 176, pp. 51–54, 1955.

[84] P. S. DeCarli and J. C. Jamieson, "Formation of Diamond by Explosive Shock," *Science*, vol. 133, no. 3467, pp. 1821–1822, 1961.

[85] F. P. Bundy, "Direct Conversion of Graphite to Diamond in Static Pressure Apparatus," *Science*, vol. 137, no. 3535, pp. 1057–1058, 1962.

[86] L. F. Trueb, "An Electron-Microscope Study of Shock-Synthesized Diamond," *J. App. Phys.*, vol. 39, no. 10, pp. 4707–4716, 1968.

[87] F. P. Bundy and J. S. Kasper, "Hexagonal Diamond-A New Form of Carbon," *J. Chem. Phys.*, vol. 46, no. 9, pp. 3437–3446, 1966.

[88] T. Yagi, W. Utsumi, M. Yamakata, T. Kikegawa, and O. Shimomura, "High-pressure *In-Situ* X-ray-Diffraction Study of the Phase Transformation from Graphite to Hexagonal Diamond at Room Temperature," *Phys. Rev. B*, vol. 46, no. 10, pp. 6031–6039, 1992.

[89] H. He, T. Sekine, and T. Kobayashi, "Direct Transformation of Cubic Diamond to Hexagonal Diamond," *App. Phys. Lett.*, vol. 81, no. 4, pp. 610–612, 2002.

[90] T. Irifune, A. Kurio, S. Sakamoto, T. Inoue, and H. Sumiya, "Ultrahard Polycrystalline Diamond from Graphite," *Nature*, vol. 421, no. 6923, p. 599, 2003.

[91] H. Moissan *Ann. d. Chim. et Phys.*, vol. 7, no. 9, p. 133, 1896.

[92] R. Vogel and G. Tammann, "Ioppe-Seyler's Z. Physiol," *Chem.*, vol. 69, p. 598, 1910.

[93] G. Friedel and G. Ribaud, "A Transformation of Diamond," *Bull. Soc. Fran. Min.*, vol. 47, p. 94, 1924.

[94] P. W. Bridgman, "An Experimental Contribution to the Problem of Diamond Synthesis," *J. Chem. Phys.*, vol. 15, no. 2, pp. 92–98, 1947.

[95] H. J. Grenville-Wells *Miner. Mag.*, vol. 29, p. 803, 1952.

[96] H. J. Rodewald, "Die umwandlungswärmen der Phosphor-Modifikationen," *Helv. Chim. Acta*, vol. 43, p. 1657, 1960.

[97] M. Seal, "Graphitization and Plastic Deformation of Diamond," *Nature*, vol. 182, pp. 1264–1267, 1958.

[98] M. Seal, "Graphitization of Diamond," *Nature*, vol. 185, pp. 522–523, 1960.

[99] T. Evans and D. H. Sauter, "Etching of Diamond Surface with Gases," *Phil. Mag.*, vol. 6, no. 63, pp. 429–440, 1960.

[100] F. P. Bundy, H. P. Bovenkerk, H. M. Strong, and R. H. Wentorf, "Diamond-Graphite Equilibrium Line from Growth and Graphitization of Diamond," *J. Chem. Phys.*, vol. 35, no. 2, pp. 383–391, 1961.

[101] V. R. Howes, "The Graphitization of Diamond," *Proc. Phys. Soc*, vol. 80, p. 648, 1962.

[102] M. Seal, "The Effect of Surface Orientation on the Graphitization of Diamond," *Physica Status Solidi*, vol. 3, pp. 658–654, 1963.

[103] T. Evans and P. F. James, "A Study of the Transformation of Diamond to Graphite," *Proc. R. Soc. A*, vol. 277, no. 1369, pp. 260–269, 1964.

[104] G. Davies and T. Evans, "Graphitization of Diamond at Zero Pressure and at a High Pressure," *Proc. R. Soc. A*, vol. 328, pp. 413–427, 1972.

[105] A. Hu, I. Alkhesho, W. W. Duley, and H. Zhaou, "Cryogenic Graphitization of Submicrometer Grains Embedded in Nanostructured Tetrahedral Amorphous Carbon Films," *J. App. Phys.*, vol. 100, no. 084319, pp. 1–5, 2006.

[106] F. M. van Bouwelen, "Polishing: Mechanically Induced Degradation of Diamond," *Physica Status Solidi A*, vol. 172, pp. 91–96, 1999.

[107] N. S. N. Nath, "The Dynamical Theory of the Diamond Lattice Part iii. The Diamond-Graphite Transformation," *Proc. Indian Acad. Sci. A*, vol. 2, pp. 143–152, 1935.

[108] P. Badziag, W. S. Verwoerd, W. P. Ellis, and N. R. Greiner, "Nanometre-sized Diamonds are More Stable than Graphite," *Nature*, vol. 343, no. 6255, p. 244, 1990.

[109] S. E. Stein, "Diamond and Graphite Precursors," *Nature*, vol. 346, p. 517, 1990.

[110] M. Kitabatake, "Molecular Dynamics Simulations of Graphite→Diamond Transformation and SiC Growth on Si (001)," *Trans. Mat. Res. Soc. Jpn.*, vol. 14B, pp. 1493–1496, 1994.

[111] B. N. Davidson and W. E. Pickett, "Graphite-layer Formation at a Diamond (111) Surface Step," *Phys. Rev. B*, vol. 49, no. 20, p. 14770, 1994.

[112] G. Jungnickel, D. Porezag, T. Frauenheim, M. I. Heggie, W. R. L. Lambrecht, B. Segall, and J. C. Angus, "Graphitization Effects on Diamond Surfaces and the Diamond/Graphite Interface," *Physica Status Solidi A*, vol. 154, pp. 109–125, 1996.

[113] G. Jungnickel, T. Frauenheim, D. Porezag, W. R. L. Lambrecht, B. Segall, and J. C. Angus, "Mechanical Behaviour of Diamond and Other Forms of Carbon," in *Proc. Mater. Res. Soc. Symp.* (M. Droroy, D. Bogy, M. Donley, and J. E. Field, eds.), vol. 338, (Pittsburgh, PA), pp. 349–360, MRS, 1995.

[114] A. DeVita, G. Galli, A. Canning, and R. Car, "A Microscopic Model for Surface-induced Diamond to Graphite," *Nature*, vol. 379, pp. 523–526, 1996.

[115] D. Saada, J. Adler, and R. Kalish, "Computer Simulation of Damage in Diamond Due to Ion Impact and its Annealing," *Phys. Rev. B*, vol. 59, no. 10, pp. 6650–6660, 1999.

[116] A. Bródka, T. W. Zerda, and A. Burian, "Graphitization of Small Diamond Cluster - Molecular Dynamics Simulation," *Diamond Related Materials*, vol. 15, pp. 1818–1821, 2006.

[117] H. O. Jeschke, M. E. Garcia, and K. H. Bennemann, "Microscopic Analysis of the Laser-induced Femtosecond Graphitization of Diamond," *Phys. Rev. B*, vol. 60, pp. R3701–R3704, 1999.

[118] J. C. Angus, H. A. Will, and W. S. Stanko, "Growth of Diamond Seed Crystals by Vapor Deposition," *J. App. Phys.*, vol. 39, pp. 2915–2922, 1968.

[119] J. C. Angus, R. W. Hoffman, and P. H. Schmidt, "Studies of Amorphous Hydrogenated Diamond-like Hydrocarbons and Crystalline Diamond," 1988.

[120] M. Sunkara, J. C. Angus, C. C. Hayman, and F. A. Buck, "Nucleation of Diamond Crystals," *Carbon*, vol. 28, no. 6, pp. 745–746, 1990.

[121] J. C. Angus, A. Argoitia, R. Gat, Z. Li, M. Sunkara, L. Wang, and Y. Wang, "Chemical Vapour Deposition of Diamond," *Phil. Trans. R. Soc. Lond. A*, vol. 342, pp. 195–208, 1993.

[122] J. C. Angus, Z. Li, M. Sunkara, Y. Wang, M. Lee, and B. Segall, "Nucleation and Growth in the Chemical Vapor Deposition of Diamond," in *Proceedings of the Second International Conference on the Applications of Diamond Films and Related Materials* (O. Saitama, ed.), (Japan), p. 159, 1993.

[123] R. Komanduri and S. Nandyal, "Low Pressure Synthsis of Polycrystalline Diamond Abrasive," *Int. J. Mach. Tool. Manufact.*, vol. 33, no. 2, pp. 285–296, 1993.

[124] Z. Li, L. Wang, T. Suzuki, A. Argoitia, P. Pirouz, and J. C. Angus, "Orientation Relationship Between Chemical Vapor Deposited Diamond and Graphite Substrates," *J. App. Phys.*, vol. 73, pp. 711–715, 1992.

[125] W. R. L. Lambrecht, C. H. Lee, B. Segall, J. C. Angus, Z. Li, and M. Sunkara, "Diamond Nucleation by Hydrogenation of the Edges of Graphitic Precursors," *Nature*, vol. 364, no. 6438, pp. 607–610, 1993.

[126] M. Sternberg, W. R. L. Lambrecht, and T. Frauenheim, "Molecular-Dynamics Study of Diamond/Silicon (001) Interfaces with and without Graphitic Interface Layers," *Phys. Rev. B*, vol. 56, no. 3, pp. 1568–1580, 1997.

[127] F. P. Bowden and H. G. Scott, "The Polishing, Surface Flow and Wear of Diamond and Glass," *Proc. R. Soc. A*, vol. 248, pp. 368–382, 1958.

[128] M. Seal, "The Abrasion of Diamond," *Proc. R. Soc. A*, vol. 248, pp. 379–393, 1958.

[129] T. N. Loladze and G. V. Bokuchava, *The Wear of Diamond and Diamond Wheels*. Moscow: Mashinostroeniye, 1967.

[130] D. Keen, "Some Observations on the Wear of Diamond Tools used in Piston Machining," *Wear*, vol. 17, no. 3, pp. 195–208, 1971.

[131] D. Crompton, W. Hirst, and M. G. W. Howse, "The Wear of Diamond," *Proc. R. Soc. A*, vol. 333, no. 1595, pp. 435–454, 1973.

[132] A. S. Vishnevskii and A. V. Lysenko, "Interphase Reactions Along the Diamond-Iron Interface," *Sinteticheskie Almazy*, vol. 6, no. 4, pp. 7–9, 1974.

[133] A. A. Vertman and A. M. Samarin, "Kinetics of Solution of Carbon in Liquid Iron," *Izv. Akad. Nauk SSSR, Metally*, vol. 1, pp. 46–54, 1965.

[134] H. Tanaka, N. Ikawa, and Tsuwa, "Affinity of Diamond for Metals," *Annals of CIRP*, vol. 30, no. 1, pp. 241–245, 1981.

[135] M. P. Hitchiner and J. Wilks, "Factors Affecting Chemical Wear During Machining," *Wear*, vol. 93, pp. 63–80, 1984.

[136] A. Grigoriev and P. Kovalsky *Indlaqua*, vol. 39, pp. 47–54, 1984.

[137] A. K. Gangopadhyay and M. A. Tamor, "Friction and Wear Behavior of Diamond Films Against Steel and Ceramics," *Wear*, vol. 169, pp. 221–229, 1993.

[138] H. Tanaka, S. Shimada, N. Ikawa, M. Higuchi, and K. Obata, "Difference in Wear Patterns of Diamond Cutting Tool Depending on Work Material," in *Initiatives of*

Precision Engineering at the Beginning of a Millennium, pp. 179–183, Springer US, 2001.

[139] V. Sahajwalla and R. Khanna, "Monte Carlo Simulation Study of Dissolution of Graphite in Iron-Carbon Melts," *Metall. and Mat. Trans. B*, vol. 31B, pp. 1517–1525, 2000.

[140] S. Shabouk and T. Nakamoto, "Miromachining of Diamond by ferrous materials," 2001.

[141] S. Shabouk and T. Nakamoto, "Micro Machininng of Single Crystal Diamond by Utilization of Tool Wear During Cutting Process of Ferrous Material," *J. Micromechatronics*, vol. 2, no. 1, pp. 13–26, 2003.

[142] M. Uemura, "An Analysis of the Catalysis of Fe, Ni, or Co on the Wear of Diamond," *Tribology International*, vol. 37, pp. 887–892, 2004.

[143] J. M. Casstevens, "Diamond Turning of Steel in Carbon-Saturated Atmospheres," *Prec. Eng.*, vol. 5, no. 1, p. 915, 1983.

[144] C. Evans, "Cryogenic Diamond Turning of Stainless Steel," *Annals of CIRP*, vol. 40, no. 1, pp. 571–575, 1991.

[145] G. Zhang, "Method for Extending Diamond Tool Life in Diamond Machining of Materials that Chemically React with Diamond," Apr 3, 2007 2006.

[146] J. Kohlscheen, H. R. Stock, and P. Mayr, "Chemical Bonding in Magetron Sputtered TiN$_x$ Coatings and its Relation to Diamond Turnability," *Surface Coating Technology*, vol. 142-144, pp. 992–998, 2001.

[147] J. Kohlscheen, H. R. Stock, and P. Mayr, "Tailoring of Diamond Machinable Coating Materials," *Prec. Eng.*, vol. 26, pp. 175–182, 2002.

[148] N. Sasaki and Y. Saito, "Atomic-Scale Modelling of Wear of Carbon Thin Film Containing Nitrogen Using Tersoff-type Interatomic Potentials," *Nippon Kikai Gakkai Ronbunshu, A-hen*, vol. 68, no. 665, pp. 175–180, 2002.

[149] J. Häglund, A. F. Guillermet, G. Grimvall, and M. Körling, "Theory of Bonding in Transition-metal Carbides and Nitrides," *Phys. Rev. B*, vol. 48, no. 16, pp. 11685–11691, 1993.

[150] S. Shimada, H. Tanaka, M. Higuchi, T. Yamaguchi, S. Honda, and K. Obata, "Thermo-Chemical Wear Mechanism of Diamond Tool in Machining of Ferrous Metals," *Annals of CIRP*, vol. 53, no. 1, pp. 57–60, 2003.

[151] B. K. Nash, B. K. Rao, and P. Jena, "Equilibrium Structure and Bonding of Small Iron-Carbon Clusters," *J. Chem. Phys*, vol. 105, no. 24, p. 11020, 1996.

[152] I. Shim and K. A. Gingerich, "All Electron *Ab Initio* Investigation of the Electronic States of the FeC Molecule," *Euro. Phys. J. D*, vol. 7, pp. 163–172, 1999.

[153] A. N. Timoshevskii, V. A. Timoshevskii, and B. Z. Yanchitsky, "Influence of Carbon and Nitrogen on Electronic Structure and Hyperfine Interactions in FCC Iron-Based Alloys," *J. Phys.*, vol. 13, pp. 1051–1061, 2001.

[154] W. C. Chiou Jr. and E. A. Carter, "Structure and Stability of Fe$_3$C-Cementite Surfaces from First Principles," *Surface Science*, vol. 530, p. 87100, 2003.

[155] D. E. Jiang and E. A. Carter, "Carbon Dissolution and Diffusion in Ferrite and Austenite from First Principles," *Phys. Rev. B*, vol. 67, no. 214103, pp. 1–11, 2003.

[156] F. Ding, K. Bolton, and A. Rosen, "Iron-carbide Cluster Thermal Dynamics for Catalyzed Carbon Canotube Growth," *J. Vac. Sci. Technol. A*, vol. 22, pp. 1471–1476, 2004.

[157] M. Weissmann, G. Garc*i*a, M. Kiwi, and Ram*i*rez, "Theoretical Study of Carbon-coated Iron Nanowires," *Phys. Rev. B*, vol. 70, p. 201401, 2004.

[158] Y. Shibuta and S. Maruyama, "Bond-order Potential for Transition Metal Carbide Cluster for the Growth Simulation of a Single-walled Carbon Nanotube," *Comp. Mat. Sci.*, vol. 39, pp. 842–848, 2007.

[159] L. M. Raff, M. Malshe, M. Hagan, D. I. Doughan, M. G. Rockley, and R. Komanduri, "*Ab Initio* Potential-Energy Surfaces for Complex, Multichannel Systems Using Modified Novelty Sampling and Feedforward Neural Networks," *J. Chem. Phys.*, vol. 122, p. 084104, 2005.

[160] P. Shewmon, *Diffusion in Solids*. New York: The Minerals, Metals Materials Society, 2nd ed., 1989.

[161] W. Humphrey, A. Dalke, and K. Schulten, "VMD - Visual Molecular Dynamics," *J. Molecular Graphics*, vol. 14, pp. 33–38, 1996.

[162] J. Rifkin, "XMD - Molecular Dynamics for Metals and Ceramics," 2004-01-07 2004.

[163] P. McCluskey and T. Freeman, "C Code for Brenner Potential Molecular Dynamics," 2002-10-25.

[164] X. Bi, B. Ganguly, G. P. Huffman, F. E. Huggins, M. Endo, and P. C. Eklund, "Nanocrystalline α-Fe, F_3C, and Fe_7C_3 produced by CO_2 Laser Pyrolysis," *J. Mat. Res.*, vol. 8, no. 7, pp. 1666–1674, 1993.

[165] T. Fukuoka *in Tribology International 37 (2004) 887–892*.

[166] J. F. Angress and S. A. Hall, "An Infrared Study of the Maximum Lattice Frequency in Diamond," *J. Phys. C*, vol. 12, pp. 4623–4629, 1979.

[167] R. J. Nemanich, J. T. Glass, G. Lucovsky, and R. E. Shroder, "Raman Scattering Characterization of Carbon Bonding in Diamond and Diamondlike Thin Films," *J. Vacuum Science and Technology A*, vol. 6, no. 3, pp. 1783–1787, 1987.

[168] T. N. Loladze and G. V. Bokuchava, "Criteria for Determining Cutting Properties of Abrasive Tools," in *New Development in Grinding* (M. C. Shaw, ed.), pp. 432–448, Pittsburgh, PA: Proc. of the Int. Grinding Conference, 1972.

[169] R. Komanduri and L. M. Raff, "A Review on the Molecular Dynamics (MD) Simulation of Machining," *Proc. of the I. Mech. E. (Lon)*, vol. 215 B, pp. 1639–1672, 2001.

[170] W. G. Hoover, A. J. De Groot, C. G. Hoover, I. F. Stowers, T. Kawai, B. L. Holian, T. Boku, S. Ihara, and J. Belak, "Large-scale Elastic-plastic Indentation Simulations via Nonequilibrium Molecular Dynamics," *Phys. Rev. A*, vol. 42, pp. 5844 – 5853, 1990.

[171] R. Komanduri, N. Chandrasekaran, and L. M. Raff, "MD Simulation of Indentation and Scratching of Single Crystal Aluminum," *Wear*, vol. 270, pp. 113–143, 2000.

[172] R. Komanduri, N. Chandrasekaran, and L. M. Raff, "Molecular Dynamics Simulation of Atomic-scale Friction," *Phys. Rev. B*, vol. 61, no. 20, pp. 14007–14019, 2000.

[173] R. Narulkar, S. Bukkapatnam, L. M. Raff, and R. Komanduri, "Molecular Dynamics (MD) Simulations of Diffusion of Carbon into Iron," *Phil. Mag.*, vol. 88, no. 8, pp. 1259–1275, 2008.

[174] H. Opitz, *Tool Wear and Tool Life*, vol. 46. 1963.

[175] C. Phaal, "Structure Studies of Diamond," *Industrial Diamond Review*, vol. 26, no. 300, p. 486, 1965.

[176] J. Wilks and E. M. Wilks, "The Resistance of Diamond to Abrasion," *J. Phys. D*, vol. 5, pp. 1902–1919, 1972.

[177] M. Sharif Uddin, K. H. W. Seah, X. P. Li, M. Rahman, and K. Liu, "Effect of Crystallographic Orientation on Wear of Diamond Tools for Nano-scale Ductile Cutting of Silicon," *Wear*, vol. 257, p. 751759, 2004.

[178] N. Ikawa, R. R. Donaldson, R. Komanduri, W. König, T. H. Aachen, P. A. Mckeown, T. Moriwaki, and I. F. Stowers, "Ultra-precision Metal cutting - the Past, the Present, and the Future," *Annals of CIRP*, vol. 40, no. 2, pp. 587–593, 1997.

[179] J. D. Bernal, "The Structure of Graphite," *Proc. R. Soc. A*, vol. 106, no. 740, pp. 749–773, 1924.

[180] K. J. Caspersen, A. Lew, M. Oritz, and E. A. Carter, "Importance of Shear in the BCC-to-HCP Transformation in Iron," *Phys. Rev. Lett.*, vol. 93, no. 11, pp. 115501/1–4, 2004.

[181] D. L. Bunker, "Classical Trajectory Methods," *Meth. Comp. Phys.*, vol. 10, p. 287, 1971.

[182] L. M. Raff and D. L. Thompson, "Theory of Chemical Reaction Dynamics," vol. III, Boca Raton, FL: CRC Press, 1985.

[183] P. von R. Schleyer, "A Simple Preparation of Adamantane," *J. Am. Chem. Soc.*, vol. 79, no. 12, p. 3292, 1957.

[184] G. K. Williamson and R. E. Smallman, "X-ray Evidence for the Interstitial Position of Carbon in α-Iron," *Acta Cryst.*, vol. 6, pp. 361–362, 1953.

[185] K. Tokumitsu, K. Majima, and R. Yamamoto, "Transformation of Fe-C System to High Pressured Hexagonal Structures by Mechanical Alloying of Elemental Powder," *Solid State Ionics*, vol. 172, pp. 211–214, 2004.

[186] K. Tokumitsu and M. Umemoto, "Structural Change and ^{57}Fe Mossbauer Spectroscopy of Mechanically Alloyed Fe_3C and Fe_5C_2," *Mat. Science Forums*, vol. 360-362, pp. 183–188, 2001.

[187] V. Iota, J. H. P. Klepesis, and C. S. Yoo, "Electronic Structure and Magnetism in Compressed 3d Transition Metals," *App. Phys. Lett.*, vol. 90, pp. 042505–1–042505–3, 2007.

[188] E. G. Moroni and T. Jarlborg, "BCC and HCP Phase Competition in Fe," *Europhys. Lett.*, vol. 33, no. 3, pp. 223–228, 1996.

[189] A. Sauveur, *The Metallography and Heat Treatment of Iron and Steel*. Sauveur and Boylston, 1918.

[190] J. Chipman, "Thermodynamics of Liquid Fe-C Solutions," *Metall. and Mat. Trans. B*, vol. 1, no. 8, pp. 2163–2168, 1970.

[191] E. J. Fasiska and G. A. Jeffrey, "On the Cementite Structure," *Acta Cryst.*, vol. 19, pp. 463–471, 1965.

[192] K. Matsunaga, C. Fisher, and H. Matsubara, "Tersoff Potential Parameters for Simulating Cubic Boron Carbonitrides," *Jpn. J. Appl. Phys.*, vol. 39, pp. L48–L51, 2000.

[193] Y. Umeno, T. Kitamura, K. Date, M. Hayashi, and T. Iwasaki, "Optimization of Interatomic Potential for Si/SiO_2 System Based on Force Matching," *Comp. Mat. Sci.*, vol. 25, no. 3, pp. 447–456, 2002.

[194] M. Malshe, R. Narulkar, L. M. Raff, M. Hagan, S. Bukkapatnam, and R. Komanduri, "Parameterization of Analytical Interatomic Function Using Neural Network (NN)," *J. Chem. Phys*, vol. 129, pp. 044111/1–9, 2008.

[195] M. T. Hagan and M. B. Menhaj, "Training Feedforward Networks with the Marquardt Algorithm," *Neural Networks*, vol. 5, no. 6, pp. 989 – 993, 1994.

[196] C. Möller and M. S. Plesset, "Note on an Approximation Treatment for Many-Electron Systems," *Phys. Rev.*, vol. 46, pp. 618–622, 1934.

[197] O. K. Rice and H. C. Ramsperger, "Theories of Unimolecular Gas Reactions at Low Pressures. II," *J. Am. Chem. Soc.*, vol. 32, p. 225, 1928.

[198] K. Hornik, M. Stinchcombe, and H. White, "Multilayer Feedforward Networks are Universal Approximators," *Neural Networks*, vol. 2, no. 5, pp. 359–366, 1989.

[199] B. C. Bolding and H. C. Andersen, "Interatomic Potential for Silicon Clusters, Crystals, and Surfaces," *Phys. Rev. B*, vol. 41, no. 15, pp. 10568 – 10585, 1990.

[200] M. Malshe, R. Narulkar, L. M. Raff, M. Hagan, S. Bukkapatnam, and R. Komanduri, "Development of Generalized Potential-Energy Surfaces Using Many-body Expansions, Neural Networks, and Moiety Energy Approximations," *J. Chem. Phys*, vol. 130, p. 184102, 2009.

[201] M. Malshe, L. M. Raff, M. Hagan, S. Bukkapatnam, and R. Komanduri, "Theoretical Investigation of the Dissociation Dynamics of Vibrationally Excited Vinyl Bromide on an *Ab Initio* Potential-Energy Surface Obtained using Modified Novelty Sampling and Feedforward Neural Networks. ii. Numerical Application of the Method," *J. Chem. Phys*, vol. 127, p. 134105, 2007.

[202] J. M. Soler, E. Artacho, J. D. Gale, Garciá, J. Junquera, Ordejón, and D. Sánchez-Portal, "The SIESTA Method for *Ab initio* order-N Materials Simulation," *J. Phys.*, vol. 14, pp. 2745–2779, 2002.

[203] D. R. Hamann, M. Schlüter, and C. C., "Norm-Conserving Pseudopotentials," *Phys. Rev. Lett.*, vol. 43, pp. 1494 – 1497, 1979.

[204] G. B. Bachelet, D. R. Hamann, and M. Schlüter, "Pseudopotentials that work: From H to Pu," *Phys. Rev. B*, vol. 26, pp. 4199 – 4228, 1982.

[205] J. P. Perdew and A. Zunger, "Self-interaction Correction to Density-Functional Approximations for many-electrons system," *Phys. Rev. B*, vol. 23, pp. 5048–5079, 1981.

[206] J. P. Perdew, B. Burke, and M. Ernzerhof, "Generalized Gradient Approximations Made Simple," *Phys. Rev. Lett.*, vol. 77, pp. 3865 – 3868, 1996.

[207] F. P. Bowden and D. Tabor, *The Friction and Lubrication of Solids*. London: Oxford Univ. Press, 1950.

[208] H. H. Hurt and D. L. Decker, "Tribological Considerations of the Diamond Single Point Tool," *Proc. of the SPIE*, vol. 508, pp. 126–131, 1984.

[209] H. J. Monkhorst and J. D. Pack, "Special Points for Brillouin-zone Integrations," *Phys. Rev. B*, vol. 13, pp. 5188–5192, 1976.

[210] A. Rahman and L. M. Raff, "Trajectory Investigations of the Dissociation Dynamics of Vinyl Bromide on an *Ab Initio* Potential-Energy Surface," *J. Phys. Chem. A*, vol. 105, no. 11, pp. 2156 –2172, 2000.

[211] A. S. Vishnevskii, A. V. Lysenko, T. D. Ositinskaya, and V. G. Delevi, "Role of Diffusion and Graphitization in the Interphase Interaction of Synthetic Diamond with Iron," *Izvestiya Akademii Nauk SSSR, Neorganicheskie Materialy*, vol. 11, no. 9, pp. 1589–1593, 1975.

[212] A. S. Vishnevskii and A. V. Lysenko, "Effect of Electronic States on the Reactive Diffusion of Carbon in Transition Metals," *Metallofizika*, vol. 66, pp. 67–71, 1976.

VITA

Rutuparna Narulkar

Candidate for the Degree of

Doctor of Philosophy

Dissertation: INVESTIGATION ON THE MECHANISM OF WEAR OF SINGLE CRYSTAL DIAMOND TOOL IN NANOMETRIC CUTTING OF IRON USING MOLECULAR DYNAMICS (MD)AND THE DEVELOPMENT OF GENERALIZED POTENTIAL ENERGY SURFACES (GPES) BASED ON *AB INITIO* CALCULATIONS

Major Field: Mechanical Engineering

Biographical:

Personal Data: Born in Harda, MP, India on July 20, 1977.

Education:
Received the B.S. degree from Pt. Ravishankar University, Raiput, Chattisgarh, India, 1999, in Mechanical Engineering
Received the M.S. degree from Oklahoma State University, Stillwater, OK, US, 2003, in Mechanical Engineering
Completed the requirements for the degree of Doctor of Philosophy with a major in Mechaical Engineering Oklahoma State University in Dec, 2009.

Name: Rutuparna Narulkar   Date of Degree: December, 2009

Institution: Oklahoma State University   Location: Stillwater, Oklahoma

Title of Study: INVESTIGATION ON THE MECHANISM OF WEAR OF SIN-
                 GLE CRYSTAL DIAMOND TOOL IN NANOMETRIC CUTTING OF
                 IRON USING MOLECULAR DYNAMICS (MD)AND THE DEVELOP-
                 MENT OF GENERALIZED POTENTIAL ENERGY SURFACES (GPES)
                 BASED ON *AB INITIO* CALCULATIONS

Pages in Study: 192   Candidate for the Degree of Doctor of Philosophy

Major Field: Mechanical Engineering

Scope and Method of Study: Diamond, the hardest of all materials known, undergoes severe wear in the machining of iron. This is because of the strong chemical affinity of iron towards carbon. However, the micro-mechanisms of wear are not well understood. A review of literature indicates graphitization of diamond as the leading cause of wear. Lack of direct evidence led us to investigate the wear mechanism of diamond in the machining of pure iron by MD simulations.

Findings and Conclusions: In this investigation, the role of iron in the wear of diamond was established. MD simulations of nanometric cutting were conducted at 100 m s^{-1}. It has been shown that diamond initially graphitizes and subsequently reacts with iron to form iron carbide, thus confirming the plausible mechanism proposed some 30 years ago.

Central to atomistic simulations is the potential energy surfaces (PES). In this investigation, we have advanced two methods for the development of PES. The first involves modification of the parameters in the existing analytical functional forms, such as Tersoff potential, and the second method involves the development of generalized PES independent of any specific functional form using ab initio calculations, many body expansion, and neural networks. These methods were developed so that PES for different materials can be obtained.

ADVISOR'S APPROVAL: R. Komanduri